COMPUTATIONAL MODELLING OF BUOYANCY-DRIVEN DISPLACEMENT VENTILATION FLOWS

A thesis submitted to The University of Manchester
for the Degree of Doctor of Philosophy
in the Faculty of Engineering and Physical Sciences

2016

CHUN CHUAN CHANG

School of Mechanical, Aerospace and Civil Engineering

CONTENTS

Words count 42,642

LIST OF FIGURES

LIST OF TABLES

ABSTRACT

The University of Manchester

Chun-Chuan Chang

Doctor of Philosophy

Computational Modelling of Buoyancy-Driven Displacement Ventilation Flows

13th April 2016

The study of the buoyancy–driven displacement ventilation flows has been conducted earlier through both mathematical modelling and experiments. There can be some assumptions made in the studies for thermal analysis such as: adiabatic boundaries, neglecting radiation heat transfer between wall surfaces, and neglecting the absorptivity of the air on simulating the thermal distribution within the ventilated spaces. This study considers heat conduction at boundaries, heat radiation between wall surfaces and radiative absorptivity of the air when modelling buoyancy-driven displacement ventilation flows. The simulations were carrying out using computational fluid dynamic (CFD) programme Star-CCM+.

This study investigates the influence of the absorptivity of the air on thermal distribution within an enclosure ventilated by buoyancy-driven displacement ventilation flows. Two cases of buoyancy-driven displacement ventilation experiments conducted early by Sandbach (2009) and Li et al. (1993b) were modelled. To consider the absorptivity of the air, the local weather data were retrieved and were used for calculating the absorption coefficient of the air under different weather conditions. The participating media radiation model was employed to compute the radiation heat absorbed by the air. In addition, the performances of the turbulence models on modelling buoyancy-driven displacement ventilation flows were investigated to ensure the predicted results were accurate and satisfactory.

The simulation results presented in this study have shown to agree well with the experimental data in two different experiment cases. In the case of the experiments conducted by Sandbach and Lane-Serff (2011b), the predicted results match well with the measurements when considering absorptivity of the air. The errors between the simulation results and the measurements were less than 10% in most cases. The results also suggest that the absorption coefficient has an influence on ventilation flow rate and consequently has an effect on the strength of the stratification. This indicates that the absorption coefficient should be determined according to the conditions rather than be given an one-and-for-all value. The simulation results have also shown to agree well with the measurements given in the literature presented by Li et al. (1993b). The effect of the absorptivity was shown to be more significant in the case of high supply airflow temperature or high supply heat load. Hence, radiative absorptivity of the air should be taken into account in order to accurately model the thermal distribution in the ventilated enclosure.

DECLARATION

No portion of the work referred to in the thesis has been submitted in support of an application for another degree or qualification of this or any other university or other institute of learning.

COPYRIGHT

NOMENCLATURE

Roman

Upper case

A	: Area	[m^2]
D_k	: Turbulent production term	
D_b	: Buoyancy production term	
E	: Energy	[kJ]
E_r	: Radiation heat transfer	[W]
F	: Buoyancy flux	[m^4 s^{-3}]
F	: Force	[kg m s^{-2}]
F	: View factor	
F_0	: Buoyancy flux from the source	[m^4 s^{-3}]
H	: Height	[m]
H	: Enthalpy	[kJ]
I_b	: Blackbody emissive power	[W/m^2]
I_r	: Radiation reflected by surfaces	[W/m^2]
I_e	: Radiation emitted by surfaces	[W/m^2]
J	: Radiosity	[W/m^2]
Q	: Heat transfer rate	[W]
R	: Gas constant	
R	: Radius of the plume at certain height	[m]
R_t	: Turbulent Reynolds number	
R_i	: Richardson number	
R_s	: Surface resistance to radiation	
S	: Strain rate tensor	

T	: Turbulent time scale	
T	: Temperature	[K]
T_o	: Reference temperature	[K]
T_s	: Blackbody source temperature	[K]
U	: Internal energy	[kJ]
$\boldsymbol{V}$	: Volume	[m^3]

Lower case

a	: Acceleration	[m s^{-2}]
a_b	: Absorption coefficient	[m^{-1}]
a_s	: Scattering coefficient	[m^{-1}]
a_{ex}	: Extinction coefficient	[m^{-1}]
$\hat{b}_f$	: Non-dimensional buoyancy fluxes in the plume	
$\hat{b}_e$	: Non-dimensional buoyancy of the environment	
c_0	: entrainment constant	
c_d	: Discharge coefficient of openings	
c_i	: Velocity coefficient for lower opening	
c_o	: Velocity coefficient for upper opening	
c_p	: Specific heat	[kJ kg^{-1} K^{-1}]
c_{pa}	: Specific heat capacity of air	[kJ kg^{-1} K^{-1}]
e_c	: Emissivity of CO_2	
e_w	: Emissivity of H_2O	
e_t	: Sum of the emissivity of CO_2 and H_2O	
Δe_{cw}	: Emissivity of CO_2 and H_2O at overlap spectrum	
f_μ	: Damping function	
g	: Gravity	[m s^{-2}]

g'	: Reduced gravity	[m s^{-2}]
g_0'	: Reduced gravity in the environment	[m s^{-2}]
$\hat{g}$	: Non-dimensional reduced gravity	
h	: Convection heat transfer coefficient	[W m^{-2} K^{-1}]
h_c	: Convection heat-transfer coefficient at ceiling	[W m^{-2} K^{-1}]
h_r	: Radiative heat-transfer coefficient	[W m^{-2} K^{-1}]
$\hat{h}_0$	: Non-dimensional height of first front	
$\hat{h}$	: Non-dimensional height	
i_b	: Blackbody radiative intensity	[W m^{-2} sr^{-1}]
i_s	: Radiative intensity	[W m^{-2} sr^{-1}]
$i_{s,s}$	: Scattered radiative intensity	[W m^{-2} sr^{-1}]
k	: Turbulent kinetic energy per unit mass	[m^2 s^{-2} kg^{-1}]
k	: Thermal conductivity	[W m^{-1} K^{-1}]
k_c	: Conductive heat-transfer coefficient at ceiling	[W m^{-1} K^{-1}]
l	: Distance	[m]
l_t	: Turbulence length scale	[m]
l_m	: Prandtl mixing length	[m]
m	: Mass	[kg]
$\hat{m}_p$	: Non-dimensional momentum fluxes in the plume	
$\bar{m}$	: Scattering cross section for a particle	[m^2]
$\bar{n}$	: Number of particles per unit volume	[m^{-3}]
n_p	: Number of plume layers	
p	: Pressure	[Pa]
p_c	: Partial pressure of CO_2	[Pa]
p_w	: Partial pressure of H_2O	[Pa]
p_m	: Partial pressure of H_2O in the gas mixture	[Pa]

p_s	: Saturated vapour pressure of H_2O	[Pa]
p_v	: Vapour pressure	[Pa]
r	: Radial coordinate of a conical form	[m]
t	: Time	[s]
t_s	: Time step	[s]
u	: Velocity	[m s^{-1}]
$\bar{u}$	: Mean velocity	[m s^{-1}]
v	: Velocity	[m s^{-1}]
v_s	: Maximum air velocity in the domain	[m s^{-1}]
v	: Volume	[m^3]
$\dot{v}$	: Volume flux	[m^3 s^{-1}]
$\hat{v}_p$	: Non-dimensional volume fluxes in the plume	
w	: Velocity in vertical direction	[m s^{-1}]
w_t	: Vertical velocity of plume	[m s^{-1}]
w_s	: Vertical velocity of first front	[m s^{-1}]
$\hat{w}$	: Non-dimensional vertical velocity	
Δx	: Size of mesh cells	[m]
z	: Distance at vertical direction	[m]
z_s	: Position of first front	[m]
z_p	: Distance between neutral level and first front	[m]

Greek

α	: Absorptivity	
α	: Thermal diffusivity	[m^2 s^{-1}]
α_p	: Plank-mean absorption coefficient	[m^{-1}]
ρ	: Density	[kg m^{-3}]

ρ : Reflectivity

ρ_o : Density far from the plume (reference density) [kg m^{-3}]

ρ_1 : Ambient density [kg m^{-3}]

θ : Angle

σ : Courant-Friedrichs-Lewy coefficient

σ_ϵ : Turbulent Schmidt number in dissipation transport equation

σ_k : Turbulent Schmidt number in kinetic transport equation

δ_{ij} : Kronecker delta

τ : Non-dimensional time

τ : Shear stress [Pa]

τ : Transmissivity

τ_η : Spectral transmissivity

ε : Dissipation

ϵ_{ij} : Strain rate

β : Volume expansion coefficient [K^{-1}]

λ : Spectral wavelength [μm]

ν : Kinematic viscosity [m^2 s^{-1}]

μ : Dynamic viscosity [kg $m^{-1}s^{-1}$]

μ_T : Eddy viscosity [kg $m^{-1}s^{-1}$]

ω : Circumferential angle

Ω : Solid angle

Ω_0 : Rotation rate tensor

ϕ : Blending function of two-layer formulation

ϕ : Relative humidity

$\varphi(\theta,\omega)$: Phase function of scattering

Superscripts

– : Time-mean

– : Average

^ : Non-dimensional

Subscripts

b : Buoyancy

k : Turbulent production

const : Constant

cond : Heat conduction

conv : Heat convection

in : Input

out : Output

sys : System

v: : Vertical

∞ : Infinite

CHAPTER ONE

1 Introduction

1.1 Context

In the early ages of human history, an enclosed space is mainly a shelter for humans to avoid severe weather. But gradually the enclosed areas have been used for many other purposes such as working, leisure activities, and dinning. Thus the amount of time spent in the enclosed spaces has increased. The longer the humans stay in the enclosed areas the greater the impact of contaminants will have on human health. Hence, maintaining indoor air quality and thermal comfort for occupants in the space has become an important task. The contaminants often come from human respiration and human body heat (Bjorn and Nielsen, 2002, Zukowska et al., 2012). To remove the pollutant inside houses, the enclosed region should be provided with adequate ventilation rates so to avoid putting the occupants' health at risk (The British Standards Institution, 1999). To achieve this, ventilation systems are installed to provide airflows which keep the internal environment at a satisfactory degree of thermal comfort.

In most cases, the operation of conventional ventilation systems relies on mechanical devices such as chillers, pumps, and fans to maintain the required indoor air temperatures and air circulations. This often consumes significant amounts of energy throughout the years. With the increasing demands of eco-friendly buildings that emit less carbon dioxide, an environmentally friendly natural ventilation system which uses less mechanical components would be a potential solution to it.

Natural ventilation is widely applied in buildings in cold climate regions. Due to temperature differences, the warm and polluted air inside the space can be naturally vented out through openings. There are mainly two types of ventilation mechanisms: mixing ventilation and displacement ventilation depends on where the openings are

mounted on the walls of the room. Although it is convenient to apply natural ventilation in a cold climate region, a poorly designed ventilation system could still cause discomfort for occupants in two extreme scenarios: low air quality with a thick stratification layer or high air change rate. A well designed natural ventilation room, on the other hand, provides a good level of fresh air and also maintains the house at a comfortable temperature.

For hot climate regions, most buildings run HVAC system throughout most of the year which consumes enormous amount of energy. This has led to the consequence of vast spending on energy bills and thus a non-environmentally friendly building. A building designed with an efficient natural ventilation system, however, can significantly reduce energy consumption and minimise the carbon-dioxide emissions. An investigation on energy consumption of an office ventilated by different types of ventilations system was carried out by The Association for the Conservation of Energy (Scrase, 2000). The result shows that the office ventilated by A/C ventilation system consumes more energy than those offices ventilated naturally by up to 90% as shown in Figure 1-1.

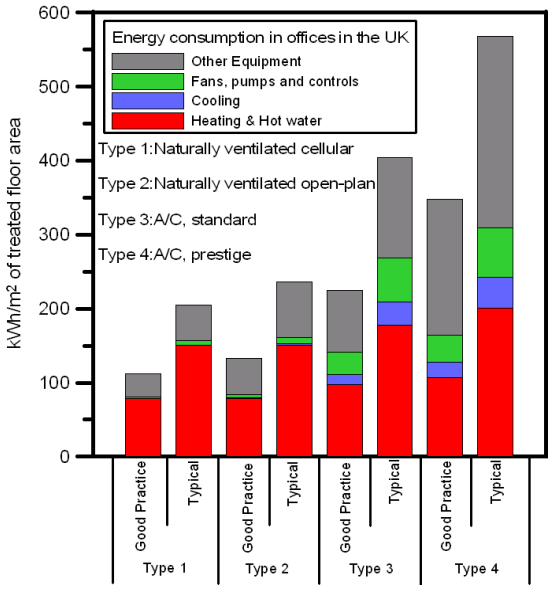

Figure 1-1: Energy consumption by different types of ventilation systems.

In natural ventilation, the air movement is initiated by two sources: pressure differences and temperature differences. The pressure differences are produced by winds that drive airflows into the enclosure; the temperature differences are produced by heat sources which create buoyancy flows driving the airflow moving upward. In an indoor space, the heat sources can be occupants, electrical devices, or wall surfaces which releasing the heat absorbed from solar radiation as shown in Figure 1-2. The air circulation inside the enclosed region is initiated by the buoyancy forces generated by these heat sources. The hot airflows rise up from the heat sources and flow out of the space through upper openings creating an empty space at the lower half of the space. The empty space is then filled with descending cool air coming in through other openings. This is the principal idea of natural ventilation.

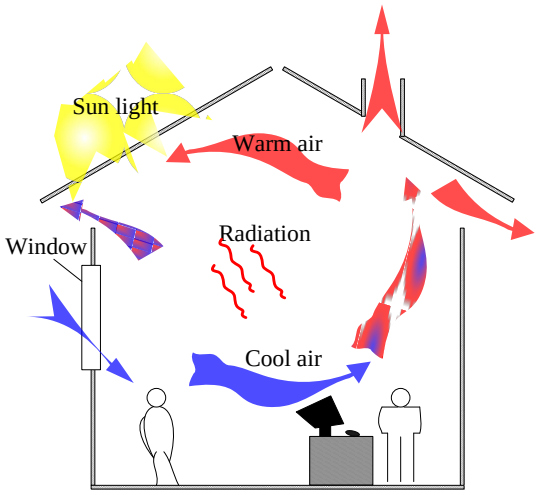

Figure 1-2: Schematic of natural ventilation.

This study begins with an investigation of buoyancy flows in a confined region (as shown in Figure 1-3) by reviewing earlier studies on analysing plume flows, stratification layers, and density profile in the space. The early studies investigated the buoyancy plumes behaviour by conducting salt bath experiments (Baines and Turner, 1969).

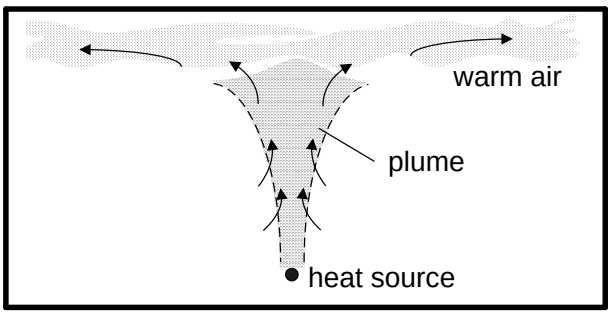

Figure 1-3: Buoyancy flow generated by heat source.

Injecting the salt solution into the fresh water tank creates an inversed case of buoyancy flow in a confined space. The salt solution descends down to the bottom of the fresh water tank as soon as it is released; it then immediately spreads out to form a stratification layer. The salt solution arriving later entrains the fluid from the layer firstly formed to become even heavier replacing the position of first layer by pushing it upwards (see Figure 1-4).

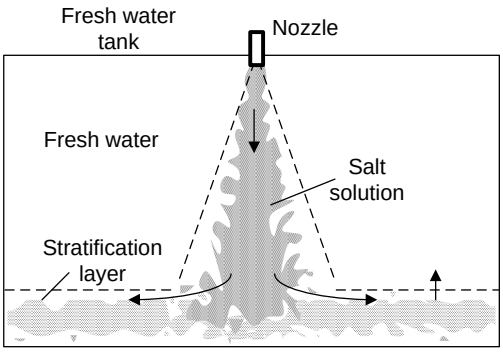

Figure 1-4: Salt bath experiment.

The experimental results were then used to verify the modelling results from the mathematical models developed for buoyancy plume flows. A time-dependent approximate analytic expression developed by Worster and Huppert (1983), for example, models the density profile of the fluid above the interface of stratification layer.

Following the analysis of a buoyant plume in a confined region, some earlier studies move on to investigate the buoyancy flows in a displacement ventilation flow region via both modelling and experimental approaches (see Figure 1-5). The simulations were carried out by solving either the conventional turbulence models or the numerical models developed by earlier researchers. The experiments conducted were in a full-scale test room. The buoyancy force was generated by a heater placed in a test-room. The simulation results were then compared with the measurements for analysis.

In validating the simulation results, it was found that the agreement was poorer when comparing the results with salt-bath experiment. The discrepancy can also be found when comparing the modelling results with measurements from full-scale experiment. This study works on the causes of the discrepancy and the methods that can improve the predictive accuracy in modelling displacement ventilation flows.

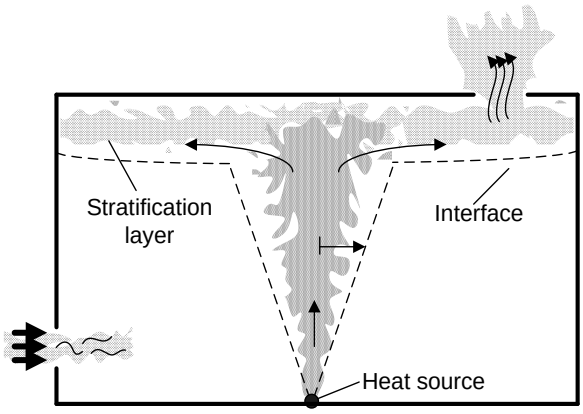

Figure 1-5: Buoyancy-driven displacement ventilation flow.

1.2 Research objectives

From the simulations and experiments conducted in the early studies, it is found that many factors affect the results of modelling buoyancy plume flow. The salt bath experiment can model the entrainment behaviour of the buoyant plume; however, the diffusivity of the fluid can be different from the air in the real case. In addition, heat transfer through and between boundaries can take place due to the heat transfer from the heat sources in the space. That is also deemed to have a significant effect on the density profile and the formation of stratification layer (Li et al., 1993b).

The radiative absorptivity of the air filled in between the surfaces of the enclosed region was often neglected in most of the early studies. Some cases considered the absorptivity of the air; however, it was assumed to be independent of the air conditions (e.g. Howell and Potts, 2002).

In the case of displacement ventilation flow, the airflow in the region can be very complex and are usually a combination of all sorts of flow elements with different levels of turbulence. There can be high turbulence airflows near the openings and above the heat sources. There can also be low turbulence airflows at the near wall regions. In addition, some high turbulent flows can return back to laminar flows due to damping effect (Narasimha and Sreenivasan, 1979). This phenomenon is called relaminarization (Noto and Nakai, 2008, Steiner, 1971). Solving above all the mentioned problems are the objectives of this study.

1.2.1 Objectives

The objective of this study is to improve the predictive accuracy on modelling thermal distributions in a buoyancy-driven displacement ventilation flow region. To achieve this, the performance of turbulence models on modelling airflows at different turbulent level was conducted; the effect of the absorptivity of the participating gases, H_2O and CO_2, was considered. The absorption coefficient of the air is determined accordingly to its condition.

This study employs CFD programme Star CCM+ to conduct simulations. Star CCM+ is a single integrated CFD software using the finite volume method. It allows users to complete a CFD simulation project entirely within the Star CCM+ environment. That is: building CAD geometry, constructing grids, solving governing equations, and post-processing. Unstructured meshes such as polyhedral and trimmed hexahedral mesh are provided for discretising arbitrary geometry flow domains including fluid and solid regions.

In terms of simulating the fluid flow, Star CCM+ is capable of modelling steady/unsteady, compressible/incompressible laminar and turbulent flow problems. The RANS models provided are Spalart-Allmaras, a range of K-Epsilon models, K-Omega model and two Reynolds stress models. For radiative heat transfer analysis, not only is Star CCM+ capable of simulating surface to surface radiation, it provides discrete ordinate modelling (DOM) which accounts for media that is non-transparent to radiation. There are also other CFD commercial software packages which can conduct the simulation work, such as: FLUENT, CFX, STAR CD, and FLOW 3D.

There is a section in the Star CCM+ that allows users to input customized equations and functions. In the simulations, this feature was used to add equations for determining convection heat transfer coefficients at solid boundaries and for judging the convergence of the simulations. The simulation results were then verified with measurements.

In summary, the research objectives are:

a. Investigate the nature and the performance of different turbulence models on modelling typical buoyancy-driven displacement ventilation flow.

b. Investigate the influence of temperature and humidity on absorption coefficient of the air.

c. Investigate the influence of the absorptivity of the air to the energy distribution and air volume flow rate within displacement ventilation space.

d. Validate the modelling results obtained in this study with measurements from the literatures.

1.3 Thesis outline

This study begins by reviewing the analysis of buoyancy plume flows, buoyancy-driven ventilation flows, the performance of the turbulence models on modelling displacement ventilation flows and the influence of the radiation heat transfer on thermal distribution in a ventilated enclosure. As air was considered to be a participating medium in some earlier studies, this study also reviewed some literatures regarding the participating medium on attenuating the radiative intensity of the radiation. A correlation was then applied and used to determine the absorption coefficients under each condition studied.

Since the performance of a turbulence model can be different at modelling different type of complex turbulent flows, an investigation on the performance of different turbulence models is made to determine a suitable turbulence model for modelling buoyancy-driven displacement ventilation flows. The present study then employs the commercial CFD programme Star CCM+ to simulate the thermal distribution and ventilation flows in a test room. The simulation results were checked to be mesh and time-step independent to guarantee the accuracy of the predictive results. The results were then validated with the measurements of a full-scale experiment for further analysis. The structure and content of this thesis are summarised as follow:

Chapter 2 reviews literatures on buoyancy-driven flows in enclosed space with/without openings, the performance of the turbulence models, the effects of radiation heat transfer on thermal distribution in the ventilated spaces, and the radiative absorptivity of the air.

Chapter 3 details the fundamental theories of the conservation laws, the turbulence models, the heat transfer mechanisms, and the physics of the radiative absorptivity of the participating medium.

Chapter 4 details the modelling methodology which includes constructing the CAD models for simulations, the mesh method used for discretising computational domain,

the boundary conditions, the determination of time stepping and the absorption coefficients of the air. Different sizes of grid cells were constructed for mesh sensitivity analysis. The performance of the turbulence models on modelling the buoyancy-driven displacement ventilation flow is analysed. Lastly, a summary of modelling procedures is presented in a flow chart.

Chapter 5 and Chapter 6 modelled the buoyancy-driven displacement ventilation flow cases presented by Sandbach and Lane-Serff (2011b) and Li et al. (1993b). The modelling results were validated with the experimental data, and the effects of absorptivity of the air were studied.

Chapter 7 presents the conclusions of this study and suggestions for future works.

CHAPTER TWO

2 Background and Literature Review

2.1 Context

Ventilation is a form of air motion or circulation which maintains a certain level of air quality for the space within an enclosure. These air motions are driven by forces that mainly come from two sources: pressure differences and temperature differences. For pressure differences, it is normally regarded to be generated by wind or mechanical devices such as fans. The air motion is then initiated to flow from higher pressure region to lower pressure region as shown in Figure 2-1.

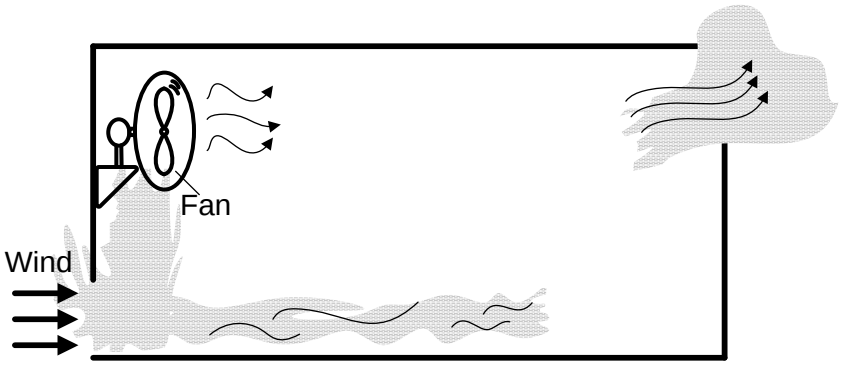

Figure 2-1: Air motion driven by pressure differences.

Temperature differences can be created by the heat sources from humans and facilities inside the enclosure or heat sources coming from outside the enclosure. The temperature differences will result in a density gradient in the air that produces gravitational forces to initiate air motions as shown in Figure 2-2. From the figure we can see that the air heated up by the heat source rises up to the top of the room creating empty space for cold denser air to come in. This rising plume and incoming cool air has then naturally formed an air circulation that ventilates the space.

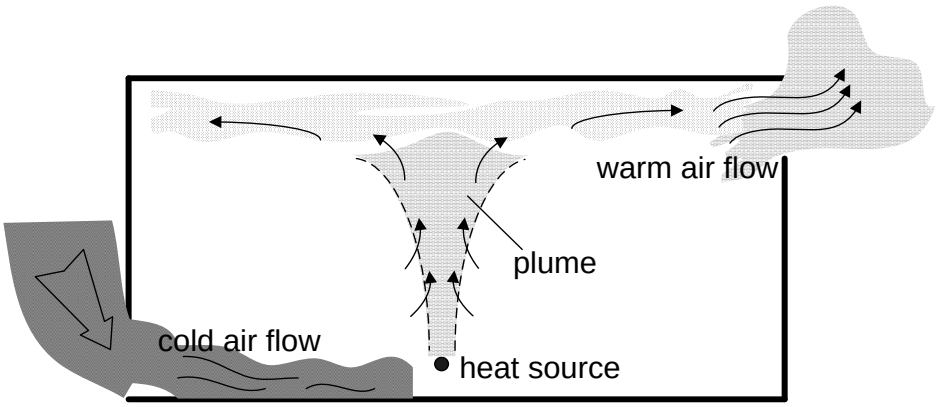

Figure 2-2: Air motion driven by temperature differences.

This study investigates the ventilation flows driven by buoyancy forces and the effects of various factors and boundary conditions to the flows. This chapter reviews previous experimental studies and simulation works so to have a good understanding and a clear view of the background.

2.2 Buoyancy flows

The study of buoyancy flows begins with the investigation of free convection flows produced by heat sources in a gravitational field. The convection flows are observed to leave the point heat sources first as a purely stable laminar flow for a distance, and then turns into unstable turbulent flow with eddy turbulence on the boundary. The laminar zone is however assumed to be small in comparison with that of turbulent region for the convenience of analysis. To deal with the complex nature of free convection flows, an approximate analysis derived from governing equations was then developed with three approximations: pressure intensity remains hydrostatic throughout the field motion; forces in the horizontal direction are ignored in comparison with forces in the vertical direction; and turbulent mixing is only considered in the horizontal direction (Rouse et al., 1952). Experiments were also conducted by Rouse (1952) to measure the mean velocity and density of a plume flow. From the experimental data shown, it is found that Gaussian function can fit

the data quite well and therefore can be used to represent the time averaged velocity and density of a plume flow for convenience.

Based on Rouse's study, a similarity solution was proposed for analysing free convection flows (Batchelor, 1954). The solution was obtained by assuming that the temperature and velocity have similar distributions in all horizontal planes at different distance above point heat sources, and their magnitudes vary as some power of *z*. The study of free convection flow was divided into two parts: laminar flow and turbulent flow. For laminar flow, the vertical velocity and the temperature can be expressed as:

$$w = z^{c_1} \cdot f\left(\frac{r}{R}\right), \tag{2-1}$$

$$\mathrm{g}\left(\frac{T - T_0}{T_0}\right) = z^{c_2} \cdot f\left(\frac{r}{R}\right), \tag{2-2}$$

where w is the vertical velocity at plume axes, c_1, c_2 are powers to be determined, g is gravity, T is temperature, T_0 is the ambient temperature at given point, r is radial distance from the vertical line of conical form, and R is the radius of the heat plume at height z. That is,

$$R \propto z^{c_3}, \tag{2-3}$$

where c_3 is a constant. To find out the relationship between buoyancy flux and velocity and temperature fields, an equation can be formed base on the condition that buoyancy flux across all horizontal planes is the same for a steady motion plume flow:

$$F = \int_0^\infty wg\frac{T - T_0}{T_0} 2\pi r dr \,, \tag{2-4}$$

where F is the buoyancy flux. This equation can only be satisfied if $c_1+c_2+2c_3=0$. In the equation of momentum, the acceleration, buoyancy acceleration and viscous retardation terms depend on z should be in the same dimension,

$$\frac{w^2}{z} \sim g\frac{T - T_0}{T_0} \sim \frac{\nu w}{R^2}, \tag{2-5}$$

where ν is the kinematic viscosity. Therefore it provides another correlation for powers of c_1, c_2, and c_3:

$$2 \cdot c_1 - 1 = c_2 = c_1 - 2 \cdot c_3 \,. \tag{2-6}$$

For the fact that velocity and buoyancy relations can be influence only by F, r, ν, z, and thermal diffusivity α, the general form of velocity and buoyancy can be obtained through dimensional analysis. That is,

$$w = \left(\frac{F}{\nu}\right)^{\frac{1}{2}} \cdot f\left(\frac{rF^{\frac{1}{4}}}{z^{\frac{1}{2}}\nu^{\frac{3}{4}}}, \frac{\nu}{\alpha}\right), \tag{2-7}$$

$$g\frac{T - T_0}{T_0} = \frac{F}{\nu z} \cdot f\left(\frac{rF^{\frac{1}{4}}}{z^{\frac{1}{2}}\nu^{\frac{3}{4}}}, \frac{\nu}{\alpha}\right), \tag{2-8}$$

$$R = \frac{z^{\frac{1}{2}}\nu^{\frac{3}{4}}}{F^{\frac{1}{4}}} \cdot f\left(\frac{\nu}{\alpha}\right). \tag{2-9}$$

For turbulent flow, the diffusion effects are ignored so the mean vertical velocity and the temperature can be expressed as:

$$w_t = \left(\frac{F}{z}\right)^{\frac{1}{3}} \cdot f\left(\frac{r}{R}\right), \tag{2-10}$$

$$\mathrm{g}\left(\frac{\overline{T - T_0}}{T_0}\right) = \frac{F^{\frac{2}{3}}}{z^{\frac{5}{3}}} \cdot f\left(\frac{r}{R}\right), \tag{2-11}$$

where w_t is mean vertical velocity of turbulent flow, and F is the buoyancy flux. The similarity solution above is confirmed by the measurements conducted by Yih (Yih, 1951) both to have dependence of velocity and temperature on vertical distance z.

This similarity solution was than questioned by other investigators for its limitation in some scenarios. First of all, previous researches have assumed that the surrounding air into which the heated current is rising is uniform. However, the similarity solution can no longer be applicable when there is a density gradient in the ambient air. Secondly, in a stably stratified ambient fluid, the motion of rising flow is limited to an extent in vertical direction; therefore, seeking the solutions are dependent on power of vertical distance z becomes unnecessary (Morton et al., 1956). In order to study vertical convection flows without considering the turbulent eddies mixing with the ambient air in detail, the equations of conservation of volume, momentum and density deficiency was proposed by Morton (1956) based on the simpler transfer assumptions (Taylor and U.S. Atomic Energy Commission, 1946). They are:

(1) The rate of air entrained through the rising plume edge is proportional to the upward velocity at that height in the plume.

(2) The mean velocity and buoyancy force in horizontal section across the plume are assumed to be constant at all heights (e.g. top-hat profile).

(3) The density variation within the plume is small in comparison with the reference density in the environment at the source level.

By this means the problems can be solved without the concerns for different conditions of ambient fluid. As velocity and buoyancy force are assumed to be constant in horizontal section across the plume at all heights and zero value outside of it (also called top-hat profile, see Figure 2-3), the conservation relations of volume, momentum, and buoyancy can then be expressed as:

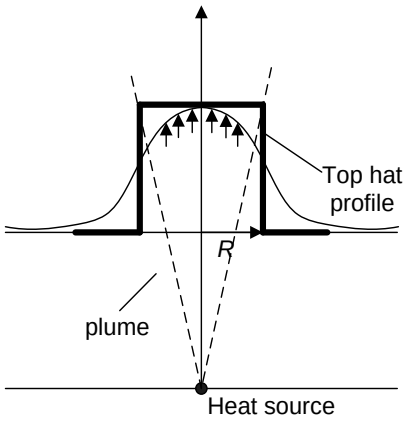

Figure 2-3: Schematic of top hat profile.

Conservation of volume:

$$\frac{d(\pi R^2 w_t)}{dz} = 2\pi R c_0 w_t \,. \tag{2-12}$$

Conservation of momentum:

$$\frac{d(\pi R^2 {w_t}^2)}{dz} = \pi R^2 \mathrm{g}\,(\rho_0 - \rho)\,. \tag{2-13}$$

Conservation of buoyancy:

$$\frac{d\left(\pi R^2 w_t(\rho_1 - \rho)\right)}{dz} = 2\pi R c_0 w_t(\rho_1 - \rho_0)\,, \tag{2-14}$$

where c_0 is the proportionality constant (entrainment constant), so that the inflow velocity at the edge of the plume is some fraction c_0 of upward velocity inside the plume w_t as shown in Figure 2-4. $\rho(r,z)$ and $\rho_0(z)$ are the density inside and outside the plume, $\rho_1 = \rho_0(0)$ is the reference density.

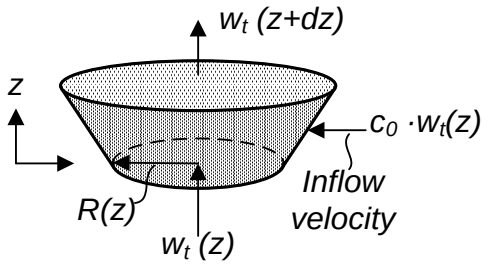

Figure 2-4: Schematic of slice of plume.

However, the plume in a conical form with apex at the point source described by the theoretical method above is not the same in real cases. Therefore, the calculation of the position of virtual source is introduced by Morton (1956). He suggests that the displacement of a virtual source (as shown in Figure 2-5) needs to be determined for experiments before the comparison is made with the theoretical results.

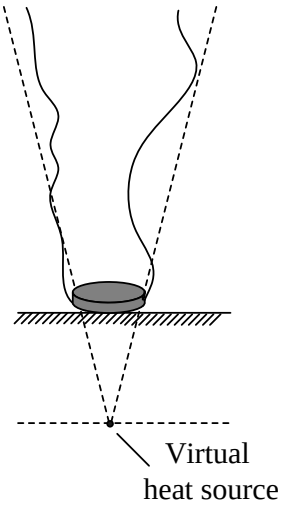

Figure 2-5: Position of virtual heat source.

Apart from the buoyancy plumes generated from a single point heat source, plumes generated from multiple heat sources are also studied such as line heat source (Turner, 1969), or heat sources distributed within an area (Etheridge and Sandberg, 1996). This case can be found in cinemas or conference rooms where people are the main source for generating thermal plumes (Zukowska et al., 2012). As rising plumes widen gradually by entraining external fluid across its boundary by large eddies (Townsend, 1970) (see Figure 2-6), the studies show the plumes from each source will eventually merge to one single plume after a distance from the heat sources. Its characteristic is found to be the same as those of plumes from a single source. The study also indicated that the total flow rate of the buoyancy flux is greater when it comes from multiple sources rather than a single one (see Figure 2-7).

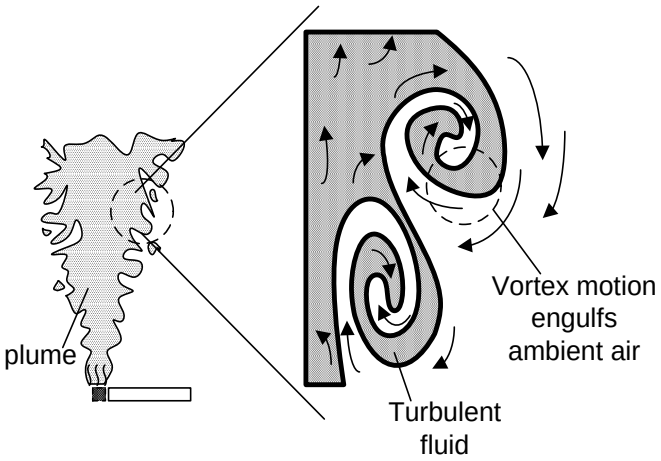

Figure 2-6: Entrainment process at boundary.

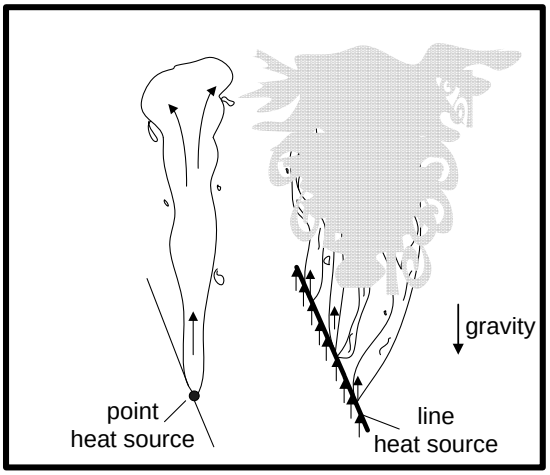

Figure 2-7: Plume generated from single and multiple sources.

2.3 Buoyancy flow in an unventilated confined region

When rising buoyancy flow is capped in a confined region, the flow will impinged on the top boundary as it collides and form a stratification layer next to it. This case is also known as the filling box model. Experiment has shown that the layer firstly formed is stably stratified and has a discontinuity of density front adjacent to the environment fluid. As time goes on, the first stratification layer is gradually pushed downwards by the new arriving plume fluid replacing the existing layers with even lighter density. Therefore, the stratified region begins to grow (see Figure 2-8). The descending stratification layer gradually modifies the environment fluid and surrounds a larger portion of the plume. In this case, the density distribution of environment is not uniform but is changing accordingly with the properties of the stratified layers.

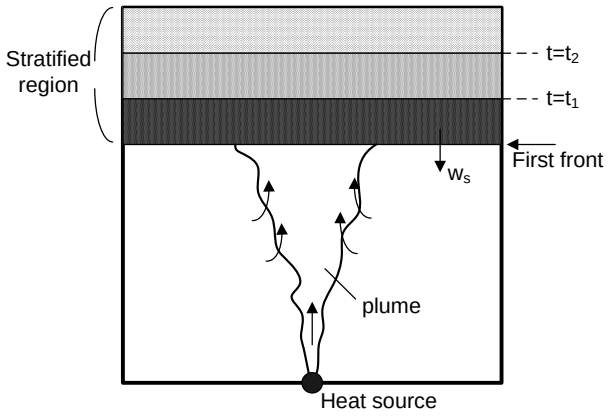

Figure 2-8: Schematic of stratification layers.

To consider the influence of the stratified layer on the ambient fluid, a time-dependent solution was proposed by Baines and Turner (1969). The solution was developed based on the analytic solutions established previously (i.e., Eq. (2-12), Eq. (2-13), Eq. (2-14)), and two other relations derived. First of all, from conservation law, the volume flux of the stratification layer moving downward from upper

boundary must equal to the volume flux of rising plume at any level (see Figure 2-9). That is,

$$-\pi {d_0}^2 w_s = \pi R^2 w_t \,, \tag{2-15}$$

where πd_0^2 is the cross-sectional area of stratification layer, $w_s = dz_s/dt$ is the vertical velocity of first front, z_s, in the environment. Secondly, the density in the environment changes accordingly to the motion of the first front only. That is,

$$\partial g_0'/\partial t = -w_s(\partial g_0'/\partial z)\,, \tag{2-16}$$

where g_0' is the reduced gravity

$$g_0' = \frac{g(\rho_0 - \rho_1)}{\rho_1}. \tag{2-17}$$

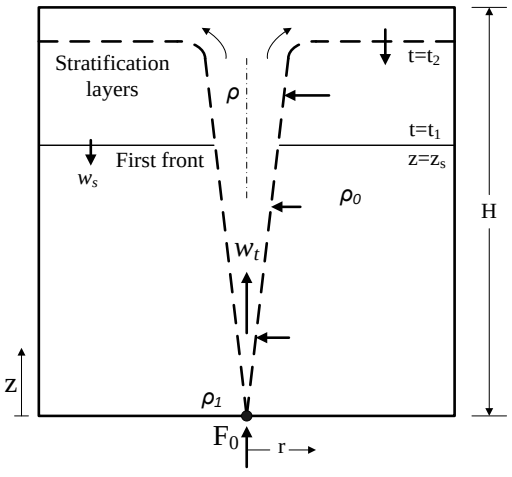

Figure 2-9: Schematic of plume arising in confined region.

Based on the solutions derived by Morton (1956) and given the buoyancy flux F_0, the correlations for the properties of the plume below the first front are:

$$F_0 = \frac{1}{2}\pi R^2 w_t \Lambda|_{z=0}\,, \tag{2-18}$$

where

$$\Lambda = \frac{5}{3\pi}\left(\frac{5\pi}{18}\right)^{\frac{1}{3}} {c_0}^{-\frac{4}{3}} {F_0}^{\frac{2}{3}} z^{-\frac{5}{3}}\,, \tag{2-19}$$

$$R = 6/5\, c_0 z\,, \tag{2-20}$$

$$w_t = \frac{5}{6c_0}\left(\frac{18}{5\pi} c_0 F_0\right)^{\frac{1}{3}} z^{-\frac{1}{3}}\,. \tag{2-21}$$

From the equations above, the time-dependent solution can be expressed as:

$$t = \frac{5}{4c_0}\left(\frac{5\pi}{18c_0}\right)^{\frac{1}{3}} {d_0}^2 \cdot H^{-\frac{2}{3}} {F_0}^{-\frac{1}{3}} \left[\left(\frac{H}{z_s}\right)^{\frac{2}{3}} - 1\right]. \tag{2-22}$$

This time-dependent solution was later modified to develop an approximate analytic solution for filling box model (Worster and Huppert, 1983).

The time-dependent solution developed by Morton (1956) was transformed by a set of non-dimensionalised variables, $\hat{b}_f$, $\hat{v}_p$, $\hat{m}_p$, and $\hat{b}_e$, introduced by Worster (1983) which represent the buoyancy, volume, momentum fluxes and buoyancy of the environment respectively.

Buoyancy flux:

$$\hat{b}_f = \frac{1}{2}\pi F_0^{-1} R^2 w_t g' \,, \tag{2-23}$$

where

$$g' = \frac{g(\rho_0 - \rho)}{\rho_1} \,. \tag{2-24}$$

Volume flux:

$$\hat{v}_p = \frac{1}{4}\pi^{\frac{1}{3}} c_0^{-\frac{4}{3}} H^{-\frac{5}{3}} F_0^{-\frac{1}{3}} R^2 w_t \,. \tag{2-25}$$

Momentum flux:

$$\hat{m}_p = \frac{1}{2}\pi^{\frac{1}{3}} c_0^{-\frac{1}{3}} H^{-\frac{2}{3}} F_0^{-\frac{1}{3}} R w_t \,. \tag{2-26}$$

Buoyancy of the environment (density field above the first front):

$$\hat{b}_e = 4\pi^{\frac{2}{3}} c_0^{\frac{4}{3}} H^{\frac{5}{3}} F_0^{-\frac{2}{3}} g_0' \,. \tag{2-27}$$

Also together with the new introduced independent non-dimensional height and time variables $\hat{h}$, and τ:

$$\hat{h} = z/H \,, \tag{2-28}$$

$$\tau = 4\pi^{\frac{2}{3}} c_0^{\frac{4}{3}} H^{\frac{2}{3}} A^{-1} F_0^{\frac{1}{3}} t \,. \tag{2-29}$$

Eq. (2-12), Eq. (2-13), Eq. (2-14) and Eq. (2-16) are then transformed respectively into the relations below:

$$\frac{d\hat{v}_p}{d\hat{h}} = \hat{m}_p \,, \tag{2-30}$$

$$\frac{d\hat{m}_p^4}{d\hat{h}} = 2\hat{v}_p \hat{b}_f \,, \tag{2-31}$$

$$\frac{d\hat{b}_f}{d\hat{h}} = \hat{v}_p \frac{\partial \hat{b}_e}{\partial \hat{h}} \,, \tag{2-32}$$

$$\frac{\partial \hat{b}_e}{\partial \tau} = \hat{v}_p \frac{\partial \hat{b}_e}{\partial \hat{h}} \,. \tag{2-33}$$

With the equations established above, a couple of critical solutions can be obtained with some assumptions (Worster and Huppert, 1983). First they assumed that the environment below the position of first front $\hat{h}_0$ in a confined region is uniform as the

environment in an open region. By that, the right-hand side of Eq. (2-32) is zero and then the solutions below are obtained:

$$\hat{b}_f = 1\,, \tag{2-34}$$

$$\hat{v}_p = \frac{3}{10}\left(\frac{18}{5}\right)^{\frac{1}{3}} \hat{h}^{\frac{5}{3}}\,, \tag{2-35}$$

$$\hat{m}_p = \frac{1}{2}\left(\frac{18}{5}\right)^{\frac{1}{3}} \hat{h}^{\frac{2}{3}}\,. \tag{2-36}$$

Secondly, to work out the position of first front at any time, the law of conservation was applied to relate the velocity of first front with the volume flux in the plume:

$$\frac{d\hat{h}_0}{d\tau} = -\hat{v}_p\big|_{\hat{h}_0}\,. \tag{2-37}$$

By integration, the position of first front at any time can then be expressed as:

$$\hat{h}_0 = \left[1 + \frac{1}{5}\left(\frac{18}{5}\right)^{\frac{1}{3}} \tau\right]^{-\frac{3}{2}}\,. \tag{2-38}$$

Finally, an approximation is introduced to assume that the flux of buoyancy $\hat{b}_f$ in the plume is linear between points of $\hat{h}=\hat{h}_0$ and $\hat{h}=1$, then a set of approximation solutions from Eq. (2-30), Eq. (2-32), and Eq. (2-31) are:

$$\hat{v}_p = \tilde{b}_f^{\frac{1}{3}}(\tau) \cdot \hat{v}_{p\infty}(h), \tag{2-39}$$

$$\hat{m}_p = \tilde{b}_f^{\frac{1}{3}}(\tau) \cdot \hat{m}_{p\infty}(h), \tag{2-40}$$

$$\hat{b}_e = \tilde{b}_f^{\frac{2}{3}}(\tau) \cdot \hat{b}_{e\infty}(h) - c(\tau), \tag{2-41}$$

where $(\hat{v}_p)_\infty$, $(\hat{m}_p)_\infty$, $(\hat{b}_e)_\infty$ are equal to $\hat{v}_p$, $\hat{m}_p$, and $\hat{b}_e$ at $\tau \to \infty$, $\tilde{b}_f(\tau)$and $c(\tau)$ are:

$$\tilde{b}_f(\tau) = \frac{1 - \hat{h}_0^{\frac{5}{3}}}{1 - \hat{h}_0}, \tag{2-42}$$

$$c(\tau) = 5\left(\frac{5}{18}\right)^{\frac{1}{3}} \left\{ \frac{\hat{h}_0^{-\frac{2}{3}} - 1}{1 - \hat{h}_0} + 3\tilde{b}_f^{\frac{2}{3}} \left[\frac{1 - \hat{h}_0^{-\frac{2}{3}}}{1 - \hat{h}_0} - \frac{5}{78}\frac{1 - \hat{h}_0^{\frac{4}{3}}}{1 - \hat{h}_0} - \frac{155}{56784}\frac{1 - \hat{h}_0^{\frac{7}{3}}}{1 - \hat{h}_0} + \cdots \right] \right\}. \tag{2-43}$$

The result from the approximate analytic solution mentioned above was validated by the numerical solution developed. This numerical method assumes that buoyancy of the environment, $\hat{b}_e$, is known at time τ and is represented by a step function (Germeles, 1975). That means at each time-interval $\Delta\tau$, the plume discharges a small amount liquid to add a new amplitude of $(\hat{b}_e)_{n+1}$ at each time step (see Figure 2-10 and Eq. (2-44)). At this same time step, the added amplitude of $(\hat{b}_e)_{n+1}$ squeezes the

stratification layer first formed moving downward from level $\hat{h}_i$ to a lower level $\hat{h}_i^{new}$ which gives Eq. (2-45). That is,

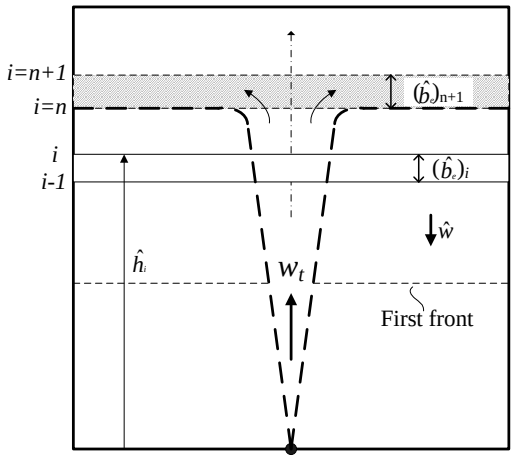

Figure 2-10: Sketch of step profile of $(b_e)_i$ at time $\tau+\Delta\tau$.

$$(\hat{b}_e)_{n+1} = (\hat{b}_e)_n + \left(\frac{\hat{b}_f}{\hat{v}_p}\right)_n , \tag{2-44}$$

$$\hat{h}_i^{new} = \hat{h}_i - \hat{h}' \cdot \hat{w} \cdot \Delta\tau , \tag{2-45}$$

where $\hat{h}'=(1-\hat{h})$, $\hat{w}$ is non-dimensional averaged downward vertical velocity, a normalised variable defined by Germeles (1975). The result of the numerical solution was shown to have matched closely well with the approximate analytic solution with a discrepancy less than 1%.

2.4 Buoyancy flow in a ventilated confined region

A ventilated confined region means it connects with the environment outside the region via openings made in the floor, walls, or ceiling of the space. These openings provide access for a continuous fluid exchange between the space and the environment. This case of ventilation flow can be categorised into two types: mixing ventilation and displacement ventilation as shown in Figure 2-11. Mixing ventilation normally has one opening made to the space. Light fluid leaves the space through upper half of the opening while the dense ambient fluid enters through the lower half. The dense fluid will then mix well with the fluid in the region as it descends towards the floor level. Displacement ventilation flow, on the other hand, has two openings made to the region with a lower opening for incoming ambient fluid and an upper opening for warm fluid. Ultimately, a stratification layer is formed next to the ceiling surface, but the formation of stratification layer is less as strong in the case of mixing ventilation.

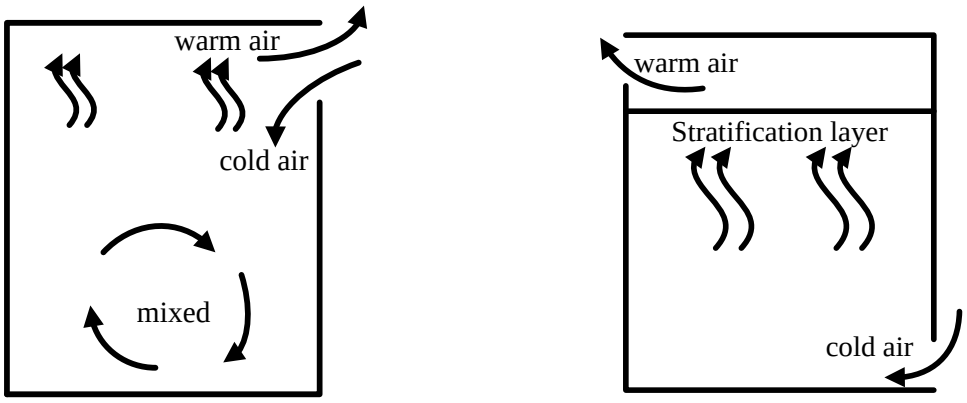

(a) (b)

Figure 2-11: Schematic of (a) mixing ventilation and (b) displacement ventilation.

2.4.1 Mixing ventilation

The investigation for these two types of ventilation flow was conducted by Linden et al (1990). For mixing ventilation flow, the position of the opening at ceiling level can result in different flow exchange through opening. For the exchange flows through an opening in the ceiling (lighter fluid in the enclosure with denser fluid above the ceiling opening), the flow will be unstable and does not have a quiescent distribution of flow patterns and pressure (Brown et al., 1963). There are mainly two forces working in opposite direction that drive the flow exchange through the horizontal opening: pressure and buoyancy forces. In the circumstance of zero pressure difference across the opening, the buoyancy force will lead to a bidirectional flow exchange. When the pressure difference increases and become dominant, the flow exchange becomes unidirectional flow (Jaluria et al., 1993).

In the case of flow exchange through the opening on the wall (vertical opening), the flow is described in terms of two-layer hydraulics (Dalziel and Laneserff, 1991). The flows exchange through the opening will be in opposite direction to each other with denser fluid flow into the space via lower part of the opening and lighter fluid in the upper part of the opening. The depth of each fluid layer is regarded the same when the flow is expected to be dissipationless.

While the light fluid leaves the space, the incoming dense flow descends towards the bottom of the space performing an inverse filling box flow pattern described previously (see Figure 2-12 (a)). The mixing process continues with a rising front of dense fluid until the front reaches the level of the opening. By this stage, the fluid in the region is considered well mixed and the stratification in the space becomes weak (Linden et al., 1990). In this case, the neutral level where the pressure inside is equal to the pressure outside is approximately at half of the height of the opening (see Figure 2-12 (b)).

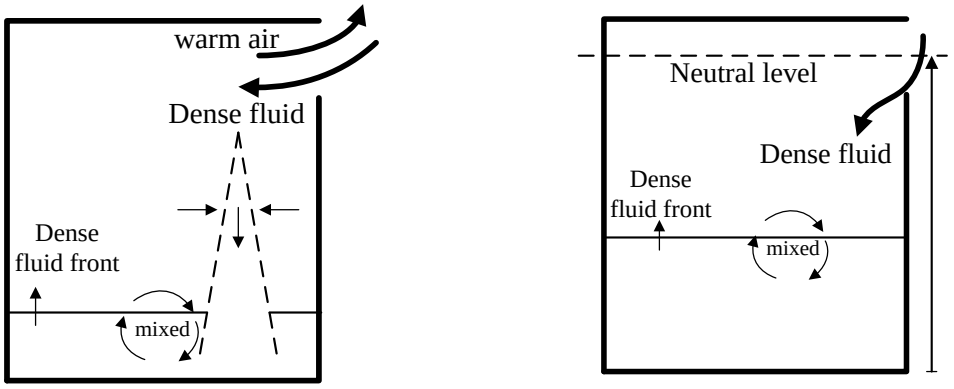

(a) (b)

Figure 2-12: Schematic of (a) incoming dense fluid (b) neutral level of mixing ventilation.

Based on the experiment conducted by Linden and Simpson (1985), the volume flux of an exchange flow via the vertical opening at neutral level is expressed as:

$$\dot{v} = c_d A (g' H_d)^{1/2} , \tag{2-46}$$

where A is the area of the opening, H_d is the height of the opening, g' is reduced gravity inside the opening where $\Delta\rho$ is the density difference between the space and the ambient, c_d is a discharge coefficient associated with the opening. As the flow exchange at the opening remains conservation, we have:

$$\frac{dg'}{dt} = -\frac{g'\dot{v}}{\boldsymbol{V}} = -\frac{c_d A H_d^{\frac{1}{2}} g'^{\frac{3}{2}}}{\boldsymbol{V}} . \tag{2-47}$$

By integration, Eq. (2-47) becomes:

$$\frac{g'}{g'_0} = \left(1 + \frac{t}{\tau}\right)^{-2} , \tag{2-48}$$

where

$$\tau = \frac{2\boldsymbol{V}}{c_d A}(g_0' H_d)^{-1/2} . \quad (2\text{-}49)$$

From the equations above, the buoyancy flux through the opening at certain time can be obtained by multiplying $\dot{v}$ and g'.

2.4.2 Displacement ventilation

For displacement ventilation, two openings are made: one at the top of the space and the other at the bottom of the space as mentioned above. The ambient fluid comes in from the opening at the floor level and the light fluid outflows through the upper opening. This forms vertical up-moving flows that drive the airflows. In addition, the part of the plume that spreads out towards sidewalls begins to descend from the upper part of the space and forms vertical flows moving downwards. These two opposite vertical flows will later bring the space to a steady state establishing an interface in the space.

The region below the interface and outside the plume is filled with dense ambient fluid; while the region above the interface and outside the plume is filled with lighter fluid. The vertical velocities of the fluid at both sides will reduce to zero when approaching to the interface, but with only the horizontal velocities left flowing towards the plume due to entrainment as shown in Figure 2-13 (a). To find this interface height and determine the flows in the space, a mathematical model for displacement ventilation flow is developed with couple of assumptions made.

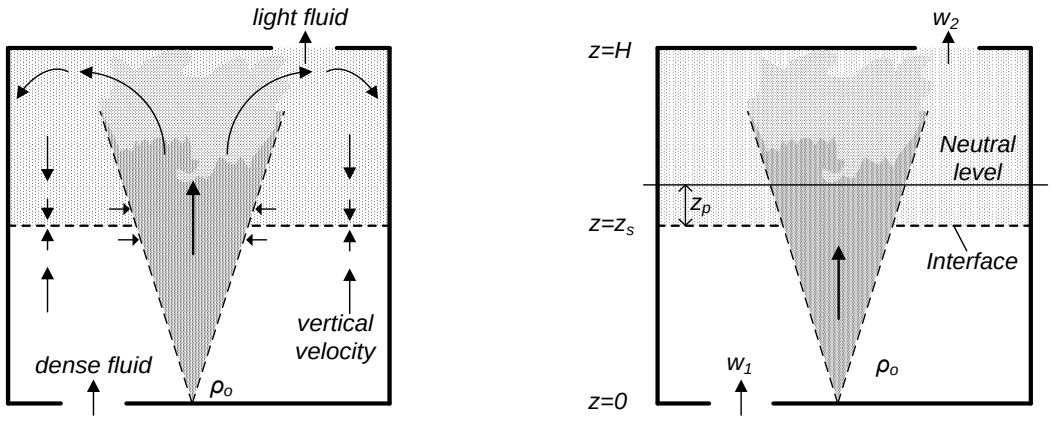

(a) (b)

Figure 2-13: Schematic of (a) displacement ventilation flow (b) neutral level.

Firstly, the incoming ambient flow is assumed to form a uniform layer of height z_s. Secondly, a neutral level is assumed to locate in between the interface and ceiling where the pressure inside and outside of the space is equal to the hydrostatic pressure. Hence, according to Bernoullis's theorem, the following two equations can be obtained:

$$w_1{}^2 = 2g' z_p \,, \tag{2-50}$$

$$w_2{}^2 = 2g'\big(H - z_s - z_p\big). \tag{2-51}$$

Due to the contraction following the fluid flow through the orifice, there will be a head drop along the streamline through the inlet vent. Hence equation (2-50) should be expressed as

$$w_1{}^2 = 2c_3 g' z_p \,, \tag{2-52}$$

where c_3 is a constant depend on the degree of sharpness in expansion at inlet vent. For incompressible flow, the incoming volume flux is equal to the volume flux leaving the space to satisfy the law of conservation, we have:

$$\dot{v} = w_1 A_1 = w_2 A_2 \,, \tag{2-53}$$

where A_1 and A_2 are the areas of opening at floor level and ceiling level respectively. Eliminating variable z_p from Eq. (2-51) and Eq. (2-52), together with Eq. (2-53) gives the volume flux through the space as

$$\dot{v} = A^*[g'(H - z_s)]^{1/2} \,, \tag{2-54}$$

where

$$A^* = \frac{A_1 A_2}{\left(\frac{1}{2}(A_2^2/c_3 + A_1^2)\right)^{1/2}} \,, \tag{2-55}$$

where A^* is considered as an "effective area" of the openings, as the value of A^* highly influenced by adjusting the value A_1 and A_2. The buoyancy flux then can be obtained by multiplying $\dot{v}$ and g', we have:

$$F = \dot{v} \cdot \mathrm{g}' \,. \tag{2-56}$$

To determine the position of the interface in the space, the velocity at the interface is matched with the buoyancy flux per horizontal area of the space A_s, we have:

$$\frac{dz_s}{dt} = \frac{F}{A_s} \,, \tag{2-57}$$

hence the height of the interface at each time can be expressed as:

$$\frac{z_s}{H} = 1 - \left(1 - \frac{t}{t_e}\right)^2 , \tag{2-58}$$

where t_e is the time for the space to empty, given as:

$$t_e = \frac{2A_s}{A^*}\left(\frac{H}{g'}\right)^{1/2} . \tag{2-59}$$

Sandbach and Lane-Serff (2011a) modified the step-profile equation proposed by Germeles (1975) to simulate the growing depth of the buoyant fluid layers by adding new buoyant layer next to the ceiling at each time step. The original approach models the plume flow in a close enclosure (Germeles, 1975); the modified step-profile takes the ventilation flow rate into account which then can be employed to model buoyancy driven flow both in ventilated and unventilated regions (Sandbach and Lane-Serff, 2011a). The equation accounts for the effects of ventilation flow, $\dot{v}$, and the strength of the buoyancy source (n_p v_p^*), the growing depth of the buoyant layer is given as:

$$z_j^{new} = z_j + \left(\dot{v} - n_p \cdot v_p^*\right) \cdot \Delta\tau , \tag{2-60}$$

where z_j is the vertical height of interface of the plume at time-step j, $\dot{v}$ is the non-dimensional ventilation flow rate, n_p is the number of equal strength sources, v_p^* is the non-dimensional volume flow rate of plume. Then the mathematical model from Linden et al. (1990) is adopted to calculate the ventilation flow rate which is:

$$\frac{{w_o}^2}{2c_o} = g_3'(H_3 - H_2) + g_2'(H_2 - H_N)\,, \tag{2-61}$$

$$\frac{{w_i}^2}{2c_i} = g_1'(H_1 - H_0) + g_2'(H_N - H_1)\,, \tag{2-62}$$

where c_o, c_i are velocity coefficient for upper and lower openings which are used to account the energy losses through openings. H_N is the height of the neutral level.

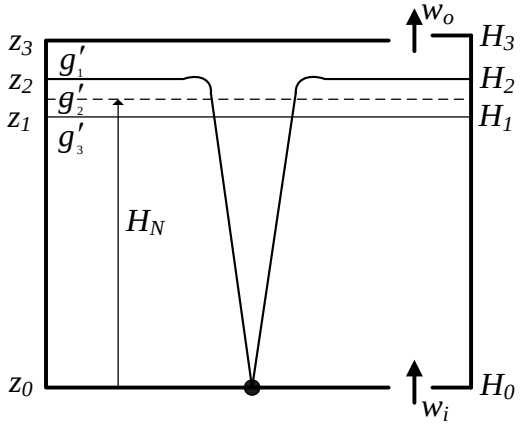

Figure 2-14: Schematic of displacement ventilation model.

According to the continuity principle, the volume flow rate leaving the space must equal the volume flow rate entering the space. By eliminating variable H_N in Eq. (2-61) and Eq. (2-62), a modified version of ventilation flow rate is then obtained:

$$\dot{v}^* = A_s^* \left[\sum_{j=1}^{n} g_j' \left(z_j - z_{j-1} \right) \right]^{1/2}, \tag{2-63}$$

where

$$A_s^* = \frac{\sqrt{2} A_o A_i}{\left(\left(A_o^2 / c_{d,o}^2 + A_i^2 / c_{d,i}^2 \right) \right)^{1/2}}, \tag{2-64}$$

where A_o, A_i are the areas of upper and lower openings, $c_{d,o}$ and $c_{d,i}$ are the discharge coefficients at outlet and inlet opening respectively. The results of the calculations show that the larger the coefficient the higher the interface. This is to be expected, as an increase in discharge coefficient will result in an increase in volume flow rate as Eq. (2-63) shows.

To simulate the thermal energy distribution within the enclosure, energy equations were derived to calculate the heat transfer at boundaries. This includes the heat conduction, convection and radiation at ceiling and floor (Sandbach and Lane-Serff, 2011b). The non-dimensional reduced gravity was defined as:

$$\hat{g} = \frac{g}{g'} \cdot \frac{T - T_0}{T_0}, \tag{2-65}$$

the temperature differences term were expressed by non-dimensional reduced gravity in the heat transfer equations.

The heat transfer that took place inside the space was grouped into six sections for analysis. These six sections are: (1) heat transfer from adjacent fluid layer to inner surface of ceiling, (2) radiative heat transfer from ceiling to floor, (3) heat conduction within the ceiling, (4) heat transfer from ceiling to surroundings, (5) heat transfer from floor to surroundings, and (6) finally the heat transfer between lower fluid layer, incoming cool air and the floor (see Figure 2-15).

The heat lost through sidewalls was neglected in this case. This is due to the much poorer insulation of the ceiling than that of the sidewalls. The sidewalls of the test room were constructed of two 0.015 m thick plasterboards separated by a 0.054 m air gap in between. The ceiling was constructed of plasterboard thickness 0.012 m. The thermal resistances of ceiling and sidewall can be calculated as follow:

$$R_{ceiling} = \frac{L}{k} = \frac{0.012}{0.17} = 0.07\,, \tag{2-66}$$

$$R_{sidewall} = 2 \times \frac{0.015}{0.17} + \frac{0.054}{0.0254} = 2.3\,. \tag{2-67}$$

With a much smaller heat resistance, the heat flux going through ceiling is larger than through the sidewalls. Hence, the thermal energy lost through sidewalls was neglected.

To start, the energy transfer from the plume layer adjacent to the inner surface of the ceiling forms the relation:

$$m_n c_{pa} \frac{d\hat{g}_n}{dt} = h_c A\left(\hat{g}_{c,1} - \hat{g}_n\right), \tag{2-68}$$

where m_n is the mass of the fluid, c_{pa} is the specific heat of the fluid next to the ceiling surface, $\hat{g}_n$ is the reduced gravity at nth layer of the fluid, $\hat{g}_{c,1}$ is the non-dimensional temperature difference of the ceiling surface, h_c is the convective heat transfer coefficient at the inner ceiling surface.

The heat transfer from ceiling to floor contains three heat transfer mechanisms: heat convection at ceiling surface, heat conduction within ceiling layer, and heat radiation from ceiling to floor which is approximated by using linear form. Thus the heat transfer equation is given as:

$$m_{c,1}c_{pc}\frac{d\hat{g}_{c,1}}{dt} = h_cA\left(\hat{g}_{c,1}-\hat{g}_n\right) + k_cA\frac{d\hat{g}_{c,1}}{dz} - h_rA\left(\hat{g}_{c,1}-\hat{g}_f\right), \qquad (2\text{-}69)$$

where $m_{c,1}$ is the first layer of ceiling mass, c_{pc} is the specific heat of the ceiling, k_c is the conductive heat transfer coefficient of the ceiling, $\hat{g}_f$ is non-dimensional temperature difference at the floor surface, h_r is the coefficient of approximate linearised radiative heat transfer equation.

The energy balance within the ceiling is purely heat conduction, so the heat-transfer equation is obtained based on Fourier's law:

$$\frac{d\hat{g}_{c,j}}{dt} = \frac{k_c}{\rho_c c_{pc}}\frac{d^2\hat{g}_{c,j}}{dz^2}, \qquad (2\text{-}70)$$

where $\hat{g}_{c,j}$ is non-dimensional temperature difference within ceiling at j^{th} ceiling layer.

For the heat transfer at the final ceiling layer next to the outer ceiling surface, it not only includes the heat conduction within the layer but also the heat radiation and convection to the surroundings. Hence, the energy balance equation is given as:

$$m_{c,n_t}c_{pc}\frac{d\hat{g}_{c,n_t}}{dt} = k_cA\frac{d\hat{g}_{c,n_t}}{dz} - h_{cr}A\left(\hat{g}_{c,n_t}-\hat{g}_0\right), \qquad (2\text{-}71)$$

where $m_{c,nt}$ is the mass of the n_t ceiling layer next to the surroundings, $\hat{g}_{c,nt}$ is the non-dimensional temperature difference at n_t ceiling layer, $\hat{g}_0$ is the reduced gravity of the

surroundings, h_{cr} is the sum of the heat convection coefficient and the coefficient of linearised radiation heat transfer equation. This approximate radiation heat transfer equation is made under the assumption that the temperature difference between outer ceiling surface and the surrounding is small. The error is estimated as follow:

For radiation heat transfer from outside ceiling surface to ambient, it is expressed as:

$$Q_{rad} = \sigma(T_c^4 - T_o^4). \tag{2-72}$$

To expand the equation, it becomes:

$$Q_{rad} = \sigma(T_c - T_o + T_o)^4 - T_o^4. \tag{2-73}$$

Let A=T_c-T_o then,

$$Q_{rad} = \sigma\{[A^4 + 4A^3T_o + 6A^2T_o^2 + 4AT_o^3 + T_o^4] - T_o^4\}. \tag{2-74}$$

If the temperature difference between ceiling surfaces and ambient temperature is small, A<1, then the radiation heat transfer equation can be approximated to:

$$Q_{rad} \approx \sigma 4T_o^3(T_c - T_o) + O(\Delta T^2)\,, \tag{2-75}$$

hence it can be seen that the error is second order so this is a first order approximation.

Apart from the radiative heat transfer taking place between ceiling and floor, there is also radiative heat transfer in between ceiling and sidewalls surfaces. The radiation heat transfer can be estimated by calculating the radiative heat resistances between ceiling and floor and the resistance between ceiling and sidewalls surfaces. The surface resistances can be expressed as:

$$R_{c-f} = \frac{1-\varepsilon}{A_c\varepsilon} + \frac{1}{A_cF_{c-f}} + \frac{1-\varepsilon}{A_f\varepsilon}\,, \tag{2-76}$$

$$R_{c-sidewall} = \frac{1-\varepsilon}{A_c\varepsilon} + \frac{1}{A_cF_{c-sidewall}} + \frac{1-\varepsilon}{A_{sidewall}\varepsilon}\,, \tag{2-77}$$

where F is radiative view factor, A_c is ceiling area, A_f is floor area, ε is the emissivity of the surfaces. The value of view factor can be determined by looking up the view factor chart. For aligned parallel rectangles, the value of view factor for ceiling and floor is given 0.48 and the view factor for sidewall is estimated 0.26 according to summation rule. Then the surface resistances of ceiling and sidewall become:

$$R_{c-f} = 0.0478 \times \frac{1-\varepsilon}{\varepsilon} + \frac{1}{0.48A_c}, \tag{2-78}$$

$$R_{c-sidewall} = 0.088 \times \frac{1-\varepsilon}{\varepsilon} + \frac{1}{0.26A_c}. \tag{2-79}$$

It can be seen that the radiative heat resistance at sidewall is larger than at floor. Beside there is a greater temperature difference between ceiling and floor; hence, the radiation heat transfer between ceiling and sidewalls was neglected in their study.

For the heat transfer at inner floor boundary, the experimental results showed that the majority of heat was lost through the ceiling (~ 53%), advection (~ 43%) and only a small amount of heat was lost through walls (~ 3.4%) (Sandbach, 2009). Hence, the temperature differences between the inner and outer surfaces of the floor are small. To reduce the complexity of the mathematical model, the floor as a whole is regarded as a single control volume, and its temperature is considered as the mean value of its inner and outer surface temperatures.

Hence, the equation for floor includes heat convection and radiation at fluid-solid inside interface; also heat conduction from outside floor surface to surroundings. The energy equation is given as:

$$m_f c_{pf} \frac{d\overline{\hat{g}_f}}{dt} = h_r A\left(\hat{g}_{c,1} - \hat{g}_f\right) - h_f A\left(\hat{g}_f - \hat{g}_1\right) - \frac{k_f A}{l_f}\left(\hat{g}_f - \hat{g}_0\right), \tag{2-80}$$

where k_f is the heat conduction coefficient, h_f is the heat convection coefficient of inner floor surface, l_f is the depth of the floor, $\overline{\hat{g}_f}$ is the mean temperature difference of the floor which is defined as $\overline{\hat{g}_f} = 0.5(\hat{g}_f + \hat{g}_0)$.

Lastly, the bottom fluid layer close to the floor is not only heated by the convection from the solid floor layer, but also cooled by the incoming ambient fluid. Therefore, the net heat transfer at this layer of fluid close to the floor can be expressed as:

$$m_1 c_{pa} \frac{d\hat{g}_1}{dt} = h_f A(\hat{g}_f - \hat{g}_1) - \rho_a c_{pa} \dot{v}(\hat{g}_1 - \hat{g}_0)\,, \tag{2-81}$$

where m_1 is the mass of the fluid at the bottom layer, ρ_a is the density of the fluid, $\dot{v}$ is the volume flow rate through the lower opening.

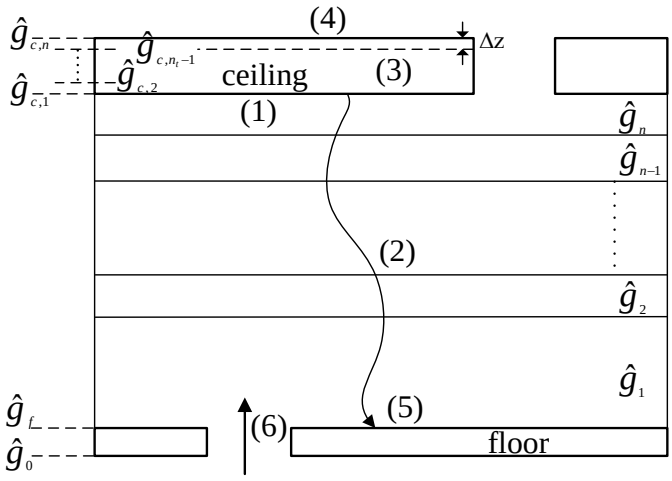

Figure 2-15: Schematic of heat transfer mechanisms considered for modelling (Sandbach and Lane-Serff, 2011b).

The heat transfer equations above were then solved by using a semi-implicit method, and compared with the experimental results. The simulation results were found to match generally well with the measurements, which proves that the effects of heat transfer at boundaries can not be ignored.

The radiative heat transfer between boundaries was also considered previously by several researchers in the studies of ventilation flows in an enclosure (Teodosiu et al.,

2014, Li et al., 1992). Rooney conducts study of buoyant plumes, especially strongly buoyant plumes.

A study of a displacement ventilation of a room containing a fire was conducted by Rooney and Linden (1997). This follows the research which develops a similarity solution for gaseous plumes in the non-Boussinesq regime (Rooney and Linden, 1996). In this non-Boussinesq plume model, the equation of buoyancy flux of the plumes is related to the convective power of the fire. The method for calculation of long-wave radiation of a downward movement of fluid was developed by Rooney (2005). This method considers the influence of solar irradiance (I_m) and clear-sky solar irradiance (I_c) to the actual atmospheric emissivity (ε) by modifying the empirical relationship of atmospheric emissivity of clear-sky (ε_c):

$$\varepsilon_c = 1.24(p_v/T)^{1/7} , \tag{2-82}$$

to

$$\varepsilon = \Phi + (1 - \Phi)\varepsilon_c , \tag{2-83}$$

where p_v is vapour pressure, T is near-surface temperature, and Φ is cloud fraction.

$$\Phi = (I_c - I_m)/I_c . \tag{2-84}$$

However, the air flows in between the surfaces in their studies were treated as transparent to radiation heat. That is, the radiation heat absorbed by the air was neglected. The simulation conducted in this study takes the radiative absorptivity of air into account.

2.5 The performance of turbulence models

Turbulence models are essential tools for solving fluid dynamic problems. Over the years, a wide range of turbulence models were developed for modelling different kinds of turbulent flows. However, none of those turbulent models could work well for every turbulent flow case. In fact, often only work well in one case but work poorly in another (Chen, 1995). To design a comfortable indoor environment requires accurate prediction of air velocity and temperature distribution in the ventilated space. Hence, the study of the performance of turbulence models in modelling different types of indoor ventilation cases becomes indispensable.

In this regard, a comparison of the performances of k-ε models for modelling indoor airflows was conducted by Chen (1995). The two-equation turbulence models were: standard k-ε model, low-Reynolds-number k-ε model, two-layer k-ε model, two-scale k-ε model, and a renormalization group (RNG) k-ε model. The characteristic of each turbulence model is addressed respectively:

The standard k-ε model is only suitable for modelling fully turbulent flows. For the region near to the walls where viscous effects become dominant, wall functions should be applied. The low-Reynolds-number k-ε model, on the other hand, performs well in predicting near-wall flows and wall heat transfer (Patel et al., 1985, Henkes and Hoogendoorn, 1989). However, low-Reynolds-number k-ε model requires a very refined mesh near walls to capture steep gradient of velocity and temperature in the near-wall region (Xu et al., 1998, Henkes et al., 1991).

The two-layer k-ε model is an alternative turbulence model which can provide satisfactory results with less mesh points and better convergence rates (Xu and Chen, 2001). In this two-layer k-ε model, the fully turbulent region is modelled by standard k-ε model and the near-wall viscosity-influenced region is resolved by a one-equation model. A one-equation model consists of a differential k equation and an algebraic expression for ε. That is,

$$\varepsilon = \frac{k^{3/2}}{l_t}. \tag{2-85}$$

A two-scale k-ε model is derived by dividing its turbulent kinetic energy spectrum k into two parts: production region k_p and the dissipation region k_t (as shown in Figure 2-16). The partition of k ($k = k_p + k_t$) is dependent on the energy transfer rate ε_p (energy transfer from production region to dissipation region), and dissipation rate ε_t. By this approach, unlike the traditional turbulence models, the model cannot only consider the generation and the dissipation turbulence kinetic energy but also the energy transfer between the partitioned regions (Kim and Chen, 1988).

This turbulence model is applied to solve the flow in the near wall region when the integrating energy in production region is equal to energy transfer rate ε_p across the two partitioned regions and $\varepsilon_p = \varepsilon_t$. Otherwise, the two-scale is used to solve high Reynolds-number flows.

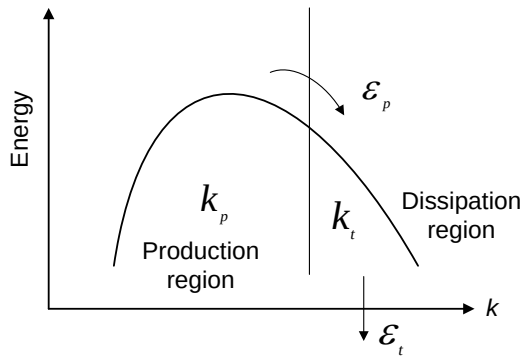

Figure 2-16: Schematic of two-scale turbulence model (Kim and Chen, 1988).

The renormalization group (RNG) k-ε model was derived based on the RNG method (Yakhot and Orszag, 1986). The RNG method is a self-similarity mathematical apparatus that allows a physical system to appear the same when viewed at different scales. In this turbulence model, the effect of the large scales on the eddies in the inertial range is represented by small-scale velocity fluctuations (Chen, 1995). The RNG k-ε model shares the same form as the standard k-ε model, only that all the coefficients of the turbulence model are different from the standard turbulence model. The coefficients were computed by the RNG method rather than determined from the experimental measurements.

There are four different types of ventilation flow simulated by Chen (1995): natural convection flow in an enclosed cavity domain with high temperature wall on one side and low temperature wall on the other, forced convection, mixed convection which is the combination of natural and forced convections, and lastly impinging jet flow. The study shows that the predictions of the mean velocity of each type of ventilation flow by five turbulence models are generally satisfactory; however, due to the assumption of isotropic turbulence, the prediction of the velocity fluctuation is less accurate. RNG turbulence model is in general shown to have better performance then any other k-ε turbulence models. For the other models, they could perform well in some particular cases but badly at the others. A summary of the performance of each turbulence model is shown in Table 2-1.

Of all the ventilation flows studied by Chen (1995), mixed convection is similar to displacement ventilation flow. However, the behaviour of a plume from a point source of buoyancy is different from the plume developed from a vertically distributed source of buoyancy in a ventilated enclosure. In addition, the air in the enclosure is considered as transparent to the radiation heat transfer. The simulations carried out in this thesis considered the radiative absorptivity of the air to study its effects on the redistribution of thermal energy in the enclosure.

Table 2-1: The performance of turbulence models for different types of flows.

Flow mode	Parameters	k-ε	LR k-ε	Two-layer	Two-scale	RNG k-ε
Natural convection	Mean vel.	B	A	B	B	B
	Temp.	B	D	B	B	B
Forced convection	Mean vel.	C	C	C	E	C
Mixed convection	Temp.	A	A	C	A	A
Impinging jet	Mean vel.	C	C	C	A	A

A=excellent, B=good, C=fair, D=poor, E=unacceptable (Chen, 1995).

In the case of displacement ventilation flows, the air movement in the room is often a combination of different level of turbulent. Therefore a standard k-ε model can not always be capable to capture every detail of them all and to give accurate predictive results. Hence, a modified standard k-ε model is needed. However, as mentioned above, the available turbulence models can perform well in one case but poorly in another other. Hence, the turbulence models should be selected accordingly to the condition of turbulent flows studied.

Another study on the performance of turbulence models in modelling ventilation flows in the room was carried out with four turbulence models: zero-equation model, k-ε model with damping functions, low-Reynolds number k-ε model, and large eddy model (Nielsen, 1998). The zero-equation model is a turbulence model where the eddy viscosity is expressed as a single algebraic function with no involvement of differential equations (this will be discussed further in Section 3.2). Applying Prandtl's mixing-length theory, the eddy viscosity of zero-equation model can be approximated as:

$$\mu_T \approx \rho \cdot {l_m}^2 \cdot \frac{\partial \bar{u}}{\partial y}, \tag{2-86}$$

where l_m is the mixing length. Introducing wall-friction velocity v^*, the equation becomes :

$$\mu_T \approx \rho \cdot l_m \cdot v^*, \tag{2-87}$$

where

$$v^* = \sqrt{\frac{\tau}{\rho}} \ . \tag{2-88}$$

Nielsen (1998) then estimates the eddy viscosity by the following form:

$$\mu_T = c_c \cdot \rho \cdot u_0 \cdot H, \tag{2-89}$$

where c_c is a constant, ρ is density, u_0 is a characteristic velocity, and H is a characteristic length. Chen and Xu (1998) also employed this form providing the value of constant c_c=0.03874. The Zero equation model was shown to give reasonably accurate results in their studies. Nielsen (1998) also suggests that Eq (2-89) can be used to obtain a eddy viscosity value for initial iterations in numerical modelling.

In the case of standard k-ε model, the eddy viscosity is determined by solving turbulent kinetic energy and the rate of dissipation transport equations. It is a popular turbulence model which gives satisfactory results in most cases. However, when considering damping effects on the turbulent stresses, it can not provide accurate predictions due to its isotropic property. Turbulent flows are usually anisotropic; i.e. the normal stresses ($\overline{u^2}$, $\overline{v^2}$, $\overline{w^2}$) are different. This phenomenon is even more

pronounced near the boundary region as the stresses can be selectively damped. In the case of buoyancy driven displacement ventilation flow problems, the damping effect of buoyancy is near the interface of stratification layer. As all normal Reynolds stresses are predicted to be equal to $\frac{2}{3}k$ by standard k-ε turbulence model, the turbulent normal stress perpendicular to the interface can not be accurately modelled. To model the eddy viscosity at the near boundary region, the damping functions are developed and blended in the turbulence models to reduce the eddy viscosity in those areas. The damping function f_{μ} placed in eddy viscosity term in this study is expressed as:

$$\mu_T = \rho \cdot c_\mu \cdot f_\mu \cdot \frac{k^2}{\varepsilon}. \tag{2-90}$$

There are a number of empirical damping functions, f_{μ}, which are devised by researchers to tackle different low Reynolds number and sublayer viscous flows at the near wall regions (Jones and Launder, 1972, Chien, 1982, Lam and Bremhorst, 1981). These functions are then blended with conventional k-ε turbulence model to form two-layer turbulence models and low-Reynolds number turbulence models.

Lastly for the large eddy model, the study conducted by Nielsen (1998) points out that unlike the Reynolds averaged form of the Navier-Stokes equations (RANS), the large eddy model can compute turbulent motions at larg scales providing detailed information on quantities of turbulent flows (Snegirev and Frolov, 2011). However it can be expensive and impractical for some industrial applications (Abdalla et al., 2007).

2.6 Studies of displacement ventilation flows

Studies of displacement ventilation flows have been carried out through experiments and CFD modelling works. A wide variety of turbulence and mathematical models were applied and developed to predict the airflow pattern, heat transfer, and temperature distribution in the enclosure. The results were then verified by measurements (Novoselac et al., 2006). A full-scale experiment of a room ventilated by displacement ventilation and simulations were carried out by Li et al. (1992). The room measured 4.2 m in length, 3.6 m in width, and 2.75 m in height with openings both at floor and ceiling level of side walls. The heat load placed in the room was providing energy up to 450 W. The results of the study showed that the vertical temperature profile of the room can be considerably affected by the heat conduction through side walls and the radiation between room surfaces (Li et al., 1992).

The amount of conduction heat loss through side walls can be influenced by the heat load inside the room, ambient temperature, and the heat transfer coefficient of the walls (Xu et al., 2001). This study conducted a displacement ventilation flow experiment with various combinations of heat loads and supply air temperatures. With the same amount of heat load placed in the room, the results of the experiment showed that the higher the supply air temperature the lower the room temperature gradient and vice versa (see Table 2-2). The stratification layer formed in the room is found to be stronger with lower supply air temperature and higher heat load.

The relation between the formation of stratified layer in the displacement ventilated enclosure and the intensity of the heat source were studied by conducting experiments and mathematical modelling (Fitzgerald and Woods, 2010). The transient evolution of formation of the stratification layers in the enclosure is closely related to the interior temperature and the strength of heat source. The study showed that a strong rising plume can always reach the ceiling and finally form a two-layer stratification at steady state. For a weaker heat source, it can initially reach the ceiling, but begin to intrude at the interface between incoming ambient air and the light original room air as the interface rises. This will then create a three-layer stratification, but eventually reach steady state forming a two-layer stratification.

Radiation heat transfer is another factor that affects the strength of the stratification layer. An experimental investigation was conducted and it shows that the floor of the room can be heated by radiative heat transfer from the ceiling to increase the rising flow (Li et al., 1993b). The amount of heat absorbed by the floor can be different with different surface radiative properties. The results show that the floor covered with aluminium sheets absorbs less thermal energy radiated from the ceiling. This causes a lower temperature at the floor surface and thus a lower rising flow. The floor covered with a black surface, on the other hand, absorbs a large amount of heat from the ceiling increases the temperature on the floor. This lowered the stratification level.

The study of displacement ventilation flow has also heavily relied on computational fluid dynamics (CFD) for simulations. CFD is a powerful tool that can predict the airflow, temperature distribution, and many physical properties of turbulent flows in the enclosure. However, conducting CFD modelling is one thing, getting satisfactory results is another. In order to obtain accurate results, it requires a good understanding of the factors which have influences on the accuracy of predictions and the performance of the turbulence models. A couple of studies below have given some critical information on getting accurate results.

An experiment of displacement ventilation flow with a mannequin as a heat source placed in the enclosure was conducted for validating CFD simulations results (Deevy, 2006). The main findings of the study indicate that a refined mesh near the mannequin (heat source) and a suitable turbulence model are essential for accurate simulation results. Also, a thermal radiation model should be applied to compute the absorptivity of the air for modelling buoyancy-driven flows. The humidity in the air can absorb radiative energy which affects the temperature distribution in the enclosure but was ignored in previous researches.

In order to obtain reasonably accurate simulation results without long-running time, a mesh-independence test should be carried out for determining the size of the grids. The test is to run the same case with finer mesh from one to another until no significant difference in between the results were found (Ji et al., 2007).

Table 2-2: The influence of supply air temperature and heat load on heat loss.

	Supply Air Temperature (^{0}C)				
	20			25	30
Total heat load (W)	100	200	400	200	200
Temp. Difference* (^{0}C)	1.6	3.1	5.7	1.8	1.1
Ventilation heat loss (W)	90	174	321	101	62
Conduction heat loss (W)	10	26	79	99	138

*temperature difference between supply air and exhaust air (Xu et al., 2001)

2.7 Radiation heat transfer

The studies on buoyancy-driven ventilation flows within enclosures have been carried out through experiments and mathematical modelling (Linden, 1999). There is a discrepancy between the modelling results and a full-scale natural ventilation measurements (Howell and Potts, 2002). The study indicates that the simple mathematical model does not consider thermal radiation and can not fully represent the scale of heat diffusion in the air. Hence, simulations were carried out using CFD technique to consider the effects of diffusion and radiation heat transfer.

There are two thermal radiation models available in Star CCM+: surface to surface radiation model and participating radiation model (CD-adapco, 2013). Surface to surface radiation model is an idealised radiation model that neglects the absorptivity of the participating medium and considers only the direct radiative heat transfer between surfaces (Gao et al., 2006). Participating radiation model, on the other hand, considers the absorption and emission of the medium in the enclosure. CFD simulation works were conducted to demonstrate the effect of the absorptivity of the air to the thermal distribution in the ventilated space (Chow and Holdo, 2010). The results show that considering absorptivity of the air increases the temperature in the lower zone and decreases the temperature in the upper zone. This leads to a weaker strength of stratification layer and hence a lower Richardson number. The Richardson number is an indication of the stability of stratification which is defined as:

$$R_i = -\frac{\frac{g}{\rho}\frac{d\rho}{dy}}{\left(\frac{\partial u}{\partial y}\right)^2}, \tag{2-91}$$

where ρ is density, u is velocity.

For non-grey gases, the absorptivity can vary considerably over the spectral range and the calculation for the value can be very complicated and tedious. In most cases, the gases were assumed to be grey to determine its absorptivity. However, the absorptivity of the air is often ignored.

Some studies considered the absorptivity of the air in modelling ventilation flows. The absorption coefficient used by Howell and Potts (2002) was obtained from a Planck-mean absorption coefficient chart of water vapour (Tien and Lee, 1982); however other absorption coefficients used by Chow and Holdo (2010) and Deevy and Gobeau (2006) were not elucidated in their studies. The coefficients used by the researchers are listed in the table below:

Table 2-3: Absorption coefficients used by previous researchers.

References	**Coefficients (m^{-1})**
(Deevy and Gobeau, 2006)	0.01
(Chow and Holdo, 2010)	0.05
	0.1
(Howell and Potts, 2002)	0.17

2.8 Absorption coefficient of gases

Gases can absorb and emit radiative energy as a result of electronic, vibrational, and rotational motions of their gas molecules. The energy state of the molecules rises and decreases when absorbing and releasing a passing photon. Hence, when radiation penetrates through a gas layer, its radiative intensity could be gradually attenuated by absorptivity and emissivity of the gas. After passing through the gas layer, the ratio between the leaving radiative energy of the radiation and the entering radiative energy is called transmissivity (τ_η) which is expressed as:

$$\tau_\eta = \frac{i_s(l)}{i_s(0)} = e^{-a_b l}\,, \tag{2-92}$$

where a_b is known as the absorption coefficient, l is the thickness of the gas layer. The amount of radiative energy absorbed by the gas layer is called the absorptivity and can be expressed as:

$$\alpha = 1 - \tau_\eta = 1 - e^{-a_b l}\,. \tag{2-93}$$

The radiative properties of gases however, unlike the solid medium, can vary irregularly and rapidly across a spectral range which makes it difficult to determine its absorptivity or emissivity. The absorptances of water vapour and carbon dioxide are the two strongest participant gases in the air. They were measured by Yamanouchi and Tanaka (1985) and Burch et al (1962) respectively and the absorptance of water vapour was later presented with high accuracy in the HITEMP database (Mossi et al., 2012). It can be seen from Figure 2-17 and Figure 2-18 that the absorptances of water vapour and carbon dioxide vary strongly across a certain range of spectrum.

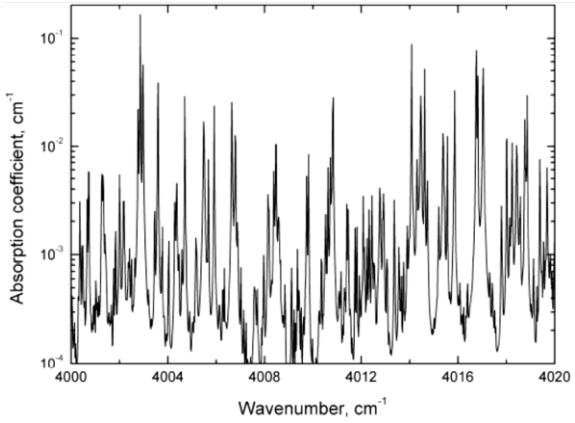

Figure 2-17: Absorption coefficient of water vapour (Mossi et al., 2012).

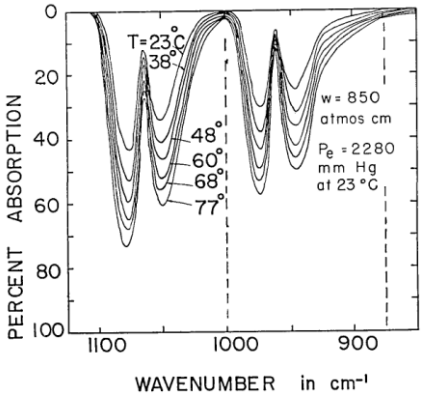

Figure 2-18: Absorption of carbon dioxide (Burch et al., 1962).

2.8.1 Planck mean absorption coefficient

From the figures shown above, the calculation of absorptivities or emissivities over a certain spectrum is clearly a formidable task. This has then led to the development of a number of approximate spectral models. These approximate models are known as (1) line by line model, (2) narrow band model, (3) wide band model, (4) global models (Modest, 2003). The Planck mean absorption coefficient is calculated by using the value computed from the narrow band model. The principle of the narrow band model is to replace the radiative properties rapidly varying across the spectrum by smoothed values appropriately averaged over a narrow spectral range,

$$\alpha_p \equiv \frac{\int_0^\infty i_b a_b d\lambda}{\int_0^\infty i_b d\lambda} = \frac{\pi}{\sigma T^4} \int_0^\infty i_b a_b d\lambda \,, \tag{2-94}$$

where i_b is the blackbody intensity, a_b is the absorption coefficient, T is the temperature, λ is the spectral wavelength, σ is the Stefan-Boltzman constant. Replacing the absorption coefficient with the averaged value from the narrow band model and making the assumption that Planck function varies little across each band, then Eq.(2-94) can be expressed as:

$$\alpha_p = \sum_j^N \left(\frac{\pi i_{b0}}{\sigma T^4}\right)_{\mathrm{j}} (a_{nb})_j \,, \tag{2-95}$$

where the Planck-mean absorption coefficient is the value of summation over all N bands, i_{b0} is the blackbody intensity at the centre of each band, a_{nb} is the band integrated absorption coefficient from narrow band model. The Planck-mean absorption coefficients were first presented by Tien (1968) based on the data of low-resolution experiments and were later obtained from high-resolution databases such as HITRAN96 (Rothman et al., 1998). In comparison with the coefficients calculated from HITRAN96, the data given by Tien were considered less accurate (Zhang and Modest, 2002).

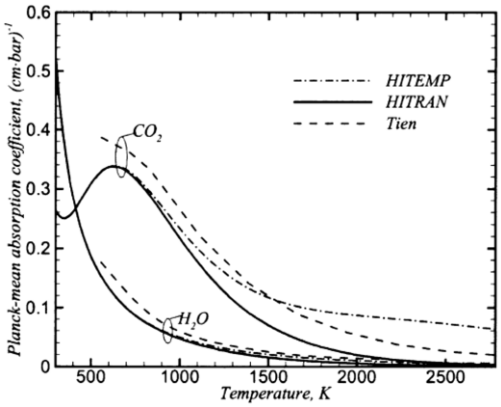

Figure 2-19: Planck-mean absorption coefficient of H_2O and CO_2 (Zhang and Modest, 2002).

2.8.2 Absorption coefficient of gas mixtures

In ventilation flows, radiation penetrates through air transferring radiative heat energy from surfaces to surfaces in the enclosure. Of all the gases in the air, CO_2 and H_2O are the main gases that cause the attenuation on radiative energy (Orloff et al., 1979). Laboratory experiments were conducted for measuring the absorptivity of the water vapour and water vapour-air mixture. The measurements were taken at temperature from 15 ^{0}C to 30 ^{0}C with relative humidity of 50-90%. The results show that the higher the water vapour pressure, the lower the transmittance of water vapour and water vapour-air mixture (McCoy et al., 1969).

For the gas mixture, the spectral line of each species can overlap over a certain region of spectrum and is important that must be accounted for. For the gas mixture of water vapour and carbon dioxide, they both have strong bands near the spectral region of 2.7 μm (Modest, 2003) and overlapped in the 2.7 and 15 μm regions of the spectrum. The emissivity of this gas mixture will be less than the sum of their individual emissivities as the result of the overlapping of these two spectral lines. An approximate overlap correction term was developed by Leckner (1972) and was used for estimating the emissivities and absorptivites of the non-grey gases mixture in the case of combustion (Modak, 1979). This simple algorithm avoids the tedious spectral calculation by using polynomial and power equations.

2.8.3 Radiation estimation in other contexts

On a larger scale, the radiation is also attenuated by the atmosphere when travelling from the sun to the earth as a result of absorption and scattering. The constituents of atmosphere are mainly O_2, O_3, H_2O and CO_2 gases. The radiation is absorbed by O_2 at wavelength about λ=0.76 μm, by gas O_3 in the wavelength region range from 0.3-0.4 μm and in ultraviolet region λ<0.3μm. The radiation absorbed by gases H_2O and CO_2 is mainly in the infrared region. The radiation can also be attenuated by air molecules or particles such as dust or water droplets due to scattering. The wavelength region in which the radiation is scattered depends on the size of the particles. Oxygen and nitrogen, for example, scatter radiation in short wavelength region due to their molecule sizes.

A study was carried out by Rooney (2005) investigating various methods for modelling atmospheric downwelling long-wave radiation (DWLW). The relation for DWLW is expressed as:

$$DWLW = \varepsilon\sigma T^4 , \tag{2-96}$$

where ε is atmospheric emissivity and it is a function of cloud fraction (Φ) and emissivity of clear-sky (ε_c):

$$\varepsilon = \Phi + (1 - \Phi)\varepsilon_c , \tag{2-97}$$

$$\varepsilon_c = 1.24(p_v/T)^{1/7} , \tag{2-98}$$

where p_v is vapour pressure, T is near-surface temperature. The cloud fraction Φ is determined by both solar irradiance (I_m) and clear-sky solar irradiance (I_c):

$$\Phi = (I_c - I_m)/I_c . \tag{2-99}$$

There are four methods used for estimating the cloud fraction. The first method introduced by Crawford and Duchon (1999) determines the clear-sky solar irradiance (I_c) as a function of solar zenith angle, sun-earth distance, atmospheric pressure and dewpoint; the solar irradiance (I_m) was obtained from measurements. The cloud fractions come from this method is compared with the other three methods; which determine cloud fraction by using data output from Laser cloud-base recorder (LCBR).

The comparison of the results from those methods show that the coefficients obtained from the methods using LCBR data are larger than those obtained from the method used by Crawford & Duchon (1999). This is because the methods using LCBR data can accurately estimate the long-wave radiation at all times; however, the method used by Crawford & Duchon (1999) can only be accurate at daytime. Furthermore, it considers only the cloud fraction but not cloud height.

2.9 Summary

This chapter reviews the earlier studies on buoyancy flow in an unventilated and ventilated confined region, the performance of turbulence models, the factors that influence the thermal distribution in a displacement ventilated space, and the radiative absorptivity of participating medium.

A time-dependent density profiles mathematical model was developed by Worster and Huppert (1983) for buoyancy flow in an unventilated confined region. The expression was developed based on the conservation laws with three assumptions such as top-hat profile. The expression models the fluid density profiles behind the interface which varying with time in a filling box region.

A mathematical model developed by Sandbach and Lane-Serff (2011a) was used to model the transient vertical stratification in the buoyancy-driven displacement ventilation flow region. The model accounts for the heat transfer at boundaries which include heat conduction, convection and radiation from ceiling to floor surfaces. The simulation results were then compared with the measurements conducted by Sandbach and Lane-Serff (2011b).

A comparison of performance of five turbulence models was conducted by Chen (1995). The analysis shows that every turbulence model can perform well for a particular type of airflow, but poor at others. For a ventilation flow region with stagnant area, the damping effect should be taken into account for accurate predicted results.

Some full-scale experiments and CFD modelling works were carried out to study buoyancy-driven displacement ventilation flow. The results show that there are a number of factors can affect the thermal distribution in the ventilated region such as supply air temperatures (Xu et al., 2001), opening size of the room (Fitzgerald and Woods, 2010), and radiation heat transfer (Chow and Holdo, 2010).

The participating medium can attenuate the penetrating radiation by absorption and emission. However, the calculation of its radiative properties of the medium can be complex as it varies irregularly and rapidly across the spectrum (e.g. Mossi et al,. 2012). This then led to the development of a number of approximate band models to compute the absorptivity of the medium.

Based on the previous studies regarding ventilation flows and radiation heat transfer, this study takes a step further to investigate the techniques for modelling buoyancy-driven displacement ventilation flows and the effects of radiative absorptivity of the air on thermal distribution in the space. The next chapter sets out the theory of each turbulence model used for modelling displacement ventilation flows, the radiative heat transfer between surfaces and participating medium, and the method for determining absorption coefficients.

CHAPTER THREE

3 Underlying Theory

3.1 Context

The study of buoyancy-driven displacement ventilation flow involves solving both fluid dynamics and heat transfer problems. The formation of ventilation flow is the result of density differences produced by the local heat sources. The ventilation flow and the heat transfer at boundaries determine how the heat is distributed in the enclosure. Hence, this chapter details what turbulence models are used and what heat transfer mechanisms are involved for modelling buoyancy-driven displacement ventilation flows. The method used to calculate the absorption coefficient of air is also presented for estimating the amount of heat attenuated by the absorptivity of the air.

3.2 Turbulence models

In the case of buoyancy-driven ventilation flows, plume flow develops into turbulent flow shortly after rising from heat source and drives ventilation flows in the enclosure. These flows are random, 3 dimensional, and varying with time. In order to model these turbulent flows, Reynolds-averaged Navier-Stokes equations and a turbulence model which describe the physical behaviour of turbulent flows is employed.

Turbulence model is introduced to approximate the Reynolds stresses in the Reynolds-averaged Navier-Stokes equations. One of the most used turbulence models, eddy-viscosity model, assumes that the Reynolds stress can be expressed in a form that is similar to viscous stress. The eddy viscosity can be determined either by turbulence length scale or turbulent quantities obtained through solving differential transport equations.

Direct numerical simulation (DNS) can be another option available for simulating turbulent flows. The difference between DNS and the turbulence model is that DNS solves the Navier-Stokes equations directly without using any turbulence model. However, in order to cover all scales of turbulence from large to small (Kolmogorov microscales), a refined mesh is needed which requires immense computational resource to carry out the calculation. The Kolmogorov length scale is defined as:

$$K_l = \left(\frac{\nu\delta}{U}\right)^{1/4}, \tag{3-1}$$

where δ is the shear layer thickness, ν is kinematic viscosity and U is the airflow velocity. In the case studied in this thesis, ν=1.22x10^{-5} (m^2 s^{-1}), U=0.308 (m s^{-1}), δ=0.05 (m), then k_l =2.3x10^{-4} (m). As the size of the computational domain is 41.58 m^3, using DNS will need to construct 3.2x10^{12} mesh grids and thus require huge amount of computational resources.

Zero-equation model

As mentioned in the previous sections, flow motions in the flow field can be described solely by the continuity equation and Navier-Stokes equation. However, for turbulent flows, each velocity component can vary rapidly at random with time and space. It is then difficult to make exact analysis. Hence, a time averaging procedure postulated by Reynolds (1895) is introduced to separate the quantities into time-averaged and fluctuating parts. The velocity is then expressed as:

$$u = \bar{u} + u', \qquad v = \bar{v} + v', \qquad w = \bar{w} + w', \tag{3-2}$$

where $\bar{u}$, $\bar{v}$, $\bar{w}$ are the time-averaged velocities, u', v', w' are the fluctuating velocities. The continuity and Navier-Stokes equations can be converted into Eq. (3-3), Eq. (3-4), Eq. (3-5), and Eq. (3-6) respectively. The Eq. (3-4) - Eq. (3-6) are known as Reynolds-averaged Navier-Stokes equations (RANS); the turbulent fluctuation parts, $-\rho\overline{u_i' u_j'}$, are known as Reynolds-stress:

$$\frac{\partial \bar{u}}{\partial x}+\frac{\partial \bar{v}}{\partial y}+\frac{\partial \bar{w}}{\partial z}=0\,, \tag{3-3}$$

$$\begin{aligned}\rho\left(\frac{\partial \bar{u}}{\partial t}+\bar{u}\frac{\partial \bar{u}}{\partial x}+\bar{v}\frac{\partial \bar{u}}{\partial y}+\bar{w}\frac{\partial \bar{u}}{\partial z}\right)&\\ =-\frac{\partial \bar{p}}{\partial x}+\mu\nabla^2\bar{u}&\\ +\left[\frac{\partial}{\partial x}(-\rho\overline{u'u'})+\frac{\partial}{\partial y}(-\rho\overline{u'v'})+\frac{\partial}{\partial z}(-\rho\overline{u'w'})\right],&\end{aligned} \tag{3-4}$$

the equations for *y* and *z* directions are as follow:

$$\begin{aligned}\rho\left(\frac{\partial \bar{v}}{\partial t}+\bar{u}\frac{\partial \bar{v}}{\partial x}+\bar{v}\frac{\partial \bar{v}}{\partial y}+\bar{w}\frac{\partial \bar{v}}{\partial z}\right)&\\ =-\frac{\partial \bar{p}}{\partial y}+\mu\nabla^2\bar{v}&\\ +\left[\frac{\partial}{\partial x}(-\rho\overline{v'u'})+\frac{\partial}{\partial y}(-\rho\overline{v'v'})+\frac{\partial}{\partial z}(-\rho\overline{v'w'})\right],&\end{aligned} \tag{3-5}$$

$$\begin{aligned}\rho\left(\frac{\partial \bar{w}}{\partial t}+\bar{u}\frac{\partial \bar{w}}{\partial x}+\bar{v}\frac{\partial \bar{w}}{\partial y}+\bar{w}\frac{\partial \bar{w}}{\partial z}\right)&\\ =-\frac{\partial \bar{p}}{\partial z}-\rho g+\mu\nabla^2\bar{w}&\\ +\left[\frac{\partial}{\partial x}(-\rho\overline{w'u'})+\frac{\partial}{\partial y}(-\rho\overline{w'v'})+\frac{\partial}{\partial z}(-\rho\overline{w'w'})\right],&\end{aligned} \tag{3-6}$$

where *u*, *v* and *w* are velocity at x, y, z direction respectively, ρ is density, *p* is the pressure, μ is dynamic viscosity. In the RANS equations, Reynolds-stresses are unknowns and needed to be modelled. To close the system, eddy viscosity hypothesis is introduced to specify the Reynolds stress. That is,

$$-\rho\overline{u_i'u_j'}=\mu_T\left(\frac{\partial \bar{u}_i}{\partial x_j}+\frac{\partial \bar{u}_j}{\partial x_i}\right), \tag{3-7}$$

where μ_T is the eddy viscosity. The eddy viscosity has the same dimension of dynamic viscosity (μ), but it is not a physical property of fluid, it depends upon the condition of turbulent eddies. The kinematic eddy viscosity is defined as the product of a length scale and a velocity scale:

$$\nu_T = u_0 \cdot l_0 \,, \tag{3-8}$$

where u_0 represents the magnitude of fluctuating velocity and l_0 represents the size of eddy. To specify the velocity scale u_0, Prandtl mixing-length hypothesis is introduced. In the case of simple shear, the mixing-length model defines the fluctuating velocity to be the product of mixing-length and the mean velocity gradients:

$$u_0 = l_m \cdot \frac{\partial \bar{u}}{\partial y}. \tag{3-9}$$

Hence, the Reynolds stress can be expressed as:

$$-\rho\overline{u'v'} = \mu_T \frac{\partial \bar{u}}{\partial y} = \rho l_m^2 \left(\frac{\partial \bar{u}}{\partial y}\right)^2 , \tag{3-10}$$

where l_m is the mixing length. This length scale represents the distance that a gas molecular displaced by turbulent eddy. The result of this displacement is a velocity difference by an amount u_0 as given in Eq. (3-9). The length scale can be different from each flow type; therefore it needs to be specified in advance before starting to obtain the solution.

One-equation model

Although the algebraic model can be useful for solving free shear layers such as wakes, jets, and mixing layers, it is still an incomplete turbulence model without specifying mixing length in advance. In addition, it does not account for the turbulent energy and dissipation of the turbulence. It assumes the turbulence is in a local equilibrium state. The mixing length hypothesis could give zero values to eddy viscosity when the velocity gradient is zero, which is in conflict with reality. Therefore, one-equation turbulence model is developed to account for the turbulent kinetic energy and the dissipation of the turbulence.

First of all, the model defines turbulent kinetic energy *k* as:

$$k = \frac{1}{2} \cdot \left(\overline{u'^2} + \overline{v'^2} + \overline{w'^2} \right). \tag{3-11}$$

By conducting the process of Reynolds averaging, the transport equation for turbulent kinetic energy using Einstein summation convention can be derived to give:

$$\frac{\partial k}{\partial t} + \bar{u}_j \frac{\partial k}{\partial x_j} = -\overline{u_i' u_j'} \frac{\partial \bar{u}_i}{\partial x_j} - \varepsilon + \frac{\partial}{\partial x_j} \left(\nu \frac{\partial k}{\partial x_j} - \overline{\left(\frac{p'}{\rho} + \frac{1}{2} u_i' u_i' \right) u_j'} \right), \tag{3-12}$$

where the eddy viscosity is defined to be a correlation with turbulent kinetic energy and turbulence length scale. That is,

$$\mu_T = (const.) \cdot \rho \cdot k^{\frac{1}{2}} \cdot l_t \,, \tag{3-13}$$

where l_t is the turbulence length scale. For the dissipation of the flow, Prandtl postulated that it is proportional to the turbulent kinetic energy *k*. By dimensional reasoning, the dissipation is given as:

$$\varepsilon = c_1 \cdot k^{\frac{3}{2}} / l_t \,, \tag{3-14}$$

where c_1 is an empirical constant. Approximating the last term of Eq. (3-12) on the right-hand side to be a gradient diffusion term, that is,

$$-\overline{u_j' \left(\frac{p'}{\rho} + \frac{1}{2} u_i' u_i' \right)} \approx \Gamma_f \frac{\partial k}{\partial x_j}, \tag{3-15}$$

where Γ_f is the turbulent diffusivity and is proportional to eddy viscosity:

$$\Gamma_f = \frac{\nu_T}{\sigma_k} \,, \tag{3-16}$$

where σ_k is turbulent Schmidt number. Hence, the one-equation model can be re-expressed as follow:

$$\frac{\partial k}{\partial t} + \bar{u}_j \frac{\partial k}{\partial x_j} = -\overline{u_i' u_j'} \frac{\partial \bar{u}_i}{\partial x_j} - c_1 \frac{k^{3/2}}{l_t} + \frac{\partial}{\partial x_j} \left(\left(\nu + \Gamma_f \right) \frac{\partial k}{\partial x_j} \right). \tag{3-17}$$

Two-equation model

A two-equation model is formed by adding a second transport equation to one-equation model. This second transport equation is solving for turbulence property such as dissipation rate ε, frequency ω, time scale τ or turbulence length scale l_t. With a second transport equation included, the two-equation model can predict the properties of a turbulent flow without the need of knowing the turbulence structure in advance. Hence, the two-equation model is the simplest complete model of turbulent flow problems.

3.2.1 Standard k-ε model

Among all two-equation models, k-ε is the most popular turbulence model which is formed by turbulent kinetic equation and dissipation transport equations. The standard k-ε model is as follows:

$$\frac{\partial k}{\partial t} + \bar{u}_j \frac{\partial k}{\partial x_j} = D_k + D_b - \varepsilon + \frac{\partial}{\partial x_j}\left(\left(\nu + \Gamma_f\right) \frac{\partial k}{\partial x_j} \right) , \tag{3-18}$$

$$\begin{aligned} &\frac{\partial \varepsilon}{\partial t} + \bar{u}_j \frac{\partial \varepsilon}{\partial x_j} = \\ &c_{\epsilon 1} \frac{\varepsilon}{k} (D_k + c_{\epsilon 3} D_b) - c_{\epsilon 2} \frac{\varepsilon^2}{k} + \frac{\partial}{\partial x_j}\left((\nu + \nu_T/\sigma_\epsilon) \frac{\partial \varepsilon}{\partial x_j} \right), \end{aligned} \tag{3-19}$$

where σ_ϵ is the turbulent Schmidt number, ν_T is kinematic eddy viscosity, D_k is turbulence production term, D_b is buoyancy production term. The turbulent and buoyancy production terms are defined as follow:

For turbulence production term D_k, in the case of incompressible and non-supersonic flow, it is given as:

$$D_k = -\overline{u_i' u_j'} \frac{\partial \overline{u}_\iota}{\partial x_j} = \nu_T \boldsymbol{S}^2 , \tag{3-20}$$

where $\boldsymbol{S}$ is the result of inner product of two mean rate of strain tensors:

$$\boldsymbol{S} = \sqrt{2 S_{ij} : S_{ij}} , \tag{3-21}$$

where

$$S_{ij} = \frac{1}{2}\left(\frac{\partial \overline{u_i}}{\partial x_j} + \frac{\partial \overline{u_j}}{\partial x_i}\right). \tag{3-22}$$

For buoyancy production term D_b:

$$D_b = \beta \frac{\nu_T}{\sigma_t}\left(\frac{\partial T}{\partial x_i} \cdot g_i\right), \tag{3-23}$$

where g_i is the gravitational vector, T is temperature, σ_t is the turbulent Prandtl number, β is the coefficient of thermal expansion which is defined as:

$$\beta = -\frac{1}{\rho}\left(\frac{\partial \rho}{\partial T}\right)_p. \tag{3-24}$$

In the case of buoyancy flow, the density of the airflow varies with temperature. By the equation of state, under the condition of constant pressure:

$$\frac{\rho_r - \rho}{\rho_r} = \frac{(T - T_r)}{T}, \tag{3-25}$$

where ρ_r and T_r are the density and temperature at the reference state. By representing density in Taylor series gives:

$$\rho = \rho_r + \frac{\partial \rho}{\partial T}(T - T_r) + \frac{\partial^2 \rho}{\partial T^2}(T - T_r)^2 + \cdots. \tag{3-26}$$

As the temperature difference (T-T_r) is relatively small compare to the reference temperature T_r, the density can be approximated as follow by introducing Eq. (3-24):

$$\rho = \rho_r - \rho_r \beta (T - T_r) + O(\Delta T^2) \,. \tag{3-27}$$

In the case of ideal gas and at constant pressure, the volume expansion coefficient is equivalent to the inverse of the temperature. That is,

$$\beta = \frac{1}{T} \,. \tag{3-28}$$

The turbulent kinematic viscosity term ν_T is defined as:

$$\nu_T = c_\mu \cdot k^2/\varepsilon \,. \tag{3-29}$$

There is still no consensus on the specification of the coefficient $c_{\epsilon 3}$. In the CFD commercial programme StarCCM+, the coefficient by default is as defined by Henkes et al. (1991) as follow:

$$c_{\epsilon 3} = \tanh \frac{|w_b|}{|u_b|}, \tag{3-30}$$

where w_b is the velocity parallel to gravitational vector g_i, and u_b is the velocity perpendicular to g_i. This equation satisfies the condition that the coefficient is zero outside natural convection boundary layers and is set to 1 elsewhere (Rodi, 1993). That is,

$$c_{\epsilon 3} = \begin{cases} 1 & for\ D_b \geq 0 \\ 0 & for\ D_b < 0 \end{cases} . \tag{3-31}$$

The rest of the turbulent numbers and coefficients are specified in Table 3-1.

Table 3-1: The coefficients and numbers of standard k-ε turbulence model.

$c_{\epsilon 1}$	$c_{\epsilon 2}$	c_{μ}	σ_k	σ_{ϵ}
1.44	1.92	0.09	1.0	1.3

3.2.2 Realisable k-ε model

The realisable k-ε model is different from the standard k-ε model by a mathematical constraint which requires the Reynolds normal stress to be always positive. The normal stress is expressed as:

$$\overline{u^2} = \frac{2}{3}k - 2\nu_T \frac{\partial U}{\partial x} \ , \tag{3-32}$$

substitute ν_T with Eq. (3-29), the mathematical constraint should be satisfied to keep normal stress positive. That is,

$$c_{\mu} \frac{\partial U}{\partial x} < \frac{\varepsilon}{3k} \ . \tag{3-33}$$

To do this, the coefficient c_{μ} is defined to be a variable and is a function of turbulence properties and mean strain rate. Apart from this, the differential dissipation rate equation of the standard k-ε model was also modified. These formulations can improve the performance of k-ε turbulence model on predicting rotating homogeneous shear flows, jets flows, boundary layer flows, recirculation and separated flows.

In this model, the turbulent kinetic transport equation is the same as standard k-ε model. The turbulence production term D_k in the dissipation rate equation is removed. The coefficient c_μ in the eddy viscosity equation is defined as a variable to ensure the realisability for modelling the cases with large mean strain rate (Shih et al., 1995a). Thus, c_μ varies from one case to another.

$$\frac{\partial \varepsilon}{\partial t} + \bar{u}_j \frac{\partial \varepsilon}{\partial x_j} = \left[\frac{\varepsilon}{k} c_{\epsilon 1} c_{\epsilon 3} D_b - \frac{\varepsilon^2}{k + \sqrt{\nu \varepsilon}} c_{\epsilon 2}\right] + \frac{\partial}{\partial x_j}\left((\nu + \nu_T/\sigma_\epsilon)\frac{\partial \varepsilon}{\partial x_j}\right), \tag{3-34}$$

where $\nu = \mu/\rho$. The buoyancy production D_b and eddy viscosity μ_T are defined identically to the corresponding terms in the standard k-ε model, c_μ is a variable which is defined as:

$$c_\mu = \frac{1}{d_0 + d_s \cdot U^* \cdot \frac{k}{\varepsilon}}\ , \tag{3-35}$$

where

$$U^* = \sqrt{S_{ij} : S_{ij} + \tilde{\Omega}_{ij} : \tilde{\Omega}_{ij}}\ , \tag{3-36}$$

where S_{ij} is the strain rate tensors as defined in Eq. (3-22) and Ω_{ij} is the rotation rate tensor given as (Shih et al., 1995b):

$$\tilde{\Omega}_{ij} = \Omega_{ij} - 2\,\varepsilon_{ijk}\omega_k\ , \tag{3-37}$$

where

$$\Omega_{ij} = \overline{\Omega_{ij}} - \varepsilon_{ijk}\omega_k \,, \tag{3-38}$$

where ω_k is the angular velocity. The parameter d_s is defined as:

$$d_s = \sqrt{6}\cos\theta \,, \tag{3-39}$$

$$\theta = \frac{1}{3}acos\left(\sqrt{6}W_0\right), \tag{3-40}$$

$$W_0 = \frac{S_{ij}S_{jk}S_{ki}}{\sqrt{S_{ij}S_{ij}}^3}, \tag{3-41}$$

where S is the mean strain rate tensor which is the same as Eq. (3-21). The value of d_0 is determined based on the type of flow selected for the calibration. For boundary layer type of flow which accounts for the flow in the inertial sublayer, the calibration of the model coefficient d_0 is given as d_0=4.0 (Shih et al., 1995a). The turbulent numbers $c_{\epsilon 1}$ is defined as:

$$c_{\epsilon 1} = max\left(0.43, \frac{\eta}{5+\eta}\right), \tag{3-42}$$

where

$$\eta = \frac{\boldsymbol{S}k}{\varepsilon}. \tag{3-43}$$

The other coefficients are specified in Table 3-2.

Table 3-2: The coefficients of realisable *k*-ε turbulence model.

$C_{\varepsilon 2}$	σ_k	σ_ϵ
1.9	1.0	1.2

3.2.3 Realisable two-layer *k*-ε model

In the case of buoyancy-driven displacement ventilation flows, the level of turbulence of airflows can vary from high speed plume flow produced by heat sources to low-Reynolds laminar flow in the near-wall regions. Apart from those types of airflows, there are airflows that undergo relaminarisation due to the damping effects from the walls and stable stratification layer which causes the airflows to relaminarise (Noto and Nakai, 2008). Therefore, the airflows of this case are rather complex and using standard *k*-ε turbulence model may not be able to provide satisfactory results (Murakami et al., 2000). Instead, it is clear to see that employing a turbulence model equipped with damping functions is the solution for obtaining more accurate predictive-results of this kind of airflows (Nielsen, 1998).

The realisable two-layer *k*-ε turbulence model is a combination turbulence model set which considers the damping effects and thus performs well in modelling the flows at near-wall regions. It consists of a realisable *k*-ε turbulence model and a pair of turbulence length scale equations. The model is then controlled by a blending function which can switch the model to realisable *k*-ε turbulence model when solving flows far from the walls and to turbulence length scale equations when solving flows at near-wall regions.

When solving the flows in the near-wall region, the turbulence kinetic energy, *k*, is solved by Eq. (3-18) but the buoyancy term D_b is replaced by the function below (Chien, 1982):

$$D_b = -2\mu\frac{k}{y^2}, \tag{3-44}$$

where y is the normal distance to the closest solid boundary.

Instead of solving the differential equation for dissipation rate ε, the dissipation rate at the near-wall region is calculated by an algebraic equation defined as:

$$\varepsilon = \frac{k^{\frac{3}{2}}}{l_t}, \tag{3-45}$$

where l_t is the dissipation length scale and is also a function of variable *y*. Hence, the turbulence model used to solve the flow in the region near to the wall boundary is expressed as:

$$\frac{\partial k}{\partial t} + \bar{u}_j\frac{\partial k}{\partial x_j} = D_k - 2\nu\frac{k}{y^2} - \frac{k^{\frac{3}{2}}}{l_t} + \frac{\partial}{\partial x_j}\left(\left(\nu + \Gamma_f\right)\frac{\partial k}{\partial x_j}\right). \tag{3-46}$$

When solving the flows at outer near-wall region, the kinetic energy is still solved by Eq.(3-46), but the dissipation rate is calculated by the original equation of the realisable *k*-ε model, Eq. (3-34). In Star-CCM+, the equation of eddy viscosity μ_T of the two-layer *k*-ε turbulence model is then computed by the function below:

$$\mu_T = \phi\cdot\mu_T|_{k-\varepsilon} + (1-\phi)\cdot\mu_t|_{two-layer}, \tag{3-47}$$

where $\mu_T|_{k\text{-}\varepsilon}$ is calculated by Eq. (3-29) from standard k-ε model, the two-layer eddy viscosity $\mu_t|_{two\text{-}layer}$ is calculated by the equation below:

$$\mu_t|_{two-layer} = \sqrt{\overline{v'v'}} \cdot l_v \,, \tag{3-48}$$

where ϕ is the blending function and l_v is the viscosity length scale which is a function of variable y. With this two-layer eddy viscosity equation, the transition can be controlled from one layer to another by determining the value of ϕ. In this case, Eq. (3-47) is applied to outer region when ϕ=1, and to near-wall region when ϕ=0. The blending function ϕ in Star-CCM+ is defined the same as the equation developed by Jongen (1998):

$$\phi = \frac{1}{2} \cdot \left[1 + \tanh\left(\frac{Re_y - Re_y^*}{c_A}\right)\right], \tag{3-49}$$

where Re_y is the Reynolds number based on the normal distance to the closest solid boundary y and $k^{0.5}$, which is defined as:

$$Re_y = \frac{\rho \cdot y \cdot \sqrt{k}}{\mu}. \tag{3-50}$$

The switching criterion Re_y^* determines when the transition occurs from one layer to another. This turbulence model can work in high-Reynolds number mode, two-layer mode, and one-equation mode by varying the Re_y^* value from 0 to ∞. The value is usually selected in between 50 to 200 which ensure the transition occurs only in logarithmic region. The default value of the switching criterion in Star-CCM+ is given as Re_y^*=60. The constant c_A determines the sharpness of the transition from one model to another. The transition can be going from sharp to smooth by given the value from 1 to 10 (Jongen, 1998). In Star-CCM+, the constant c_A is defined as:

$$c_A = \frac{\left|\Delta Re_y\right|}{\tanh^{-1} 0.98}, \tag{3-51}$$

where ΔRe_y =10 is given as default value in Star-CCM+.

Several two-layer formulations have been proposed to compute the length scale functions: l_t and l_v. These two length scale functions consider the damping effects in the near-wall region. There are three models implemented in Star-CCM+ for selection which are named: Wolfshtein shear-driven model (Wolfshtein, 1969), Norris shear-driven model (Norris, 1975) and buoyancy-driven model (Xu et al., 1998).

The turbulence length scales of Wolfshtein shear driven model were developed based on the expression proposed by van-Driest (1956) for computing Prandtl's mixing length in the sublayer and buffer layer (Wolfshtein, 1969) (CD-adapco, 2012):

$$l_t = c_l y \left[1 - exp\left(-\frac{Re_y}{A_\varepsilon}\right)\right], \tag{3-52}$$

$$l_v = Re_y \cdot \frac{\mu}{\sqrt{\overline{vv}}} \cdot C_\mu^{\frac{1}{4}} \cdot \kappa^* \cdot \left[1 - exp\left(-\frac{Re_y}{A_\mu}\right)\right], \tag{3-53}$$

where the expressions in the brackets [ ] are van Driest damping factors which calculate the length scale in the sublayer (White, 2006). They are defined as $c_l=\kappa(C_\mu)^{-0.75}$, $A_\varepsilon=2c_l$, $A_\mu=70$, $C_\mu=0.09$ and $\kappa^*=0.42$.

The equations for the length scale in the Norris shear-driven model have some similarities with Eq. (3-53), only the damping constant A_μ was given with a different value. Therefore, the predictive results from Norris shear-driven model were found to be similar to the results from Wolfshtein shear driven model by the earlier researcher (Xu et al., 1998). This was also observed from the results in this study (see Section 4.7.2). The turbulence length scales of the buoyancy-driven model were obtained empirically by fitting the data of a turbulent natural convection in a differentially heated vertical slot at a Rayleigh number up to 10^5 (Versteegh and Nieuwstadt, 1996). The data were fitted fairly well by the equations of length scale developed:

$$l_t = \frac{8.8 \cdot y}{1 + 10/y_v^* + 5.15 \times 10^{-2} \cdot y_v^*}, \tag{3-54}$$

$$l_v = \frac{0.544 \cdot y}{1 + 5.025 \times 10^{-4} \cdot (y_v^*)^{1.65}}, \tag{3-55}$$

where

$$y_v^* = Re_y \cdot \sqrt{\frac{\overline{v'v'}}{k}}, \tag{3-56}$$

$$\frac{\overline{v'v'}}{k} = 7.19 \times 10^{-3} Re_y - 4.33 \times 10^{-5} \left(Re_y\right)^2 + 8.8 \times 10^{-8} \left(Re_y\right)^3. \tag{3-57}$$

This two-layer model was found to perform well in some natural convection flows cases such as natural convection along a heated vertical plate and natural convection flows in cavity (Xu et al., 1998).

3.2.4 Low Reynolds k-ε model

The low-Reynolds turbulence model is an alternative turbulence model to analyse viscous sublayer structure adjacent to a solid boundary and low-Reynolds number flow in stratification layers. The low-Reynolds turbulence model is developed based on standard k-ε model. The turbulent kinetic energy equation is identical to Eq. (3-18) from the standard k-ε model, but the dissipation rate equation and the eddy viscosity equation are modified to blend with damping functions which are expressed as follows:

$$\frac{\partial \varepsilon}{\partial t} + \bar{u}_j \frac{\partial \varepsilon}{\partial x_j} = \frac{\varepsilon}{k}[c_{\epsilon 1}(D_k + D_d + c_{\epsilon 3} D_b) - c_{\epsilon 2} f_2 \varepsilon] + \frac{\partial}{\partial x_j}\left((\nu + \nu_T/\sigma_\epsilon)\frac{\partial \varepsilon}{\partial x_j}\right). \quad (3\text{-}58)$$

The turbulent production D_k and buoyancy production D_b are defined identically to the corresponding terms in the standard k-ε model, the production term D_d and eddy viscosity equation are defined as follow in Star-CCM+:

$$D_d = f_2 \left(D_k + 2\mu \frac{k}{y^2}\right) e^{-c_E Re_y^2}, \quad (3\text{-}59)$$

where f_2 is a damping function defined as:

$$f_2 = 1 - c_A \cdot e^{R_t^2}, \quad (3\text{-}60)$$

where the default values for coefficients c_A and c_E are 0.3 and 0.00375 respectively, R_t is the turbulent Reynolds number defined as:

$$R_t = \frac{\rho k^2}{\mu \varepsilon}. \tag{3-61}$$

The equation of eddy viscosity is given as:

$$\mu_T = f_\mu \cdot c_\mu \cdot \rho \cdot k^2/\varepsilon\,, \tag{3-62}$$

where the damping function f_μ is given as:

$$f_\mu = 1 - e^{\left[-\left(C_{d0}\sqrt{Re_y} + C_{d1} Re_y + C_{d0} Re_y^2\right)\right]}\,, \tag{3-63}$$

where the default coefficients are C_{d0}=0.091, C_{d1}=0.0042, C_{d2}=0.00011.

3.2.5 $\mathbf{v^2}$-f Low-Reynolds number k-ε model

The $\overline{v^2}$-f turbulence model is known for its capability of capturing the near-wall turbulence effects more accurately by solving two additional differential equations: wall-normal stress function $\overline{v^2}$ and elliptic function f (Davidson et al., 2003) (Iaccarino, 2001). The turbulent kinetic energy equation is the same as Eq. (3-18) from standard k-ε turbulence model, the dissipation equation is modified and given in Star-CCM+ as follows:

$$\frac{\partial \varepsilon}{\partial t} + \bar{u}_j \frac{\partial \varepsilon}{\partial x_j} = \left[c_{\epsilon 1} \left(1 + c_a \sqrt{\frac{k}{\overline{v^2}}} \right) \frac{D_k}{T} - c_{\epsilon 2} \frac{\varepsilon^2}{k} \right] + \frac{\partial}{\partial x_j} \left((\nu + \nu_T/\sigma_\epsilon) \frac{\partial \varepsilon}{\partial x_j} \right), \tag{3-64}$$

where c_a =0.045 is a constant, T is the turbulent time scales which is defined as:

$$T = max\left[\frac{k}{\varepsilon}, c_t\sqrt{\frac{\mu}{\varepsilon}}\right], \tag{3-65}$$

where c_t =6 is a constant.

The effect of walls on turbulence is represented by wall-normal stress function $\overline{v^2}$; hence the $\overline{v^2}$-equation is given as follow in Star-CCM+. Note that the source term kf is dampened near walls as value of f has a boundary condition f =0 at walls (Davidson and Nielsen, 2003).

$$\frac{\partial \overline{v^2}}{\partial t} + \bar{u}_j \frac{\partial \overline{v^2}}{\partial x_j} = \frac{\partial}{\partial x_j}\left(\left(\nu + \nu_T/\sigma_{\overline{v^2}}\right)\frac{\partial \overline{v^2}}{\partial x_j}\right) + min\left\{kf, -\frac{1}{T}\left[(c_1 - 6)\overline{v^2} - \frac{2k}{3}(c_1 - 1)\right] + c_2 \cdot D_k\right\} - \frac{6\overline{v^2}\varepsilon}{k}, \tag{3-66}$$

where c_1 and c_2 are constants given as c_1=1.4, c_2=0.3. The f-equation is then given as:

$$L^2\frac{\partial^2 f}{\partial x_j \partial x_i} - f - \frac{1}{T}\left[(c_1 - 6)\frac{\overline{v^2}}{k} - \frac{2}{3}(c_1 - 1)\right] + c_2\frac{c_m\overline{v^2}S}{\varepsilon} = 0, \tag{3-67}$$

where c_m=0.22 is a constant, S is the strain rate tensors from Eq. (3-21), and L is the turbulence length scale which is defined as:

$$L = c_L max\left\{\frac{k^{3/2}}{\varepsilon}, c_e\left(\frac{\mu^3}{\varepsilon}\right)^{1/4}\right\}, \tag{3-68}$$

where c_L=0.23 , c_e=70 are constants. The eddy viscosity is defined as:

$$\mu_T = \rho \cdot T \cdot min\left(c_{ms}k, c_m\overline{v^2}\right), \tag{3-69}$$

where c_{ms}=0.09. It can be seen from Eq. (3-69) that damping effect is control by the value of $\overline{v^2}$ instead of Re_y in Eq. (3-62) and Eq. (3-63) of low-Reynolds turbulence model.

Table 3-3: The coefficients of v^2-f turbulence model.

$C_{\epsilon 1}$	$C_{\epsilon 2}$	σ_k	σ_ϵ
1.4	1.9	1.0	1.3

3.3 Heat transfer mechanisms

Heat is one of the energy forms which can be transferred from one system to another by the driving force of temperature differences between systems. The heat energy transfer from high temperature to low temperature region and will not stop until the temperature of the two regions are equalised. Generally, heat is transferred in three different ways: conduction, convection, and radiation. These mechanisms are different in heat transfer approaches, but it all requires the existence of temperature differences. These three mechanisms are presented below.

3.3.1 Heat conduction

Heat conduction occurs in substances such as solids, liquids and gases. The energy of heat is transferred from the high-energy particles to low-energy particles of the substance as a result of interactions between them. The interaction between particles can be different in different substances. For conduction in solid substances, the heat transfer is carried out by the vibration of molecules and the energy transport by free electrons. Heat conduction in liquid and gas is due to the collisions and diffusion of the molecules by their random motions. The energy is transferred from energetic molecules to less energetic ones causing a energy redistribution in the substance, and eventually reaches energy balance.

The effectiveness of heat conduction is affected by two factors: the thickness and the density of the medium. At a constant temperature difference, the thicker the medium, the less the heat is transferred and vice versa. The effectiveness of heat conduction is normally higher in condensed substances due to a shorter mean free path. The heat conductivity is higher in the medium with short mean free path. Therefore, the thermal conductivity of gas is lower than liquids as the molecules of liquids are more closely spaced than gases. Based on these facts, we can conclude that the amount of heat transfer via conduction is proportional to the temperature differences across the medium, but is inversely proportional to the thickness of the medium. That is,

$$Q_{cond} = -kA\frac{dT}{dx}, \tag{3-70}$$

where A is surface area of the medium, dT/dx is temperature gradient across the layer of the medium, k is thermal conductivity of the substance which measures the ability of the substance in conducting heat energy. This equation is known as Fourier's law of heat conduction. In the case of buoyancy-driven ventilation flow, the heat conduction at boundaries was not steady at the beginning but varies with time and position. The temperature and heat flux across the walls did not remain constant with time during the heat conduction process. Then the rate change of energy inside the control volume is the sum of heat conduction in each direction and the heat generation inside the control volume. That is,

$$\frac{\partial^2 T}{\partial x^2} + \frac{\partial^2 T}{\partial y^2} + \frac{\partial^2 T}{\partial z^2} + \frac{q_{gen}}{k} = \frac{1}{\alpha}\frac{dT}{dt}. \tag{3-71}$$

This equation is known as the Fourier-Biot equation where $\alpha = k/\rho c_p$ is the thermal diffusivity of the material, q_{gen} is the rate of heat generation inside the system and c_p is the specific heat.

3.3.2 Heat convection

Heat convection occurs at the solid and fluid interface. The flow motion of the fluid is the key feature for the definition of convection. The heat transfer is considered to be pure conduction when the fluid adjacent to the solid surface is at rest. The fluid motion increases the heat transfer rate by bringing the heat from the interface quickly into contact with surrounding fluid. Therefore, the rate of heat transfer through fluid is higher by convection than conduction. As mentioned above, the heat transfer process can only take place with a temperature gradient; therefore, the equation of heat convection can be expressed as:

$$Q_{\text{conv}} = hA\left(T_f - T_0\right), \tag{3-72}$$

where h is the convective heat transfer coefficient, A is the surface area where convection heat transfer takes place, T_f is temperature at the surface, T_0 is the temperature of the surrounding fluid away from the surface. This equation is also known as Newton's law of cooling.

3.3.3 Natural convection: buoyancy flow

Heat convection can be grouped into forced convection and natural convection. In forced convection, the fluid motion is driven by external forces such as a fan. Natural convection on the other hand is driven by natural means such as buoyancy effect.

Buoyancy effect is a phenomenon that the lighter fluid is being pushed upwards by a net vertical force in a gravitational field. When energy heat is transferred from a solid substance to adjacent fluid substance by convection, the fluid soon becomes warm and relatively light. This light fluid will experience weight loss as the result of reduced gravity; this is then known as the buoyancy force (see Figure 3-1).

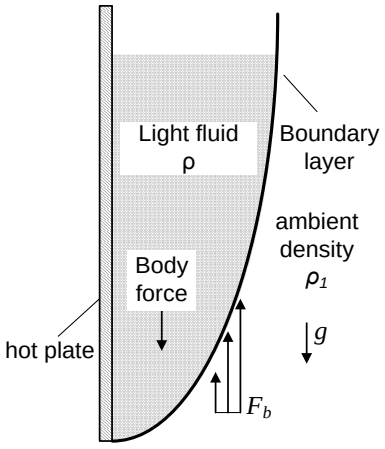

Figure 3-1: Buoyancy force.

Reduced gravity

When placing a heat source in a fluid flow field, a convection flow will be initiated soon as heat transfer takes place. As mentioned above, due to the buoyancy force, the lighter fluid begins to move upwards and the dense fluid descends to replace the vacant space. From this aspect, the lighter fluid is regarded as subjected to a reduced gravitational acceleration. Consider a fluid element of the plume immersed in the ambient flow field with its volume $\boldsymbol{V}$, the element is subjected to two forces: body force and buoyancy force. That is,

$$F_b = \rho_1 g \boldsymbol{V} \,, \tag{3-73}$$

where F_b is the buoyancy force, ρ_1 is the density of surrounding ambient fluid, $\boldsymbol{V}$ is the volume of the light fluid. If ρ is given to be the density of the light fluid, the total weight of the light fluid is the product of $\rho g \boldsymbol{V}$. Assuming the horizontal forces exerted on the element surface are neglected, the net vertical force exerts on the light fluid is

$$\Delta F = F_b - F_w = g\,\boldsymbol{V}(\rho_1 - \rho)\,. \tag{3-74}$$

where g is the gravitational acceleration as shown in Figure 3-2. Dividing both sides of the equation by the fluid mass, a new gravity force can be obtained. This term is then regarded as the reduced gravity g' which the plume fluid is subjected to (Prandtl, 1952).

$$g' = \frac{g(\rho_1 - \rho)}{\rho_1}\,. \tag{3-75}$$

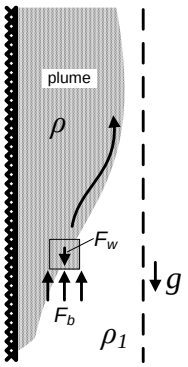

Figure 3-2: The plume fluid subject to reduced gravity.

The Boussinesq approximation

As discussed above, the buoyancy flow is subjected to reduced gravity as the result of temperature differences. In the modelling of buoyancy flow, the varying density variables in the vertical momentum equation make the problem even more complicated. Hence, an approximation is needed for the problem to reduce the complexity. The Boussinesq approximation simplifies the problem by neglecting the density variation in the inertial term and keeping the density variations in the gravitational term. That is,

$$\rho_0 \frac{Dw}{Dt} = -\frac{\partial p^*}{\partial z} - (\rho - \rho_0)g, \tag{3-76}$$

where ρ_0 is reference density, ρ is the fluid density, w is the velocity in vertical direction, p^* is the piezometric pressure $p^*=p+\rho gz$, g is gravity. This approximation is valid if the density differences compares to the reference density is small; i.e.,

$$\frac{\rho_0 - \rho}{\rho_0} \ll 1\,, \tag{3-77}$$

then the density in the inertial term of vertical momentum equation can be replaced with reference density ρ_0 without losing too much accuracy.

3.4 Surface to surface radiation heat transfer

Surfaces of an object can emit, absorb, and reflect radiation heat. The amount of radiation heat emitted depends on the radiative properties and the temperature of the surfaces. The analysis of radiation heat transfer from a surface and between surfaces is discussed in this section.

3.4.1 Thermal radiation

Surfaces of an object emit radiation with a temperature above zero. The radiation energy emitted by the surface area can be determined by Stefan-Boltzmann law. That is,

$$I_e = \varepsilon \cdot \sigma T_s^4 \,, \tag{3-78}$$

where T_s is the absolute temperature of the surface temperature in K, σ is the Stefan-Boltzmann constant that σ = 5.67x10^{-8} W/m^2 k^4, ε is the emissivity of the surface. A painted black surface in reality can be approximated to the surface of a black body which has emissivity ε=1.

Apart from emitting radiative energy, when radiation strikes an object, it absorbs and reflects the energy; some energy may be transmitted if the object is non-opaque. The sum of the energy absorbed, emitted, and transmitted should be equal to the total incoming energy; this gives the relation:

$$\alpha + \rho + \tau = 1 \,, \tag{3-79}$$

where α is absorptivity, τ is transmissivity, ρ is reflectivity. If the temperature of the object is equal to the temperature of the source that strikes radiative energy onto the surface, the Kirchhoff's law can be introduced to bring a relation for absorptivity and emissivity:

$$\alpha = \varepsilon \,. \tag{3-80}$$

3.4.2 Radiative heat transfer between surfaces

As discussed above, surfaces absorb and reflect radiation energy emitted from other surfaces. The net radiation heat gain/loss of a surface is the summation of the radiation leaving the surface and the radiation absorbed. That is,

$$E_r = A \cdot (J - I_r) \,, \tag{3-81}$$

where A is surface area, J is the radiosity represents the total radiation energy leaving a surface, I_r is the radiation strikes onto the surface from external radiation sources. If the surface is opaque and Kirchhoff's law is complied, the radiosity can be expressed as:

$$J = I_e + \rho I_r = \varepsilon I_b + (1 - \varepsilon) I_r \,, \tag{3-82}$$

where I_e and ρI_r are the radiation emitted (I_e = I_b when ε =1) and reflected by the surface as shown in Figure 3-3, I_b is the blackbody emissive power. Rearrange Eq. (3-82) and then substitute into Eq. (3-81) gives:

$$E_r = \frac{A \cdot \varepsilon}{1 - \varepsilon} (I_b - J) \,. \tag{3-83}$$

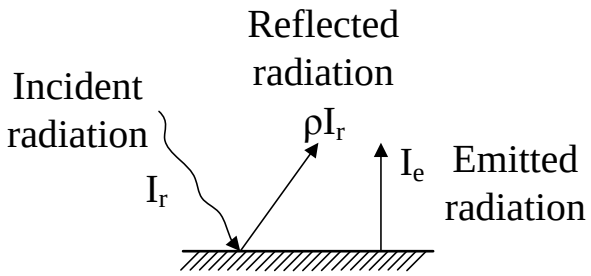

Figure 3-3: Incoming and leaving radiation on the surface.

When analysing it from the electrical analogy view, the surface resistance to radiation can now be defined as:

$$R_s = \frac{1-\varepsilon}{A \cdot \varepsilon}\,. \tag{3-84}$$

For radiation heat transfer between two surfaces, the radiation leaving surface *i* and strikes surface *j* is expressed as:

$$E_i = A_i \cdot J_i \cdot F_{i-j}\,, \tag{3-85}$$

where $F_{i\text{-}j}$ is the view factor represents the fraction of radiation leaving surface *i* that strikes surface *j*. For the radiation leaving surface *j* and strikes surface *i* is expressed as:

$$E_j = A_j \cdot J_j \cdot F_{j-i}\,. \tag{3-86}$$

Hence the net radiation heat transfer between the surfaces is:

$$E_{i-j} = A_i \cdot J_i \cdot F_{i-j} - A_j \cdot J_j \cdot F_{j-i}\,. \tag{3-87}$$

As $A_i\,F_{i\text{-}j} = A_j\,F_{j\text{-}i}$ according to reciprocity relation, Eq. (3-87) can be rearranged as:

$$E_{i-j} = A_i \cdot F_{i-j}\left(J_i - J_j\right). \tag{3-88}$$

This equation yields a space resistance to radiation, which is:

$$R_{i-j} = \frac{1}{A_i \cdot F_{i-j}}. \tag{3-89}$$

Hence, the total resistance to radiation between two surfaces can be obtained, and the radiation heat transfer between surfaces can be expressed as:

$$Q_{1-2} = \frac{I_{b1} - I_{b2}}{R_{s1} + R_{1-2} + R_{s2}} = \frac{\sigma(T_1^4 - T_2^4)}{\frac{1-\varepsilon_1}{A_1 \cdot \varepsilon_1} + \frac{1}{A_1 \cdot F_{1-2}} + \frac{1-\varepsilon_2}{A_2 \cdot \varepsilon_2}}. \tag{3-90}$$

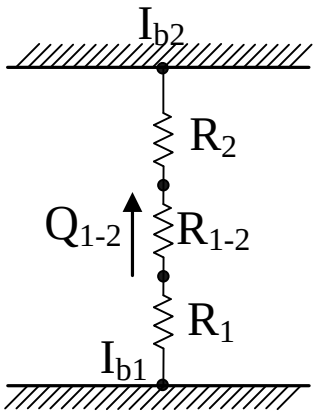

Figure 3-4: Total resistance to radiation between surfaces.

3.5 Radiation in participating media

The intensity of radiation can be attenuated by absorptivity and emissivity of participating media; it can also be attenuated by particles in the media such as dust, ice particles, and soot as a result of scattering. When radiation passes through gas layers as such, it starts to lose / gain its radiative energy by being absorbed or emitted. Air, for instance, is the main working fluid contains two main participating molecules: CO_2 and H_2O in this study. When the concentration of those two molecules become large, the radiative absorption and emission of the air should be considered. Hence, a radiative heat transfer equation is introduced in this section for considering the radiative properties.

3.5.1 Absorption

A participating medium in which the radiation travels through absorbs radiative energy as shown in Figure 3-5. The amount of the radiative intensity absorbed over the path length *dl* is equal to the product of original intensity and the absorption coefficient a_b. The change in intensity can be stated as:

$$di_s = -a_b \cdot i_s \, dl \, . \tag{3-91}$$

If absorption coefficient is assumed to be constant, then integrating Eq. (3-91) over the path length *dl* gives:

$$\ln \frac{i_s(l)}{i_s(0)} = -a_b l \, , \tag{3-92}$$

and hence it can be expressed as:

$$i_s(l) = i_s(0) \cdot e^{-a_b l}. \tag{3-93}$$

This equation shows that radiative intensity $i_s(0)$ is attenuated by the absorptivity of participating gas exponentially along the path it travels.

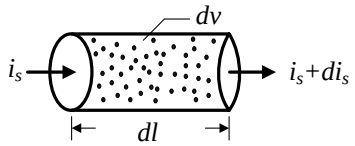

Figure 3-5: The change of intensity through participating gas over path length *dl.*

3.5.2 Emission

Not only does the participating medium absorb radiation, they also emits radiation energy. From Kirchoff's law, the absorptivity equals to the emissivity, $\alpha = \varepsilon$. That is,

$$\alpha = \varepsilon = 1 - e^{-a_b l}\,, \tag{3-94}$$

where ε is the emissivity of the medium. In the case of an optically thick medium, $a_b l >> 1$, then $\alpha = \varepsilon \approx 1$, the medium can be regarded as black surface. Hence,

$$Q_a = Q_e = (a_b \cdot i_b\, dl)\, dA\, d\Omega\,, \tag{3-95}$$

where Q_a is the energy absorbed by the medium,Q_e is the energy emitted by the medium, i_b is proven to be the blackbody intensity of the medium at its temperature (Modest, 1993). Hence, the amount of the radiative energy emitted by the medium is:

$$\frac{dQ_e}{dA\, d\Omega} = di_{s,e} = a_b \cdot i_b\, dl\,, \tag{3-96}$$

where $di_{s,e}$ is the emitted radiative intensity.

3.5.3 Scattering

Out-scattering

When radiation passes through the medium contains particles such as dust, ice particles, and soot, these particles deflect the incoming radiation causing a reduction in its radiative intensity (see Figure 3-6). The scattered radiation is redirected into another direction with an angle θ away from the direction *dl*. Then the attenuated intensity (i_s-$di_{s,s}$) keeps travelling on the same direction. The cross-sectional area dA_s is the projected area of differential volume *dv* normal to the direction of scattered intensity $di_{s,s}$.This projected area dA_s is defined as the area that encounters all scattering particles. The ratio of the projected area dA_s to *dA* is shown to be equal to the ratio of scattered intensity $di_{s,s}$ to incoming intensity i_s (Siegel, 1992). That is,

$$\frac{di_{s,s}}{i_s} = \frac{dA_s}{dA}. \tag{3-97}$$

Let each particle has a scattering cross section $\bar{m}$, and there are $\bar{n}$ numbers of particles per unit volume within the projected area, then

$$dA_s = dv \cdot \sum_{n=0}^{\infty} \bar{n} \cdot \bar{m}, \tag{3-98}$$

where $\sum_{n=0}^{\infty} \bar{n} \cdot \bar{m}$ represents the effective scattering area per unit volume is then defined as scattering coefficient a_s:

$$dA_s = a_s \cdot dv. \tag{3-99}$$

Let *dv=dA dl*, together with Eq (3-97) the change of intensity by scattering can be express as:

$$\frac{di_{s,s}}{i_s} = \frac{a_s\, dA\, dl}{dA} = a_s\, dl = -\frac{di_s}{i_s}. \tag{3-100}$$

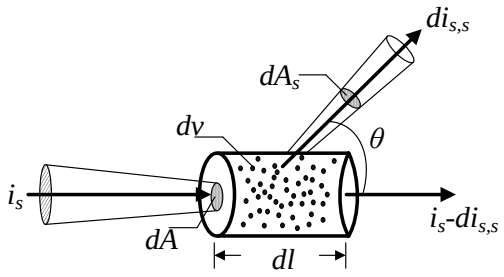

Figure 3-6: Schematic of incident intensity scattered by particles.

In-scattering

When radiation penetrates through the medium contains particles, some radiation is scattered away and some radiation from other directions is scattered into the path in $\hat{I}$ direction as shown in Figure 3-7. This is called the incoming scattering. As radiation $i_{\eta 0}$ penetrates through medium in $\hat{J}$ direction, a portion of radiative intensity $di_{\eta 0}$ is scattered away. Among all the scattered radiation, a fraction of it is scattered into the direction $\hat{I}$ which can be expressed as:

$$di_{\eta 0}(\theta, \omega) = di_{\eta 0} \cdot \frac{\varphi(\theta, \omega)}{4\pi}, \tag{3-101}$$

where $\varphi(\theta, \omega)$ is defined as scattering phase function which describes the angular distribution of the scattered radiation. The radiation scattered into the direction of i_η is $di_{\eta 0}(\theta, \omega)$, where ω is the circumferential angle as shown in Figure 3-8.

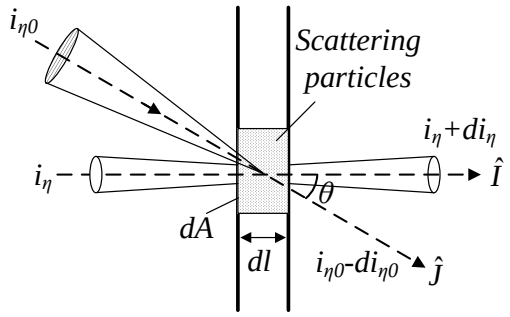

Figure 3-7: Schematic of incoming scattering intensity.

Of all the scattered radiative intensity, $di_{s,s}$, the portion being scattered into (θ,ω) direction is defined as $di_{s,s}(\theta,\omega)$ which is shown in Figure 3-8. Therefore, the total amount of scattered intensity can be expressed as:

$$di_{s,s} = \int_{\Omega_s=0}^{4\pi} di_{s,s}(\theta,\omega)\, d\Omega_s \,. \tag{3-102}$$

The intensity of $di_{s,s}$ scattered into direction (θ,ω) is expressed as:

$$di_{s,s}(\theta,\omega) = di_{s,s} \cdot \frac{\varphi(\theta,\omega)}{4\pi} = a_s \cdot i_s\, dl \cdot \frac{\varphi(\theta,\omega)}{4\pi} \,. \tag{3-103}$$

Substituted Eq. (3-102) into Eq. (3-103) gives the phase function:

$$\varphi(\theta,\omega) = \frac{di_{s,s}(\theta,\omega)}{\frac{1}{4\pi}\int_{\Omega_s=0}^{4\pi} di_{s,s}(\theta,\omega)\, d\Omega_s} \,. \tag{3-104}$$

It can be seen that the phase function is the ratio of the scattered intensity in the direction (θ,ω) to the intensity equally scattered in that direction. If the ratio equal to 1, i.e., $\varphi(\theta,\omega)=1$; then the scattering is called isotropic.

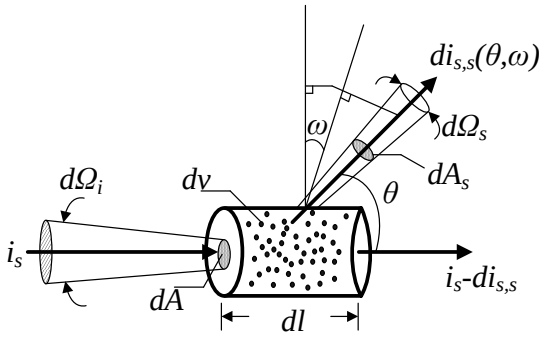

Figure 3-8: Schematic of intensity scattered away into direction (θ,ω).

Base on the previously made theory, the amount of intensity scattered in can be now calculated. Consider Figure 3-9, the amount of energy flux scattered away from $i_{\eta 0}$, per unit incident solid angle $d\Omega$, and per unit area normal to incident direction ($dA\cos\theta$) as:

$$d^4Q = di_{\eta 0}(\theta,\omega)\cdot d\Omega\cdot d\Omega_\eta\cdot dA\cos\theta. \tag{3-105}$$

Using Eq. (3-100) and Eq. (3-101) then the portion scattered into intensity i_η is:

$$di_{\eta 0}(\theta,\omega) = \left(a_s\cdot i_{\eta 0}\cdot\frac{dl}{\cos\theta}\right)\cdot\frac{\varphi(\theta,\omega)}{4\pi}, \tag{3-106}$$

then the total energy flux coming into direction $\hat{I}$ can be calculated by integrating:

$$di_\eta = \int_0^{4\pi}\left(a_s\cdot i_{\eta 0}\cdot dl\right)\cdot\frac{\varphi(\theta,\omega)}{4\pi}\cdot d\Omega\,. \tag{3-107}$$

Therefore, the amount of intensity attenuated by incoming scattering is:

$$\frac{di_\eta}{dl} = \frac{a_s}{4\pi}\int_0^{4\pi} i_{\eta 0} \cdot \varphi(\theta, \omega) \cdot d\Omega \,. \tag{3-108}$$

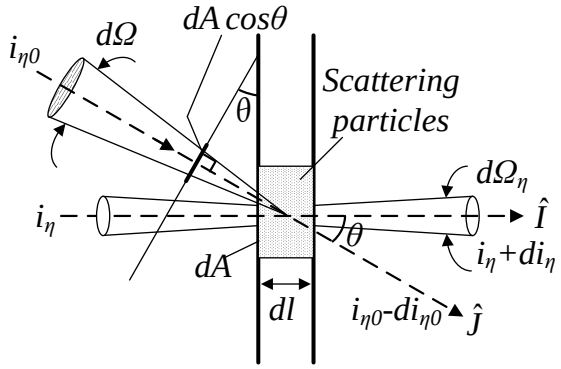

Figure 3-9: Schematic for the analysis of the amount in-scattering energy.

3.5.4 Radiative transfer equation

The radiative transfer equation describes all the radiative energy attenuation within the participating medium when radiation passing through. As discussed above, radiative intensity within the participating medium can be attenuated by medium due to its radiative absorptivity, emissivity and scattering. Hence, the total attenuation of radiative energy is the sum of Eq. (3-91), Eq. (3-96), Eq. (3-100), and Eq. (3-108). The total changes in intensity along the path long *dl* in solid angle $d\Omega$ can be express as:

$$\frac{di_s}{dl} = -a_b \cdot i_s + a_b \cdot i_b - a_s \cdot i_s + \frac{a_s}{4\pi}\int_{4\pi} i_{\eta 0} \cdot \varphi(\theta, \omega) d\Omega \,. \tag{3-109}$$

Combining the absorption and scattering terms which forms the equation of transfer given as:

$$\frac{di_s}{dl} = -a_{ex} \cdot i_s + a_b \cdot i_b + \frac{a_s}{4\pi}\int_{4\pi} i_{\eta 0} \cdot \varphi(\theta, \omega) d\Omega \,, \tag{3-110}$$

where a_{ex} is the extinction coefficient which is the combination of the absorption coefficient and scattering coefficient. As the effect of scattering to radiation heat transfer under normal circumstance is very small and therefore negligible. The scattering coefficient is given as zero in this study.

3.5.5 Absorption coefficient

Absorption coefficient indicates the magnitude of radiative intensity of the radiation attenuated when travelling through participating medium. The absorptivity of a non-grey gas is found to vary rapidly across the spectrum showing band nature of absorption. Numbers of band models such as narrow band model and wide band model were used for calculation.

As absorptivity varies rapidly across the spectrum, the narrow band model focuses on individual line shapes, widths, and spacing over a given range of wavenumbers to derive band characteristics. For a straightforward spectral integration, the narrow band model replaces the actual coefficient values with averaged ones over a given narrow range wavenumber. However, this model is not suitable for nonhomogeneous gases. The wide band model, on the other hand, obtains absorption or emission by integrating the results of narrow band model across the entire spectrum which are less accurate results and cannot be used for nonhomogeneous gases either.

Another absorption coefficient is defined for the convenience of calculating total radiative intensity called the Planck mean absorption coefficient. This coefficient is derived from the averaged values of wide band model over the entire spectrum making the assumption that the Planck function varies little across each spectral line (Tien, 1968). The Planck mean absorption coefficients for various single homogeneous absorbing gases have been calculated later based on high-resolution databases such as HITRAN96 and HITEMP and presented by Zhang and Modest (2002).

However, in practical applications, gas mixture such as air contains more than one absorbing gas species; the total absorptance of this gas mixture could form its own absorbing characteristics. This is due to the overlap of spectral lines of non-grey gases at certain spectrum regions. In this study, the participating medium, air, contains two strong absorptivity gases: CO_2 and H_2O. These two gases overlap in spectrum region (2.7 and 15 μm) and hence a correction should be made to calculate the absorptivity of the gas mixture. However, the calculation of absorptivity of non-grey gas mixture can be tedious. This is because the absorptivity and emissivity are

strongly related with wavelength and this would require an integration of absorption coefficient line with respect to the wavelength to determine its value.

Hence, this study assumes the gases to be grey and uses the emissivity charts presented by Hottel (1967) to replace the heavily spectral-dependent calculation method. The results have shown to have a satisfactory agreement with the emissivity values calculated based on HITEMP-2010 spectral data base conducted by Alberti et al. (2015), (Alberti et al., 2016). Hence, this simple model is applied in this study. The absorptivity, α, of isothermal and homogeneous CO_2 and H_2O gas mixtures is given as:

$$\alpha = \alpha_c + \alpha_w - \Delta\alpha_{cw}\,, \tag{3-111}$$

where α is the absorptivity of the gases mixture CO_2 and H_2O, α_c and α_w are the absorptivity of CO_2 and H_2O respectively and $\Delta\alpha_{cw}$ is the overlap correction.

$$\alpha_c = c_c \left(\frac{T_g}{T_s}\right)^{0.65} \times \varepsilon_c \left(T_s, \frac{P_c L T_s}{T_g}\right), \tag{3-112}$$

$$\alpha_w = c_w \left(\frac{T_g}{T_s}\right)^{0.45} \times \varepsilon_w \left(T_s, \frac{P_w L T_s}{T_g}\right), \tag{3-113}$$

where T_s is the heat source temperature, T_g is the gas temperature, L is the mean distant travelled by radiation. The partial pressures of CO_2 and H_2O are p_c and p_w. The value of (c_c, ε_c) and (c_w ε_w) are determined from the charts as shown in Figure 3-10 and Figure 3-11.

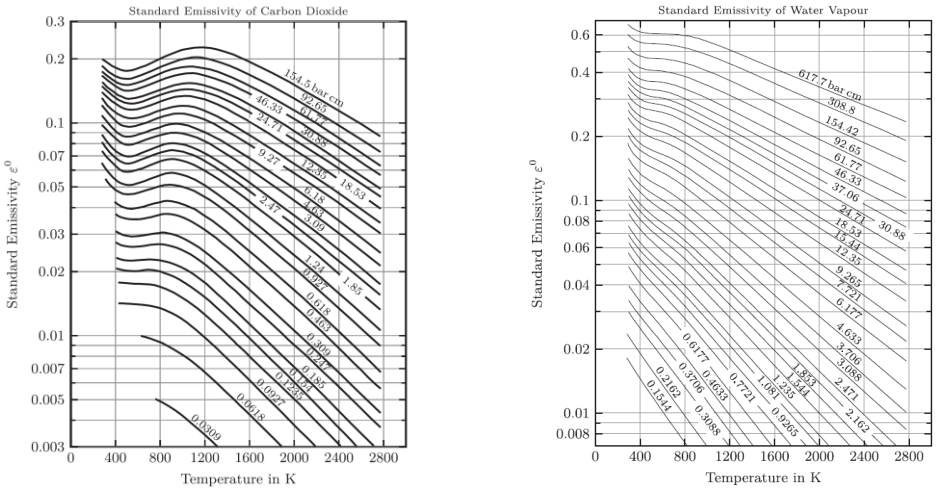

(a) (b)

Figure 3-10: Hottel's emissivity charts for (a) carbon dioxide, (b) water vapour (Alberti et al., 2015)

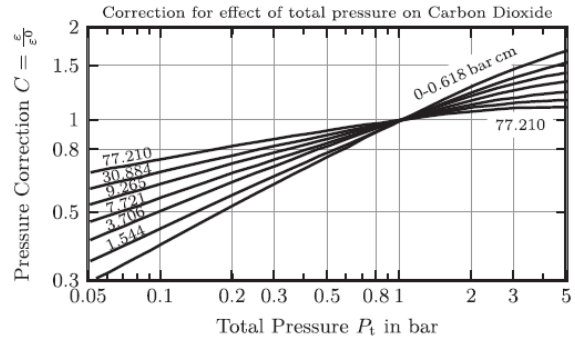

(a)

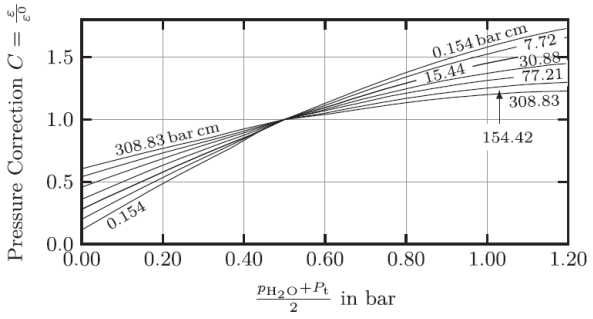

(b)

Figure 3-11: Hottel's pressure correction charts for (a) carbon dioxide, (b) water vapour (Alberti et al., 2015)

From Eq. (3-93), the absorptivity is defined as:

$$\alpha = \frac{i_s(0) - i_s(l)}{i_s(0)} = 1 - e^{-\int_0^l a_b dl} . \tag{3-114}$$

Assuming the absorption coefficient is constant along the pathlength *l*, the relation between absorptivity and absorption coefficient can be state as:

$$\alpha = 1 - e^{-a_b l} . \tag{3-115}$$

The pathlength l in this study will be generally approximated by the mean beam length which is calculated from the dimension of the simulation domain (Lallemant et al., 1996). The definition of mean beam length is described as follow.

Mean beam length

The incident energy radiated from a volume of isothermal gas body to all or parts of its boundaries is correlated with the path length it travels. In the geometry of a hemisphere, the energy radiates from a hemispherical gas body of a surface dA_j to the centre of its base of the area dA_b is dependent on the radius of the hemisphere ($a_b \cdot R$) of gas (Tien, 1968) as shown in Figure 3-12 and the equation below:

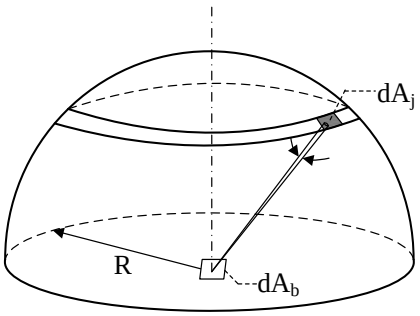

Figure 3-12: Schematic of hemisphere of gas.

$$\mathrm{dQ}_\lambda = (1 - e^{-a_b \cdot R}) E_\lambda d\lambda\,, \tag{3-116}$$

where dQ_λ is the incident energy flux, R is the radius of the gas hemisphere, E_λ is the blackbody spectral emission. For simplicity, this simple relation is used for determining the value of energy flux for any geometry of radiating gas volume. Thus the radius can be replaced by a fictitious length l_{b0} to compute the incident energy radiated from an arbitrary gas-body shape. This length is then called mean beam length (Siegel, 1992). However, the equation for computing the mean beam length can be difficult to solve, especially with arbitrary gas-body shape. Hence, a simple relationship is required.

The determination of mean beam length for the geometry can be difficult because the involvement of integration in the calculation. In the case of an optically thin medium, a practical approximate relation can be obtained due to a small value of $a_b \cdot l \ll 1$. The mean bean length for optically thin medium is approximated as:

$$l_{b0} = \frac{4\boldsymbol{V}}{A}\,, \tag{3-117}$$

where $\boldsymbol{V}$ is the volume of the gas, and A is the entire area of the boundary surface bounding the gas body $\boldsymbol{V}$ as shown in Figure 3-13. When medium such as air contains very few H_2O and CO_2 gas molecules and the distance between surfaces which radiation travels is short, the medium is considered as optically thin.

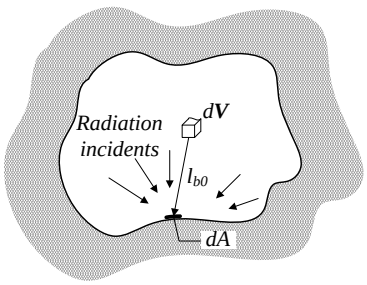

Figure 3-13: Schematic of arbitrary gas volume $d\boldsymbol{V}$ radiating to surface element dA.

The participating medium is considered optically thick when the pathlength is long and the space contains high level production of H_2O and CO_2 gases molecules. For optically thick medium, the mean beam length can be calculated by introducing a correction factor to the approximated relation from above (Modest, 2003). That is,

$$l_{b0} = c_b \frac{4\boldsymbol{V}}{A}, \tag{3-118}$$

where c_b is the coefficient determined base on the geometric configuration of the enclosure.

3.6 Thermal energy analysis

The thermal heat transfer within the ventilated enclosure in this study includes heat conduction, convection and radiation. The analysis of thermal heat transfer between and at boundaries comply the principle of conservation of energy. For thermal energy transfer at inner surface of sidewalls, the amount of heat loss through sidewalls by conduction is equal to the sum of heat coming into inner surface via convection and radiation as shown in Figure 3-14. The energy equation can be expressed as:

$$kA\frac{(T_i - T_o)}{L} = h_i A(T_a - T_i) + \sum_j^5 AF_j \varepsilon\sigma\left({T_{s,j}}^4 - {T_i}^4\right), \qquad (3\text{-}119)$$

where T_i is inner wall surface temperature, T_o is outer wall surface temperature, T_a is the temperature of the air flow next to the surface, k is the conductivity of the wall, A is the surface area, h_i is the convection coefficient, F is the view factor, σ is Stefan-Boltzmann constant, ε is the emissivity, T_s is surface temperature of other walls.

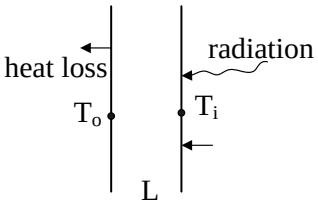

Figure 3-14: Heat transfer at wall surface.

The heat transfer at ceiling surface can be different from other walls. As hot buoyant current accumulates at the ceiling surface, the temperature at ceiling surface is the highest of all. Hence, ceiling surface radiates thermal energy to all other wall surfaces, as shown in Figure 3-15. The energy balance is then expressed as:

$$h_{ci}A(T_a - T_{ci}) = kA\frac{(T_{ci} - T_{co})}{L_c} + \sum_j^5 AF_j \varepsilon\sigma\left({T_{ci}}^4 - {T_{s,j}}^4\right). \qquad (3\text{-}120)$$

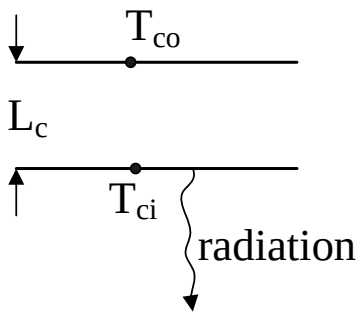

Figure 3-15: Heat transfer at ceiling surface.

The thermal energy of the room air is calculated as the product of the averaged outlet and inlet temperature of air flow and the volume flow rate. That is,

$$E_{adv} = \rho \dot{V} c_p (T_{out} - T_{in}) \,, \tag{3-121}$$

where T_{out} is the averaged outlet airflow temperature, T_{in} is the averaged inlet airflow temperature, ρ is the density of air flow, $\dot{V}$ is volume flow rate, c_p is the specific heat. By thermal energy conservation principle, the total thermal energy input from the heat source is equal to the sum of the thermal energy leaving the space via advection, and the energy heat lost through the walls.

3.7 Summary

This chapter details the knowledge of turbulence models, theory of buoyancy plume flows, radiative heat transfer within participating medium, and the mathematical model for computing absorption coefficients. The modelling and analysing works for studying buoyancy-driven displacement ventilation flows in the next chapter utilise these methods presented above.

CHAPTER FOUR

4 Modelling Methodology

4.1 Context

Previous chapters review the early studies of buoyancy-driven flow and related underlying theories. This chapter is to determine the turbulence model and the absorption coefficient that best predicts the flow configuration of each case considered. To achieve this, this chapter conducts modelling accuracy control by analysing the performances of turbulence models and mesh cell independence tests. The absorption coefficient on the date of the experiment conducted was determined based on the condition of the humidity in the air.

This chapter details the dimensions of four computational domains considered, the boundary conditions, the construction of grid cells, and the determination of absorption coefficients based on the humidity condition of each case. This chapter also carried out mesh independent test and analysed the performance of turbulence models for modelling buoyancy-driven displacement ventilation flows. At the end of this chapter, the methodology used for modelling buoyancy-driven type of ventilation flows is determined and a flow chart detailing the modelling procedure is presented.

4.2 The geometries of ventilation flow models

The computational domains created in this study were based on the layout of the experiments designed by Sandbach and Lane-Serff (2011b). The domain created based on the size of the test room was used to model unventilated filling box model. The domains created for modelling buoyancy-driven displacement ventilation flow were identical to the experiment set-ups. The dimensions of those geometries are described as follow:

4.2.1 Unventilated filling box model

The dimension of the filling box model is a room measuring 3 m high by 7 m wide by 5.6 m deep. A heat source located in the middle of the room with diameter 1 m. A temperature line probe is placed in between the wall and heat source as shown in Table 4-1.

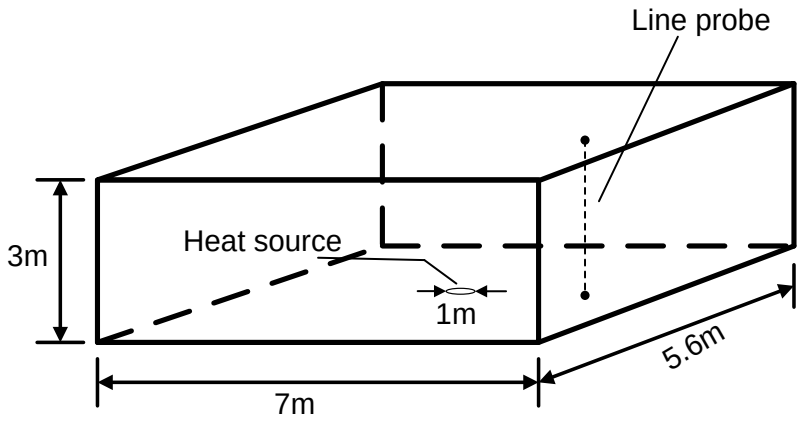

Figure 4-1: Geometry of unventilated filling box model (Sandbach and Lane-Serff, 2011b).

The walls of the domain are adiabatic, initial temperature of the fluid in the region is 300K, the Boussinesq approximation is employed with thermal expansion coefficient 0.0033/K, the density of the fluid is assumed to have constant value of 1.18 kg/m^3. The heat source rated is 0.785 kW.

4.2.2 Displacement ventilation flow model

For the case of displacement ventilation flow, the geometry created consists of a test room with four openings and a chamber. The openings are mounted two each on the ceiling and on the front wall near floor level of the test room. The test room is then located inside the chamber as shown in Figure 4-2. The test room is 2.78 m high by 7.46 m wide by 5.6 m deep. The size of the chamber is 7.5 times larger in volume. There is also a temperature line probe placed in between the sidewall and heat source for measuring the temperature profile of the room.

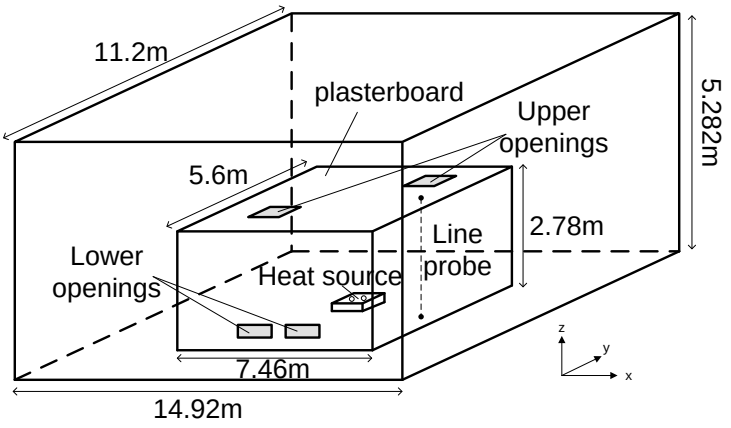

Figure 4-2: Geometry of displacement ventilation flow model (Sandbach and Lane-Serff, 2011b).

The two openings on the ceiling and the front wall are named UO-1, UO-2, LO-1, and LO-2 respectively as shown in Figure 4-3. The two upper openings, UO-1 and UO-2, were made same size on the ceiling each measuring 1.178 m by 0.576 m. The other two lower openings made on the front wall from left to right are LO-1 and LO-2. The dimension of the LO-1 opening is 1.075 m in width and 0.27 m in height; the LO-2 opening is 1.08 m in width and 0.315 m in height. The area of the dimensions of the openings are summarised in the Table 4-1.

The sidewalls of the test room were constructed of two 15 mm thick plasterboards separated by a 54 mm air gap in between. The ceiling was constructed from a single panel of plasterboard and insulated by a 12 mm thick fibreboard. The floor is made of 25 mm thick chipboard covering metallic surfaces on both sides and a carpet is laid on top of the metallic surface on the upper surface. A heat source is placed in the centre of the test room on the floor with an area of 0.1395 m^2 as shown in Figure 4-4.

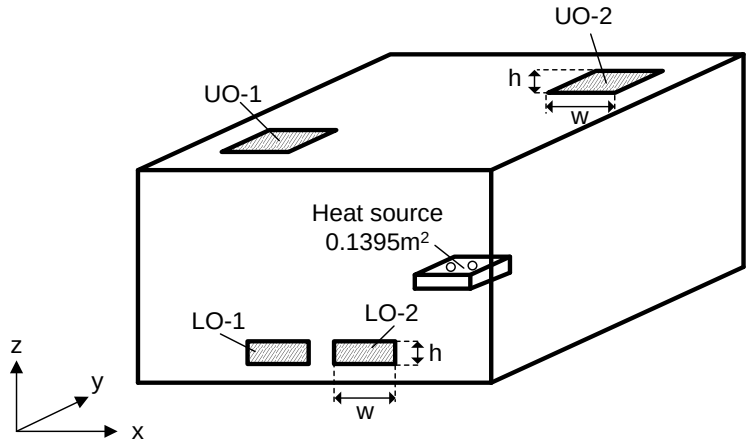

Figure 4-3: Three-dimensional representation of the test room.

Table 4-1: Dimensions of the upper and lower openings of the test room.

Openings	Width (w) (m)	Height (h) (m)	Area (m^2)
UO-1	1.178	0.576	0.6785
UO-2	1.178	0.576	0.6785
LO-1	1.075	0.27	0.2903
LO-2	1.08	0.315	0.34

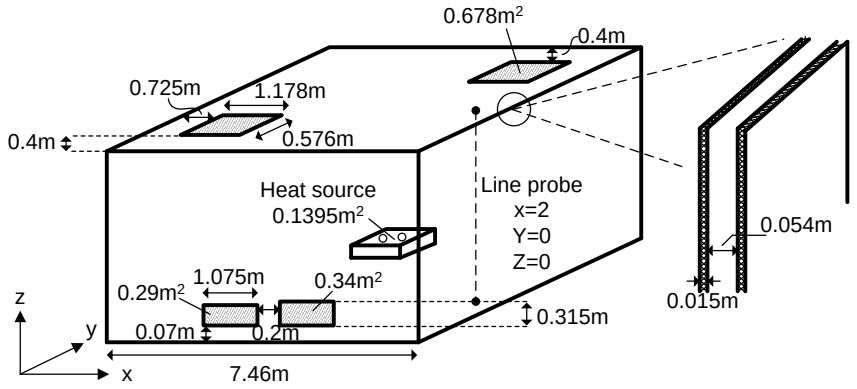

Figure 4-4: Schematic of dimensions of the test room of model Hf64 (Sandbach and Lane-Serff, 2011b).

Given four sets of opening sizes and two heat source rates, there are eight models in total created in this study. The effective areas of the openings were gradually reduced by closing off the openings from one model to the other. The total areas of upper and lower openings of the first model, Hf64, are 1.356 m^2 and 0.63 m^2 respectively (see Figure 4-4). This model was used to simulate the model with effective opening area of a*= 0.065 in Sandbach's study. In the second geometry Hf50, the total area of upper openings is reduced to 0.678 m^2 by closing off one of the upper openings, UO-2. The area of the lower openings, on the other hand, remains 0.63 m^2 (see Figure 4-5). This configuration is used to simulate the model with effective opening area of a*= 0.052.

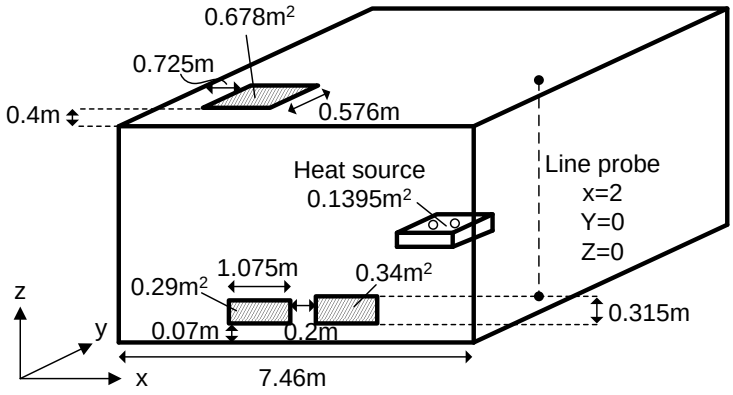

Figure 4-5: Schematic of dimensions of the test room of model Hf50 (Sandbach and Lane-Serff, 2011b).

In the third geometry, UO-1 remains open to give a total upper opening area of 0.678 m^2; lower opening LO-2, was closed off and LO-1 opening remains opened as shown in Figure 4-6. This configuration is used to simulate the model with an effective opening area a*= 0.03.

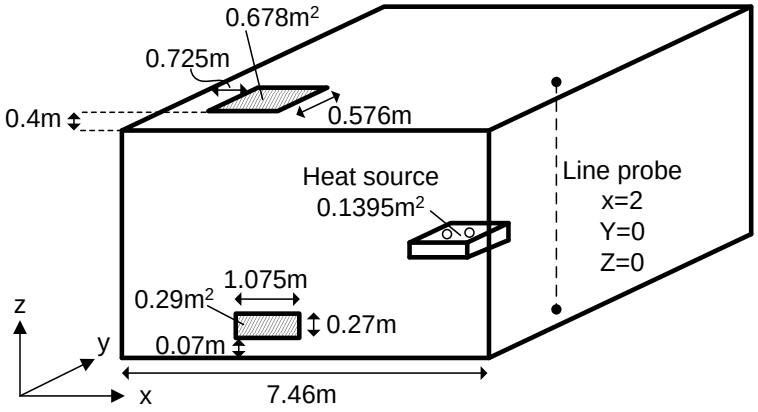

Figure 4-6: Schematic of dimensions of the test room of model Hf30 (Sandbach and Lane-Serff, 2011b).

In the last geometry, the area of upper opening is further reduced to 0.218 m^2 by reducing its width down to 0.378 m. The lower opening, LO-1, remains unchanged (see Figure 4-7). This configuration is used to simulate the model with an effective opening area of a*= 0.19. A summary of all eight models created with different size of openings are presented in Table 4-2 and Table 4-3.

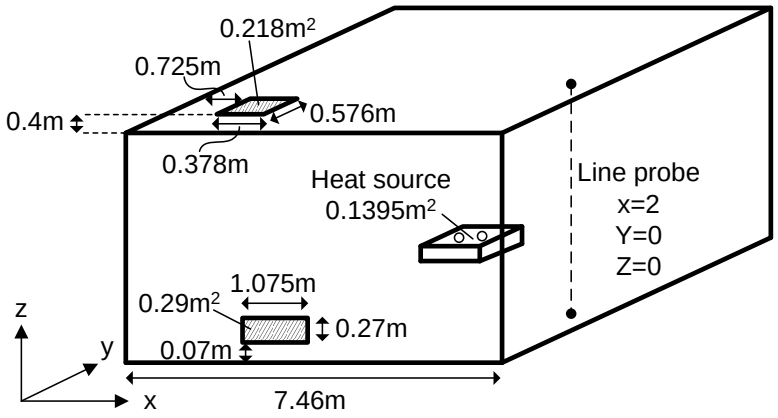

Figure 4-7: Schematic of dimensions of the test room of model Hf19 (Sandbach and Lane-Serff, 2011b).

Table 4-2: A summary of the sizes of the openings with 2.4 kW heat rate

Models	Upper opening (m^2)	Lower opening (m^2)	Heat source (kW)	Counterpart models
Hf64	1.36	0.63	2.4	a*=0.065
Hf50	0.678	0.63	2.4	a*=0.052
Hf30	0.678	0.29	2.4	a*=0.030
Hf19	0.218	0.29	2.4	a*=0.019

a* represents the effective opening area (Sandbach and Lane-Serff, 2011b)

Table 4-3: A summary of the sizes of the openings with 1.25 kW heat rate.

Models	Upper opening (m^2)	Lower opening (m^2)	Heat source (kW)	Counterpart models
hhf64	1.36	0.63	1.25	a*=0.065
hhf50	0.678	0.63	1.25	a*=0.052
hhf30	0.678	0.29	1.25	a*=0.030
hhf19	0.218	0.29	1.25	a*=0.019

a* represents the effective opening area (Sandbach and Lane-Serff, 2011b)

The material properties of the ceiling, floor, sidewalls, and working fluid (air) were obtained from Sandbach and Lane-Serff (2011b), and were used for modelling in this study. The temperature of the air was determined based on the measurements taken by Sandbach (2009). The initial air temperatures outside the test room are different from each date of the experiment conducted, it ranges from 286 K to 293 K as shown in Table 4-5. As the thermal properties of the air do not vary significantly within 5 K (less than 1%), 290 K (an averaged value of highest and lowest temperature) was set as the initial temperature for each case for convenience. The thermal properties of the initial air together with the properties of ceiling, walls and floor materials are summarised in Table 4-4.

Table 4-4: A list of properties of ceiling, floor, and sidewalls*.

	ρ (kg m^{-3})	Cp (kJ kg^{-1} K^{-1})	k (W m^{-1} K^{-1})
Ceiling	800	1000	0.17
Walls	800	1000	0.17
Floor	1000	1300	0.17
Air (T=290 K)	1.2172	1006	0.0254

*properties of materials obtained from Sandbach and Lane-Serff (2011b)

Table 4-5: Ambient air temperatures on each experiment-conducted date.

Date of Exp conducted*	Air Temp. outside test room (K)
3rd-Jan	286
4th-Jan	287
5th-Jan	286
6th-Jan	286
30th-Jan	287
31st-Jan	287
2nd-Feb	287
6th-Feb	287
8th-Feb	287
9th-Feb	288
13th-Feb	287
15th-Feb	288
7th-March	286
9th-March	288
16th-March	287
15th-May	293
16th-May	293
22th-May	291

* Experiments conducted in 2006 by Sandbach and Lane-Serff (2011b)

4.3 Mesh generation

The mesh method is important to simulation works as it has a great influence on the convergence and accuracy. In order to determine which type of mesh grid is better for modelling, two types of mesh grid: the hexahedral mesh and the unstructured polyhedral mesh were constructed for examination. In the following sections, the characteristics and the advantages/disadvantages of utilizing each type of mesh grid are presented and analysed. The reasons for choosing unstructured polyhedral mesh for modelling are given.

4.3.1 Mesh types

Based on the geometry of the computational domain shown in the previous sections, here in Figure 4-8 and Figure 4-9 presents the cartesian hexahedral mesh and the unstructured polyhedral mesh generated in the domain of test-room at its vertical (x-z) cross-section at y=0 view. A total of 1,872,349 grid cells were generated using hexahedral mesh type; and a total of 1,261,660 grid cells were generated using polyhedral mesh.

Grid refinement was applied at the turbulent flow dominated regions, which can have a great influence on the solutions. One of the main advantages of using the unstructured grids is that it can handle grid refinement in a more effective and seamless manner than structured meshes. In addition, an unstructured mesh is easy to generate and has higher flexibility in dealing with complex geometries. It can be seen from Figure 4-9 that the upper and lower parts of the test room region was refined with small grid sizes respectively in order to obtain accurate predictions at the near wall regions.

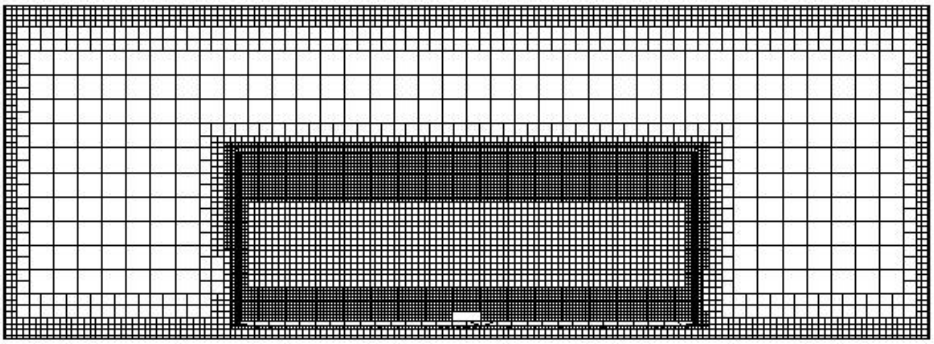

Figure 4-8: Hexahedral mesh.

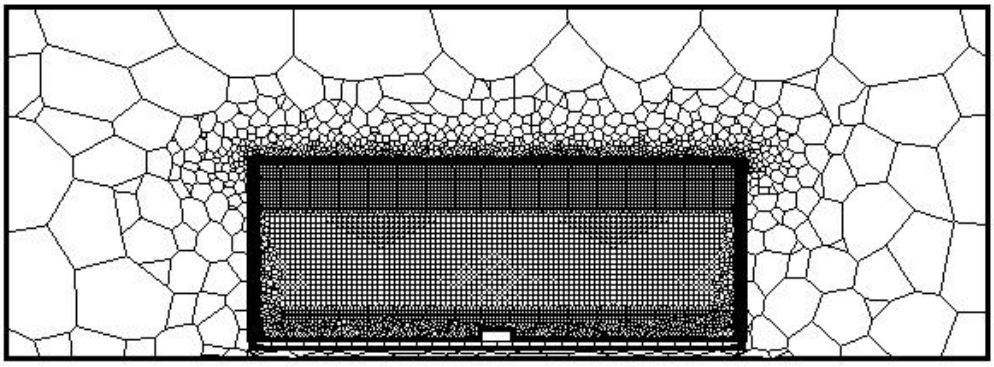

Figure 4-9: Polyhedral mesh.

4.3.2 Performance comparison and conclusions

The simulation results of case Hf64 (listed in Table 4-2) using hexahedral mesh and polyhedral mesh respectively were compared for analysis. The two time-dependent cases run for real-time 3 minutes, and the vertical temperature profiles from both cases were compared with the measurements. The results are shown in the following figures.

It can be seen from the Figure 4-10 that the polyhedral meshed model produced the lowest absolute residual value than hexahedral meshed model. In addition, the polyhedral mesh type used less numbers of iteration to reach the level of convergence. The velocities at the lower opening LO-2 of both cases were monitored throughout the iterations as shown in Figure 4-11. It can be seen that the solutions from the hexahedral mesh type converged on the same result from polyhedral mesh type.

The vertical temperature profiles from both cases and the experimental measurements are presented in Figure 4-12. The result shows that the vertical temperature profiles of the two cases match reasonably well with the experimental data.

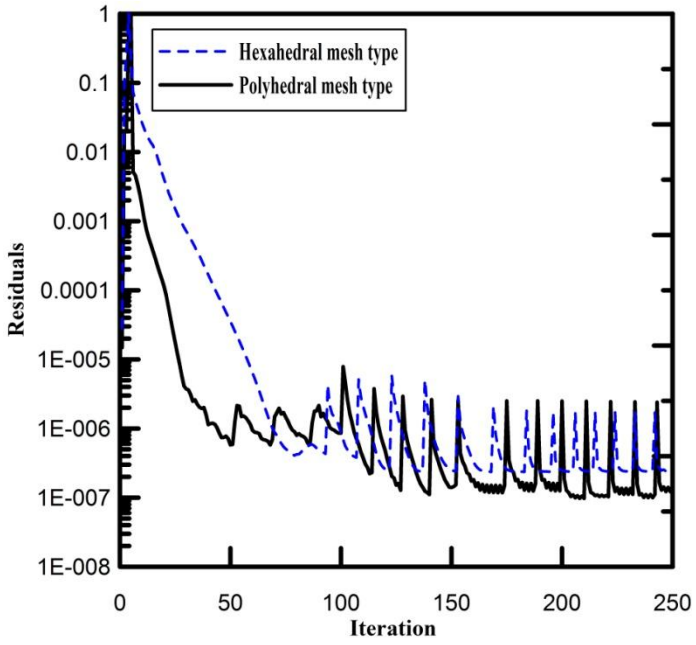

Figure 4-10: The energy residuals from hexahedral and polyhedral meshed cases.

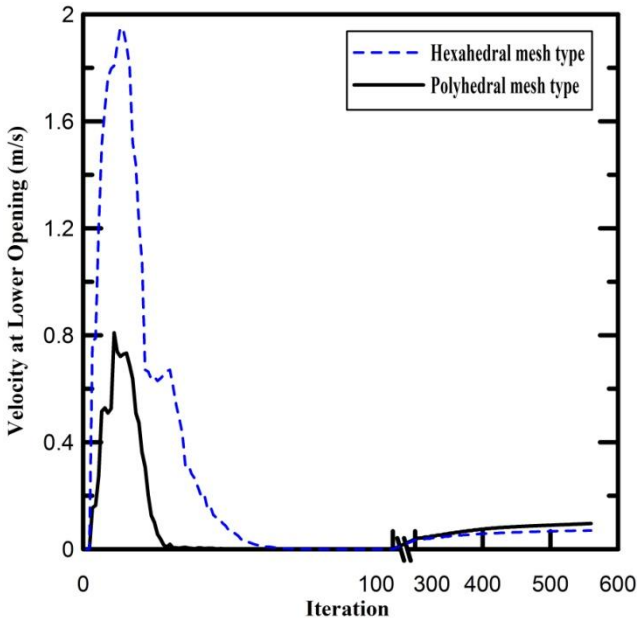

Figure 4-11: The velocities monitored at lower opening throughout iterations.

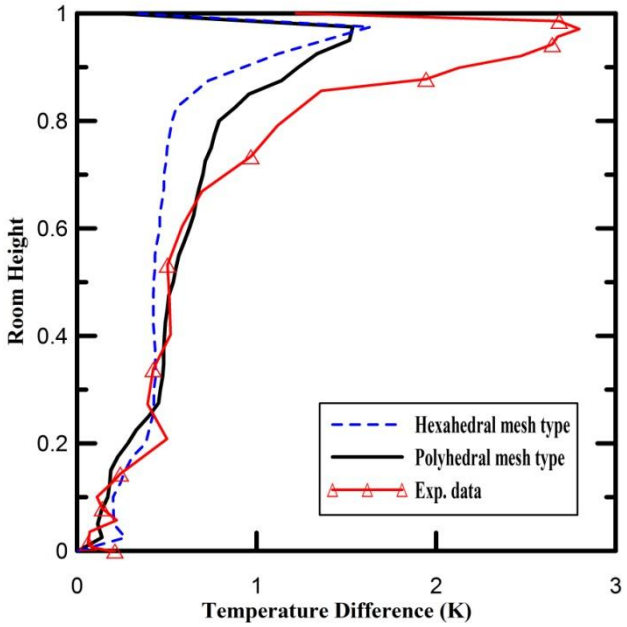

Figure 4-12: The results from models meshed with hexahedral and polyhedral grid

Based on the analysis above, the advantages of utilizing polyhedral mesh for this simulation works is clearly seen. It provides accurate solutions with relatively less amount of mesh cells. This is because the cells of polyhedral mesh type have plenty of neighbours (typically of order 10) which allows a better prediction of both gradients and local flow distribution than that of hexahedral meshes (Peric and Ferguson, 2004). Although this means more storage and computational operations per cell required, it does not make too much difference with modern advanced computational resources. Hence, in order to obtain higher accuracy and better convergence solutions, it is still worth using polyhedral mesh.

In summary, the analysis above has proved that the polyhedral mesh offers accurate solutions with less mesh cells generated, less number of iterations to complete simulation. Hence, the polyhedral mesh was used to create volume mesh for all the models in this study.

4.4 Boundary conditions and time stepping

Before running the simulation, the boundary condition and the size of time step should be determined. In order to simulate the experiments of displacement ventilation flows conducted previously by Sandbach and Lane-Serff (2011b), the boundary conditions of the models were specified to replicate the conditions of the experimental set-up. In the following sections, the boundaries of the computational domain are grouped into four parts for analysis and its boundary conditions are determined accordingly.

The time step is determined based on the condition of Courant-Friedrichs-Lewy (Blazek, 2005). This means the time step should be determined according to the time required to transport information across the spatial discretisation grid in order to obtain converged and stable solutions.

4.4.1 Boundary conditions

The whole computational domain is grouped into 4 parts which are: the chamber, the ceiling of the test room, the sidewalls of the test room, and the floor of the test room part.

Chamber part

For the chamber part, since the size of the chamber is 7.5 times larger in volume than the test room and the heat transfer at its boundaries was not considered in the experiments; hence, the boundaries of the chamber are then specified as adiabatic walls with no slip condition (see Figure 4-13).

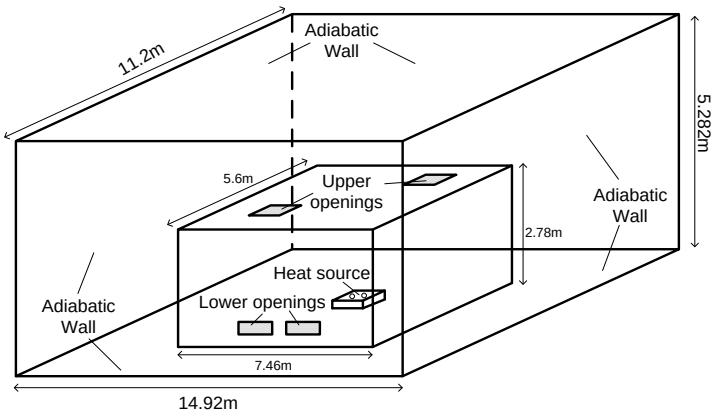

Figure 4-13: The boundary conditions of chamber part (Sandbach and Lane-Serff, 2011b).

Ceiling part

The boundaries of ceiling part considered includes inside and outside ceiling surfaces as shown in Figure 4-14. The ceiling part is made of 0.012m thick of plasterboard which a significant amount of heat lost through it. Its properties are as shown in Table 4-4. Convective heat transfer mechanism is also taken into account for both inside and outside ceiling surfaces.

When the rising buoyancy flows impinge on the ceiling, it spreads out to form a fast local fluid flow. For that reason a stronger convective heat transfer was specified at the inside ceiling surface with a convection coefficient of 42 W m^{-2} K^{-1}. This was obtained from the measurement taken by Sandbach and Lane-Serff (2011b).

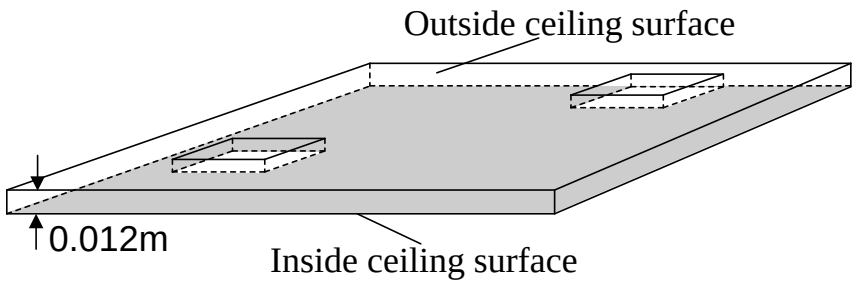

Figure 4-14: The boundaries of ceiling part (Sandbach and Lane-Serff, 2011b).

The convection coefficient of the outside ceiling surface was evaluated by the empirical correlation proposed by Novoselac (2006) (see Figure 4-15). The correlation was developed for floor surface that considers the effect of natural and forced convection; therefore it was a function of supply ventilation flow rate. For outside ceiling surface, the forced convection term is neglected as there is no local advective flow (Sandbach and Lane-Serff, 2011b). The convection coefficient varies with time but a typical value for outside ceiling surface is given 3 W m^{-2} K^{-1}.

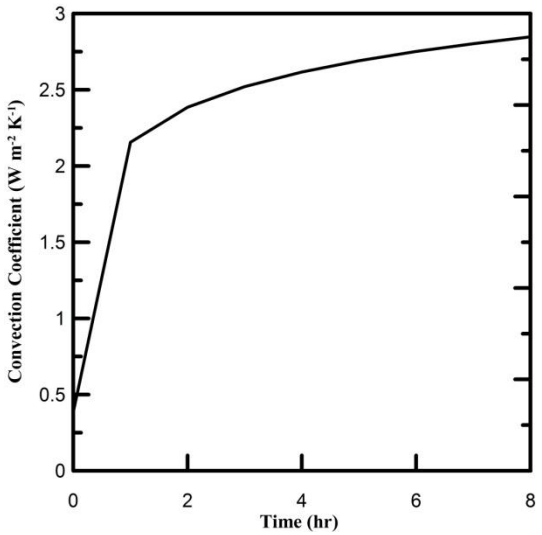

Figure 4-15: The convection coefficient of outside ceiling surface (Sandbach and Lane-Serff, 2011b).

The sidewalls

The sidewalls of the test room were made of two 0.015 m thick plasterboards separated by an air gap measured 0.054 m in width as shown in Figure 4-16. The conductive heat transfer through sidewalls is considered to be very small due to relatively thick air gap. The convective heat transfer at sidewalls was neglected as the heat lost through sidewalls was negligibly small by comparison to the heat lost through the poorly insulated ceiling (Sandbach and Lane-Serff, 2011b).

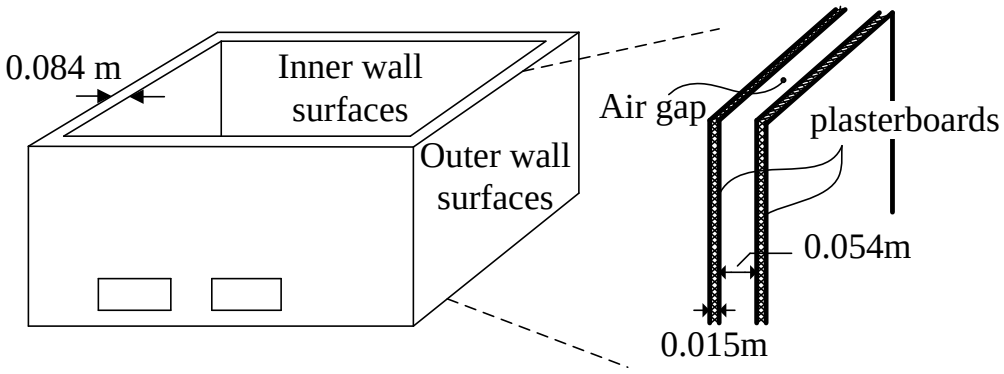

Figure 4-16: The boundaries of test room (Sandbach and Lane-Serff, 2011b).

Floor part

The floor part is made of 0.025m thick chipboard covering metallic surfaces on both sides and a carpet is laid on top of the upper surface. The heat source placed approximately 0.15m above the floor surface was set to generate thermal energy of 1.25 kW or 2.4 kW depending on the cases. The convective heat transfer at the inner surface of the floor was considered. The boundary condition of outer floor surface was assumed to be adiabatic. The convection coefficients were computed by Sandbach and Lane-Serff (2011b) to give a typical value of 2.5 W m^{-2} K^{-1}.

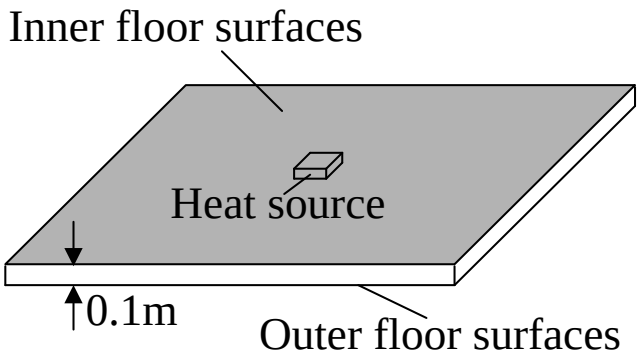

Figure 4-17: The boundaries of floor part (Sandbach and Lane-Serff, 2011b).

4.4.2 Determination of time step

Time-dependent problems can be solved by using explicit or implicit time marching methods. The explicit method is straight forward and does not require iterations. However, it should meet the von Neumann criterion for stability and therefore the criterion brings a maximum time-step restriction. For heat conduction governing equation, the size of the time-step should satisfy the condition

$$\Delta t_c < \rho c_p \frac{(\Delta x)^2}{2k}, \tag{4-1}$$

where ρ is density, c_p is specific heat, k is conductivity, Δx is the size of the mesh cell. For a linear advection equation, the maximum time-step size should meet the condition

$$\sigma = \frac{\Delta t_a v_s}{\Delta x} \leq 1, \tag{4-2}$$

where σ is known as Courant-Friedrichs-Lewy (CFL) coefficient and v_s is the local fluid flow velocity in the domain. The physical meaning of this condition can be interpreted as the distance of the information travelled at one time step should not exceed the size of a mesh. Therefore when using explicit time marching method, all nodal values should be updated at a global time-step to ensure all the physical quantities of the system are captured, i.e.,

$$\Delta t = \min(\Delta t_c, \Delta t_a). \tag{4-3}$$

For semi-implicit scheme such as Crank-Nicolson method, a time-step restriction is still needed for stability. However, there is no time-step restriction requirement for fully implicit method as it is unconditionally stable.

The fully implicit method was employed in this study and the time-step was estimated using Eq. (4-2) as a guide. The size of the mesh cell Δx is the value given for constructing mesh in each simulation case; the value of local velocity is the volume flow rate at lower openings obtained from the literature data presented by Sandbach and Lane-Serff (2011b). This gives the value $\Delta x/v_s$ = 0.72 s in this study. The model was run at time-step of 0.2 s, 1 s and 3 s respectively with the largest Courant number being 4.16. The simulation results at real-time 3 minutes are presented for accuracy checking. The CFL coefficients and the required CPU time are listed in Table 4-6 and the solutions are shown in Figure 4-18.

It can be seen from the figure below that the Courant number should not be too large when determining the size of time-step. Since the size of the time-step does not affect the stability of the results, this study were runs the models at time-step of 1 second for real-time 3, 30, and 60 minutes respectively in order to reduce the use of CPU time.

Table 4-6: The CFL coefficients and the required CPU time for each case.

	$\Delta x/v_s$	σ	Time-steps	CPU time
t_s=0.2s	0.72	0.28	900	107 hr
t_s=1 s	0.72	1.38	180	20.95 hr
t_s=3s	0.72	4.16	60	1.43hr

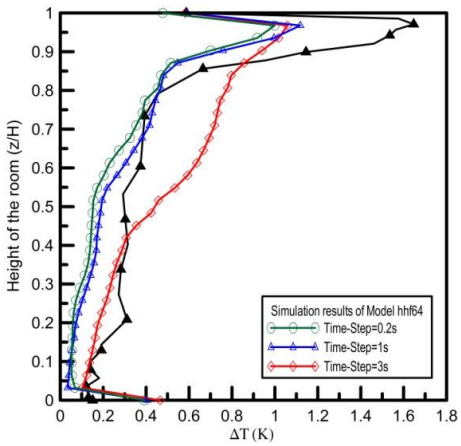

Figure 4-18: The solutions of the model runs at different time-step.

The Lagrangian time scale is a value obtained when the turbulence of the flow is observed by a tracer particle smaller than the lengthscale of turbulence of the flow. An Eulerian flow, on the other hand, describes the turbulence with a probe whose position is fixed. These two values are important both in turbulence and atmospheric pollution dispersion studies. The Lagrangian time scale is defined as:

$$\mathrm{T_L} = \int_0^\infty R_L(\tau)\, d\tau\,, \tag{4-4}$$

where $R(\tau)$ is the Lagrangian autocorrelation function defined as:

$$R_L(\tau) = \frac{\overline{v_p(t)v_p(t+\tau)}}{\overline{v_p^2(t)}}, \tag{4-5}$$

where v_p is the particle velocity in the x direction, and τ is time lag. As the Lagrangian and Eulerian autocorrelation are determined in the same turbulent flow field, it is expected that there is a relationship between the Lagrangian and Eulerian autocorrelation and time scale by a scale factor β. That is,

$$R_L(\beta t) = R_E(t)\,, \tag{4-6}$$

$$T_L = \beta T_E\,. \tag{4-7}$$

The value of scale factor β is found by Angell (1964) and Angell et al. (1971) to have average values of 3 and 4. It is reasonable to have scale factor β greater than one, since the time required by a particle to completely travel around an eddy would be longer than the time needed for it to pass through a position fixed probe. The Eulerian time scale can be estimated by a relation derived by Hanna (1981). That is,

$$T_E = 0.25\,\frac{z_i}{u}, \tag{4-8}$$

where z_i is the mixing depth and u is the flow velocity.

4.5 Determination of absorption coefficient

The spectral absorptivity of non-grey gas varies strongly with wavelength and its absorption bands are function of temperature and pressure. Spectral absorptivity provides high accuracy in radiation calculation; however, it requires detailed quantum-mechanical calculations which can be tedious and time consuming. An alternative way is to determine effective total absorptivity by using emissivity charts presented by Hottel (1967). There are five parameters needed before using these charts to determine emissivity and absorptivity of the gas. These parameters are: partial pressure of H_2O, partial pressure of CO_2, temperature of gas mixture, source temperature, and the pathlength. Once the absorptivity is determined, the absorption coefficient can be calculated by Eq. (3-115).

4.5.1 Determination of partial pressure of H_2O

Air is the working fluid in the study of displacement ventilation flows. The amount of water vapour held in the air determines the magnitude of partial pressure of H_2O. In this study, relative humidity is used to determine the partial pressure of water vapour. The relative humidity is defined as the ratio of the partial pressure of water vapour in the gas mixture to the saturated water vapour pressure at a given temperature. That is,

$$\phi = \frac{p_m}{p_s} \times 100\% \,, \tag{4-9}$$

where p_m is the partial pressure of water vapour in the gas mixture, p_s is the saturated water vapour pressure at a given temperature.

The vapour pressure is defined as the pressure exerted by a vapour which evaporates from its solid/liquid phases in thermodynamic equilibrium state at a given temperature in a closed system as shown in Figure 4-19. The process of phase transition (evaporation) goes on until the amount of particles evaporating equals the amount of particles returning from gas phase. At this point, the vapour is considered to be saturated and is called saturated vapour pressure.

The saturation vapour pressure of a substance is usually estimated using Clausius-Clapeyron equation; however, the vapour pressure cannot be determined before the thermodynamic property enthalpy is known (Çengel, 2011). The Antoine equation, a simple 3-parameter equation, is then used to estimate the vapour pressure of a liquid substance. This equation is the relation between the vapour pressure and the temperature of pure liquid substances and it is proved to fit well to the experimental values. That is,

$$\log p_v = A - \frac{B}{C + T}, \tag{4-10}$$

where p_v is the absolute vapour pressure of a substance, T is the temperature of the substance, A, B and C are substance-specific coefficients. The coefficients of water are: A=10.19621, B=1730.63, C= -39.724 (Poling, 2001).

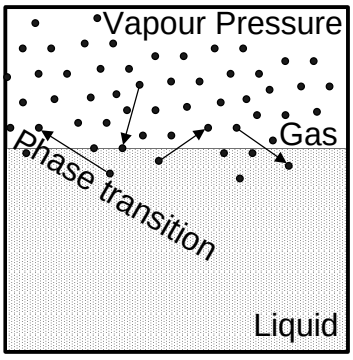

Figure 4-19: Schematic of the vapour pressure as the result of phase transition process.

The values obtained from the Antoine equation were validated with experimental data (Dean, 2005), and found to be reasonably accurate. Once the saturated vapour pressure is determined, the partial pressure of water vapour in the mixture can be obtained by multiplying the relative humidity with the saturated vapour pressure.

4.5.2 Determination of partial pressure of CO_2

According to Dalton's law of partial pressure, the total pressure of a gas mixture is the sum of the partial pressure of each components of the gas mixture. Hence, the partial pressure of carbon dioxide can be determined by the proportion of its volume to the volume of a gas mixture, air. The relation can be expressed as:

$$\frac{v_x}{v_t} = \frac{p_x}{p_t}, \tag{4-11}$$

where v_x is the partial volume of any individual gas component, v_t is the total volume of gas mixture, p_x is the partial pressure of gas x, p_t is the total pressure of gas mixture.

Carbon dioxide occupies around 0.04% of the total volume of air (Feichter et al., 2002) and is assumed to remain constant in this study as human respiration is not considered. Therefore, the partial pressure of the CO_2 in the air is 0.4×10^{-3} atm which is obtained from Eq. (4-11).

4.5.3 Determination of pathlength

The medium in this study is considered optically thick, thus the mean beam length is determined by Eq. (3-118). The value c_b depends on the geometric configuration of the enclosure. In this study, the air is enclosed in a rectangular room which is similar to the configuration as shown in Figure 4-20.

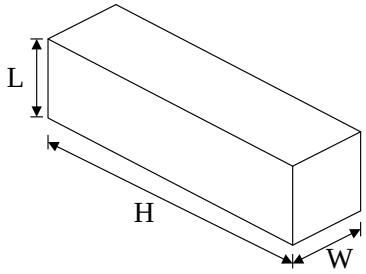

Figure 4-20: Configuration of computational domain.

For optically thick media, the recommended value for correction factor c_b is 0.9 (Brewster, 1992), thus the mean beam length can be calculated through following equations:

$$l_b = c_b \cdot l_{b0} = 0.9\frac{4\boldsymbol{V}}{A}, \tag{4-12}$$

where

$$l_{b0} = \frac{4\boldsymbol{V}}{A} = \frac{4HWL}{2(WL + HL + HW)}. \tag{4-13}$$

4.5.4 Flow chart for calculation of absorption coefficient

The calculation process of absorption coefficient is summarised in Figure 4-21. First of all, the condition of the air on the day which experiment was conducted is assumed to be the condition from the weather report. The partial pressure of water vapour in the air was calculated based on the value of relative humidity and temperature given in the weather report (The condition is assumed to be the same as in the laboratory). The partial pressure of carbon dioxide is calculated using Dalton's law. The proportion of its volume to the total volume of air is assumed to remain the same for all cases. The pathlength is determined from Eq. (4-12) and Eq. (4-13). The temperature of the gas mixture is the temperature outside of the test room. The temperature of blackbody source is the temperature of the heat source; the blackbody temperature is given 710 K at heat source 2.4 kW and 610 K at heat source 1.25 kW.

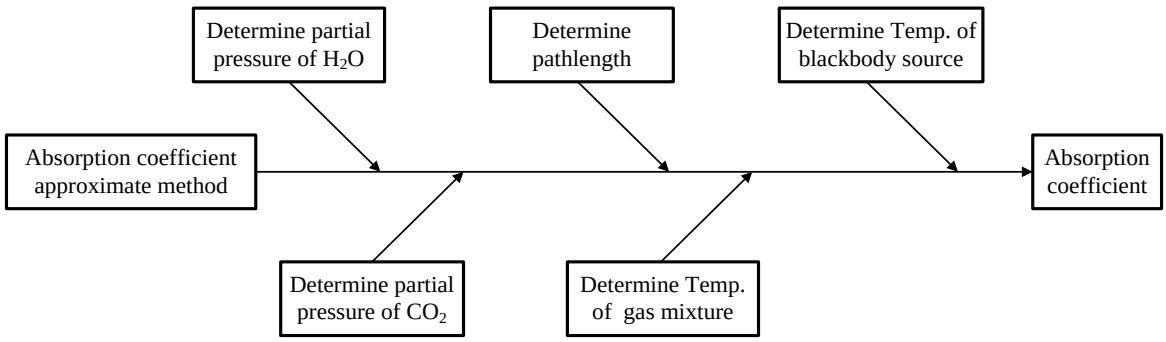

Figure 4-21: Flow chart summarising the calculation of absorption coefficient.

4.5.5 The absorption coefficients of each experiment cases

By using the equations detailed above, the absorption coefficient of each case under the condition of the date was determined. There are four sets of experimental measurements in total conducted by Sandbach and Lane-Serff (2011b). The measurements in each set were conducted on different dates as shown in Table 4-7, Table 4-8, Table 4-9, and Table 4-10. The experiments were conducted in between January and May, 2006; the temperature and relative humidity of the air were determined from the historical weather report data on the date (http://www.wunderground.com). The experiments at all conditions were fully conducted in Set-1, and were partly conducted in Set-2, Set-3, and Set-4 as shown in the tables below. The absorption coefficient of each case was calculated accordingly.

Table 4-7: Conditions and Absorption coefficients of each case, Set-1*.

Exp. Date	Effective opening	Heat source (kW)	Mean Temp. (K)	Relative humidity (%)	*1Ext. Temp. (K)	Absorption coefficient (m^{-1})
04-Jan	0.019	1.25	274	96	287	0.033
22-May	0.019	2.35	283	86	291	0.041
03-Jan	0.03	1.25	278	92	286	0.037
15-May	0.03	2.35	285	89	293	0.044
30-Jan	0.052	1.25	274	90	287	0.032
15-Feb	0.052	2.35	275	62	288	0.038
31-Jan	0.065	1.25	274	92	287	0.032
07-Mar	0.065	2.35	276.5	99	286	0.035

*(Sandbach and Lane-Serff, 2011b) [1](Temperature outside the test room)

Table 4-8: Conditions and Absorption coefficients of each case, Set-2*.

Exp. Date	Effective opening	Heat source (kW)	Mean Temp. (K)	Relative humidity (%)	*[1]Ext. Temp. (K)	Absorption coefficient (m^{-1})
06-Jan	0.019	1.25	275	89	286	0.033
--	0.019	2.35	--	--	--	--
unknown	0.03	1.25	--	--	286	--
16-May	0.03	2.35	286	86	293	0.045
06-Feb	0.052	1.25	280	77	287	0.036
13-Feb	0.052	2.35	282	93	287	0.041
09-Mar	0.065	1.25	279.9	95	288	0.040
09-Feb	0.065	2.35	275	62	288	0.027

*(Sandbach and Lane-Serff, 2011b) [1](Temperature outside the test room)

Table 4-9: Conditions and Absorption coefficients of each case, Set-3*.

Exp. Date	Effective opening	Heat source (kW)	Mean Temp. (K)	Relative humidity (%)	*[1]Ext. Temp. (K)	Absorption coefficient (m^{-1})
05-Jan	0.019	1.25	275	81	286	0.032
--	0.019	2.35	--	--	--	--
unknown	0.03	1.25	--	--	--	--
--	0.03	2.35	--	--	--	--
--	0.052	1.25	--	--	--	--
08-Feb	0.052	2.35	278	80	287	0.033
02-Feb	0.065	1.25	271.8	94	287	0.030
--	0.065	2.35	--	--	--	--

*(Sandbach and Lane-Serff, 2011b) [1](Temperature outside the test room)

Table 4-10: Conditions and Absorption coefficients of each case, Set-4*.

Exp. Date	Effective opening	Heat source (kW)	Mean Temp. (K)	Relative humidity (%)	*[1]Ext. Temp. (K)	Absorption coefficient (m^{-1})
--	0.019	1.25	--	--	--	--
--	0.019	2.35	--	--	--	--
unknown	0.03	1.25	--	--	--	--
--	0.03	2.35	--	--	--	--
--	0.052	1.25	--	--	--	--
--	0.052	2.35	--	--	--	--
16-Mar	0.065	1.25	274.5	79	287	0.031
--	0.065	2.35	--	--	--	--

*(Sandbach and Lane-Serff, 2011b) [1](Temperature outside the test room)

All the absorption coefficients obtained from data sets above are listed in chronological order in the Table 4-11 and then were plotted against relative humidity in Figure 4-22 to investigate how it varies with the variation of relative humidity.

Table 4-11: List of absorption coefficients and relative humidities on each date.

Date of Exp conducted*	Avg. relative humidity	Absorption coefficients
3rd-Jan	92	0.037
4th-Jan	96	0.033
5th-Jan	81	0.032
6th-Jan	89	0.033
30th-Jan	90	0.032
31st-Jan	92	0.032
2nd-Feb	94	0.030
6th-Feb	77	0.036
8th-Feb	80	0.033
9th-Feb	62	0.027
13th-Feb	93	0.041
15th-Feb	86	0.038
7th-March	99	0.035
9th-March	95	0.040
16th-March	79	0.031
15th-May	89	0.044
16th-May	86	0.045
22th-May	86	0.041

*Experiments conducted in 2006 by Sandbach and Lane-Serff (2011b)

In this figure we can see that the absorption coefficients vary according to the relative humidity; the coefficients increase when the relative humidity of the air rises and decreases otherwise. This phenomenon matches with what was observed in the earlier studies reviewed in Section 2.8; the water vapour in the air has a significant influence on the magnitude of the absorption coefficient. Both water vapour and carbon dioxide are the two strongest absorptances found in the air. As the total amount of carbon dioxide in the air is assumed to be constant in this study, the amount of humidity in the air will have the major influence on the absorption coefficients.

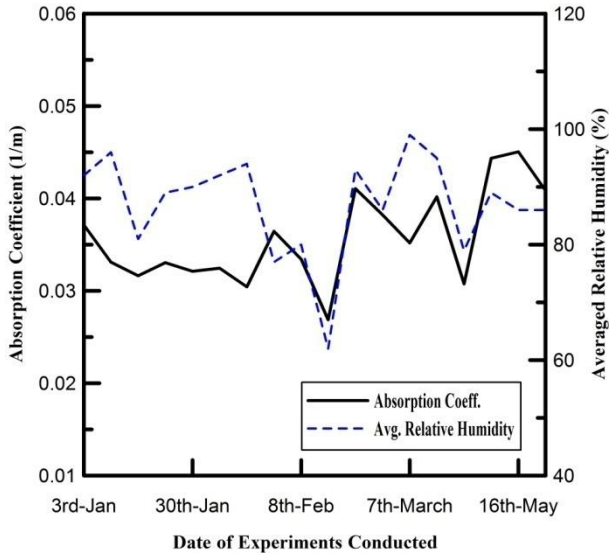

Figure 4-22: The variation of absorption coefficient to relative humidity.

The influence of vapour pressure to the absorption coefficient can be better seen from Figure 4-23. This figure shows that the partial pressure of water vapour increases with higher relative humidity of the air under the same ambient air temperature. With higher partial pressure of water vapour, the absorption coefficient has also shown to increase accordingly. From this figure we can confirm that the absorption coefficient is directly in relation to the partial pressure of water vapour in the air.

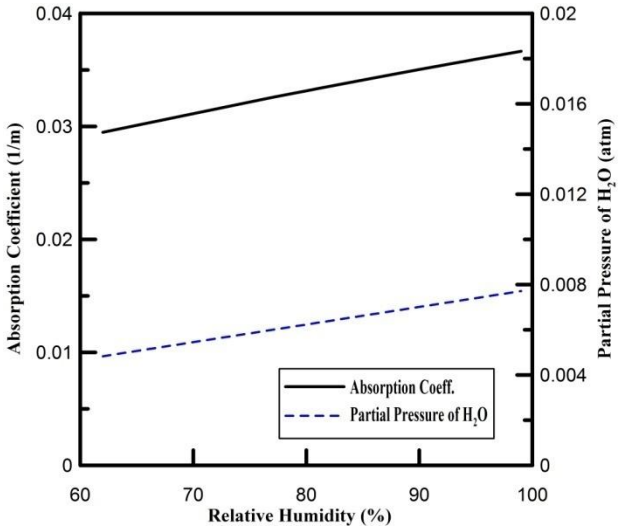

Figure 4-23: The variation of absorption coefficient to partial pressure of H_2O.

The relation of absorption coefficient to air temperature is shown in Figure 4-24. With a fixed partial pressure of water vapour, the figure shows that the coefficient decreases with an increasing air temperature. This was shown to have the same trend as Planck-mean absorption coefficient presented by Rothman (1998). There is an approximately linear relation in between absorption coefficient and air temperature in the region of 250K to 500K.

In terms of the sensitivity of absorption coefficient to blackbody temperature, the absorptivity is most sensitive to the temperature at wavelength near 2.7 μm and 15 μm for H_2O and CO_2 at 300K and 1,000K (Berour et al., 2004). For the cases studied in the thesis, the blackbody temperatures vary within 100K, the variation of absorption coefficients over the range of the temperatures is from 3.5% to 4.5%.

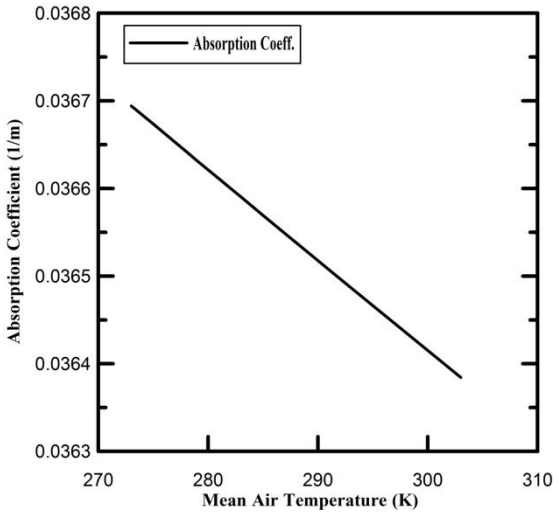

Figure 4-24: The variation of absorption coefficient to air temperature.

4.6 Size of grid cells to spatial resolution

One of the important processes in conducting CFD modelling is constructing mesh. Before solving the governing equations, the whole computational domain needs to be discretised by small size of geometrical elements known as grid cells. The number of grid cells generated inside the ventilation flow domain determines the level of the spatial resolution and the accuracy of the modelling. In this section three different sizes of grid, coarse, medium, and fine grid, were generated respectively for model Hf64 listed in Table 4-2. A polyhedral mesh type was used to generate the grids for the computational domain.

The computational domain is separated into two parts by the boundary of the test room. The region outside the test room is generally filled with relatively large cells, as only the thermal distribution inside the test room is of interest. The size of the grids generated inside the test room determines the degree of refined grids. The cells near to the ceiling surface and floor surface are further refined in order to capture the steep temperature gradients in those regions. Prism layers were generated at the boundaries of the test room. A total thickness of 0.1 m of two prism layers was generated for coarse mesh cases; a total thickness of 0.03 m of four prism layers was generated for medium and fine mesh models. The specifications and total number of grids generated for coarse, medium, and fine mesh are given in Table 4-12. It can be seen from the table that the finer the mesh, the longer the CPU time is needed for every time-step. However, a fine mesh provides a better resolution to the computational domain and generally a more accurate solution.

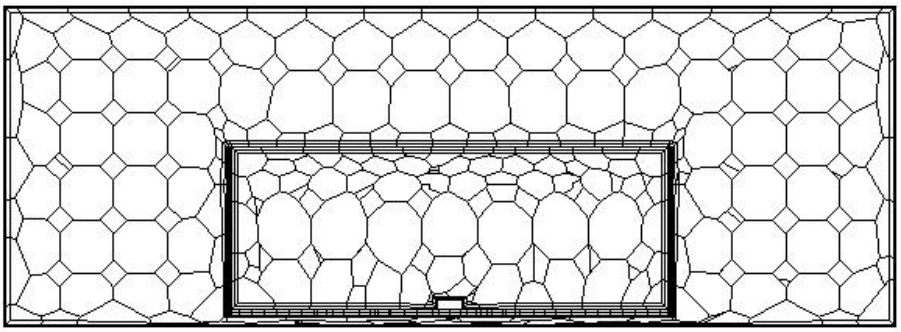

(a)

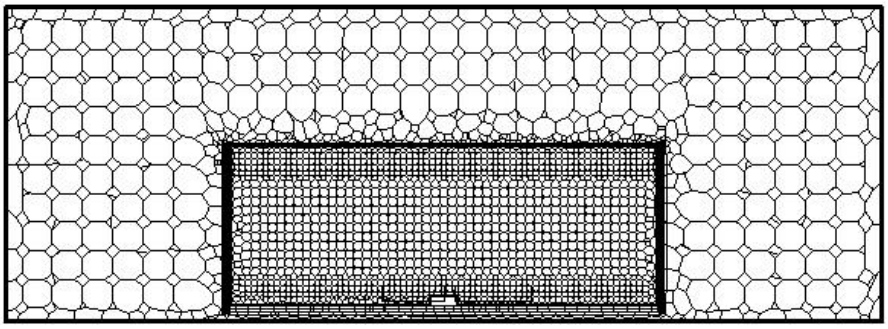

(b)

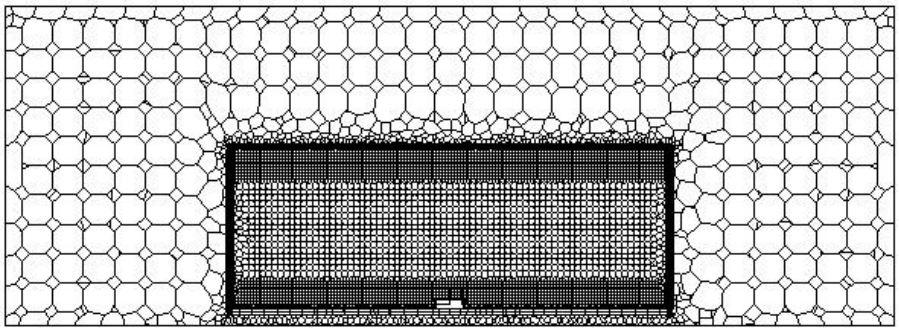

(c)

Figure 4-25: Schematic of mesh generated with (a) coarse mesh, (b) medium mesh, (c) fine mesh.

Table 4-12: The time-step required by three different sizes of mesh.

Mesh size / Items	Coarse Mesh	Medium Mesh	Fine Mesh
Number of cells	64,139	323,534	1,371,667
Number of prism layers	2	4	4
Prism layer thickness (m)	0.1	0.03	0.03
CPU time per time-step (s)	27.96	78.25	228.2

4.6.1 Contours of temperature magnitude

The thermal distributions of the test room predicted by models meshed by coarse, medium and fine grid sizes are presented in the Figure 4-26. It can be seen from the figures that the coarse grids model gives the roughest temperature contour among all other models. In the region adjacent to the ceiling surface, the coarse prism layers result in an underestimated magnitude of the temperature and also a relatively large y^+ value in comparison with medium and fine meshed models as shown in Table 4-13. The detail of the temperature gradient was not captured by the coarse meshed model.

Numerical diffusivity is proportional to the size of grid, therefore increasing the grid size will enlarge the numerical diffusivity (Sørensen and Nielsen, 2003). It can be seen from the figures that there is a relatively large numerical diffusivity in the coarse meshed model. The numerical diffusivity under the stratification layers from the coarse meshed model is larger in comparison with the medium and fine meshed models. The unpolluted area is far narrower than the medium and fine meshed ones.

Although the thermal distribution around the top of the plume are slightly different, the modelling results from medium and fine meshed models are generally in good agreement in most parts of the domain. This can also be seen from the prediction of the eddy viscosity presented in Figure 4-27. The eddy viscosity predicted by medium

and fine mesh are generally identical whereas the viscosity was under predicted at the upper region and over predicted at the lower region by the coarse meshed model.

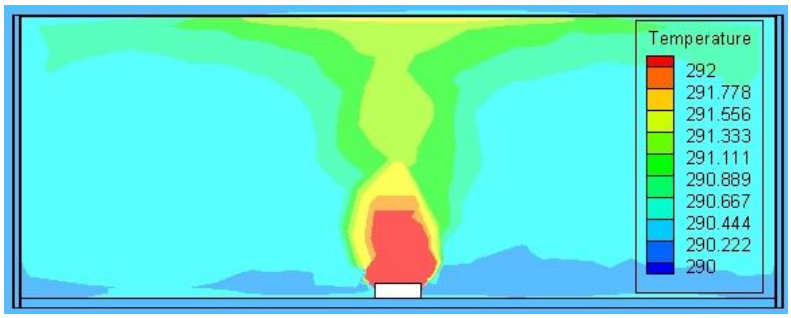

(a)

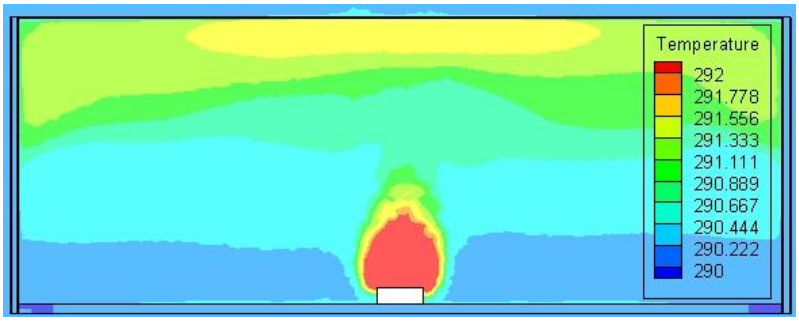

(b)

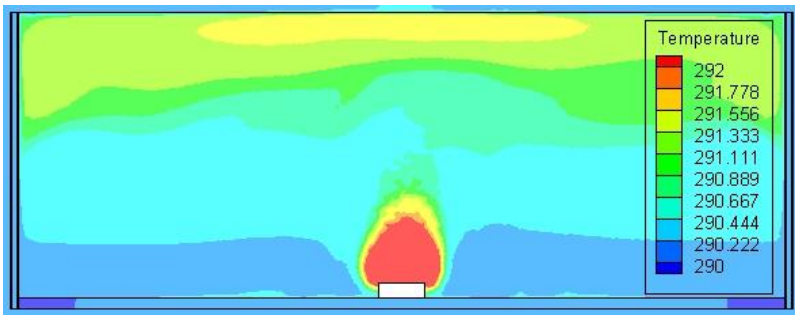

(c)

Figure 4-26: Contours of temperature modelled using (a) coarse mesh, (b) medium mesh, (c) fine mesh.

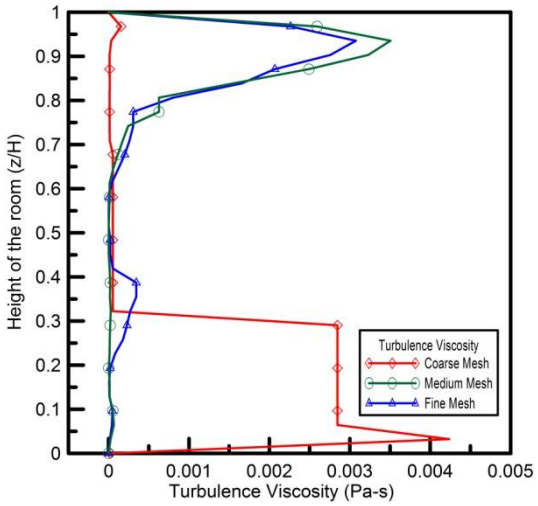

Figure 4-27: The predictive eddy viscosity from different sizes of grids.

The y^+ value is proportional to the size of grid generated. The y^+ value represents a non-dimensional distance from the wall to the first mesh node, therefore the larger the grid size the bigger the y^+ value (see Table 4-13). In order to obtain an accurate solution, the y^+ value should be kept within a certain range so the first node does not fall outside the boundary layer region. In this study case, unlike the coarse meshed model, the y^+ values of medium and fine meshed models are below 5 which were all within the pure viscous sub-layer region (Schlichting, 1962).

Table 4-13: The comparison of y+ values at ceiling and floor surfaces.

Mesh size / Items	Coarse Mesh	Medium Mesh	Fine Mesh
Ceiling surface			
y^+	22.7	2.52	2.53
Floor surface			
y^+	11.4	0.97	1.01

4.6.2 Grid-independent check

Grid-sensitivity study was carried out by comparing the modelling results obtained from models meshed with three different grids. All three models used the realisable two-layer k-ε model given in Section 3.2.3 to simulate the buoyancy-driven ventilation flows. The modelled temperature profiles of the test room were plot in Figure 4-28. It can be seen from the figure that the modelling results of medium mesh matches reasonably well with the measurements. A further refinement on the computational cells does not alter the solution significantly. Hence, the solution of medium mesh can be considered grid-independent result.

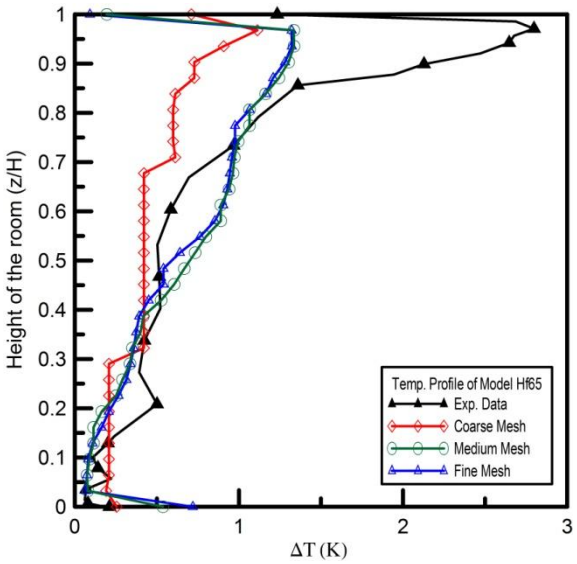

Figure 4-28: Temperature profiles of model Hf65 for mesh sensitivity study.

4.7 Turbulence models

This section studies the performances of the turbulence models in modelling the buoyancy-driven ventilation flows. In order to have a clear view of the performance of each turbulence model, the case of model hhf19 from Table 4-3 was selected to carry out the study as it has the smallest mass flow rate among all models and potentially has the most complex airflows existed inside the ventilated space.

This is because in the case of low heat flux and small opening, the buoyancy force drives the flow through the opening is small. Hence, the flow can be at different status in different region in the enclosure. There is turbulent flow right above the heat source which the turbulent stresses dominate. The viscous stresses are dominated in the region near the boundary surfaces away from the heat source. Hence, the case with low heat flux and small opening is considered to have the most complex airflows, and the simulation results are expected to be sensitive to the turbulence model selected.

The turbulence models selected for studying their performances are: standard k-ε model, realisable two-layer k-ε model, low Reynolds k-ε model, and $\overline{v^2}$-f turbulence model. The computational domain of model hhf19 was meshed with fine mesh as shown in Table 4-12. The model runs for a real time 180 seconds at each time-step of 1 second. The predicted results from each model were then validated with experimental data.

4.7.1 High and low Reynolds turbulence models

The predicted results from standard k-ε model, low Reynolds turbulence model with low y^+ wall treatment and low Reynolds turbulence model with all y^+ wall treatment were analysed and compared with the experimental data in this section. The standard k-ε model is one of the most popular two-equation turbulence models which is often used for modelling fully developed well-mixed and isotropic eddy viscosity turbulent flows. However, in a buoyancy dominated displacement ventilation flow

region, the air flows inside the region are often very complex and usually consist of many types of airflows. There are high turbulent flows in the region such as the airflows coming in from the lower openings of the test room and the vertical buoyancy plumes jet produced from heat sources. There are also low turbulent flows in the regions with strong damping effects: the wall damping effect in the near-wall region and damping effect caused by buoyancy in the region under the stable stratification layers.

Due to the assumption of isotropic turbulence, standard k-ε model can perform poorly in those regions where the turbulence is significantly damped out (Nielsen, 2004). This phenomenon can be seen by comparing the velocity contour predicted by both standard k-ε model and low-Reynolds k-ε model as shown in Figure 4-29 below. It can be seen from the figure that when the buoyancy flows reach the ceiling surface and begin to spread out horizontally, the growth rate of airflow predicted by the standard k-ε model is shown to be at the same level both in the direction perpendicular to the ceiling and parallel to the ceiling (Figure 4-29 (a)). The predicted growth rate of airflow by low-Reynolds k-ε model is shown to be smaller in the direction parallel to the ceiling but higher in the direction perpendicular to the ceiling due to the damping effect (Figure 4-29 (b)).

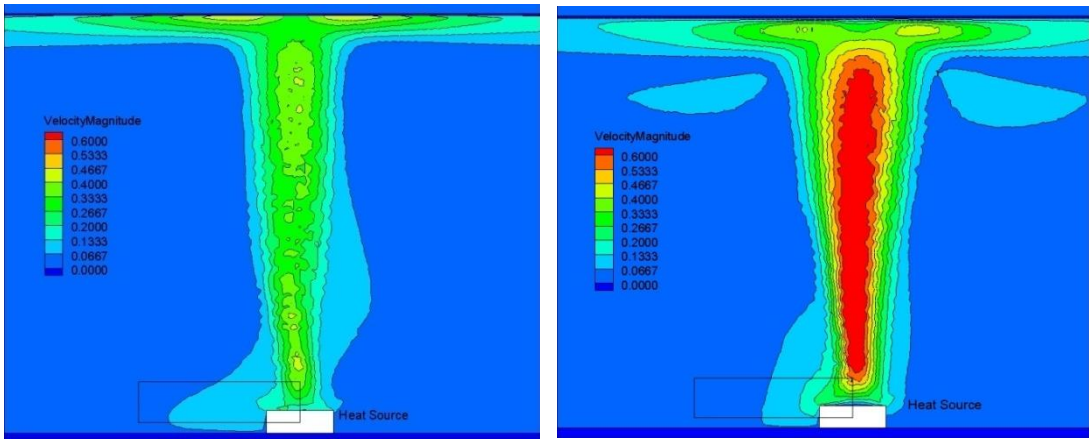

(a) (b)

Figure 4-29: Contour of airflow velocity modelled by (a) standard k-ε model; (b) low-Reynolds model.

The flow recirculated in between the ceiling and side wall predicted by both standard k-ε model and low-Reynolds k-ε model were also compared as shown in Figure 4-30. When the spreading outflows near the ceiling surface reach the side-wall of the room, a flow recirculation begins to form in between the surfaces. It can be seen from the figures that due to the lack of consideration of damping effect, the scale of the flow recirculation predicted by standard k-ε model is relatively larger than the predicted result from the low-Reynolds k-ε model. The inaccurate predictions of flow recirculation can lead to an over/under estimated thickness of plume layers; since the scale of flow recirculation is closely related to the development of plume layers (Kaye and Hunt, 2007).

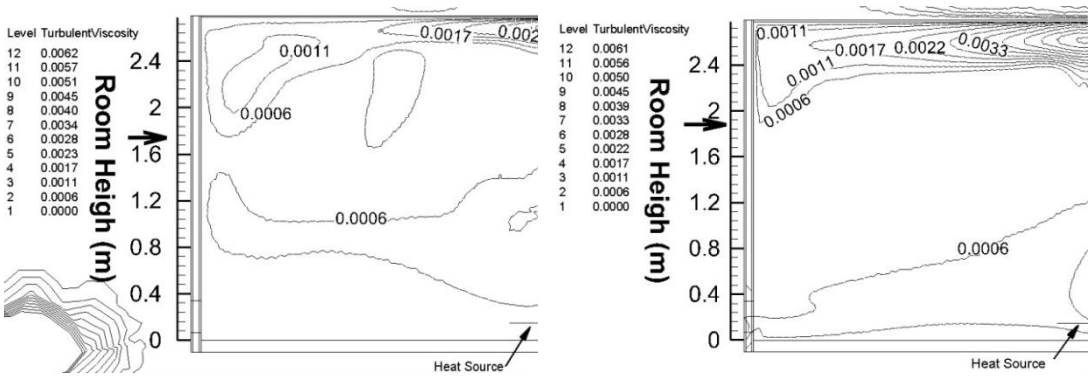

(a) (b)

Figure 4-30: Contour of eddy viscosity modelled by (a) standard k-ε model; (b) low-Reynolds model.

Lastly, the predicted temperature profiles of the test room were compared and shown in Figure 4-31. It can be seen from the figure that the standard k-ε model provides generally satisfactory results but fails to capture the large temperature gradients in the region close to the ceiling surface. The low y^+ wall treatment low Reynolds turbulence model, on the other hand, has better performance in the region close to the ceiling surface but the position of stratification layer and the temperature profiles in the lower half were poorly predicted. In the commercial programme Star CCM+,

an all y^+ wall treatment was provided when the turbulence model contain damping functions.

The all y^+ wall treatment is a blended wall treatment in which its wall boundary condition for dissipation rate ε is consistent with the two-layer formulation model (see Section 3.2.3). It is designed to give a similar result to low y^+ wall treatment when $y^+ \to 0$, to high y^+ wall treatment when $y^+ >> 30$ and to give reasonable results for the flows in the buffer layer ($5 < y^+ < 30$) where neither high nor low y^+ wall treatment holds. The all y^+ wall treatment represents the buffer layer region by smoothly blending the laminar (viscous sublayer) and turbulent (logarithmic regions) profiles together. The all y^+ wall treatment low Reynolds turbulence model provides a sufficiently accurate temperature profile in lower half and upper half of the regions; however, the location of the stratification interface was inaccurately predicted.

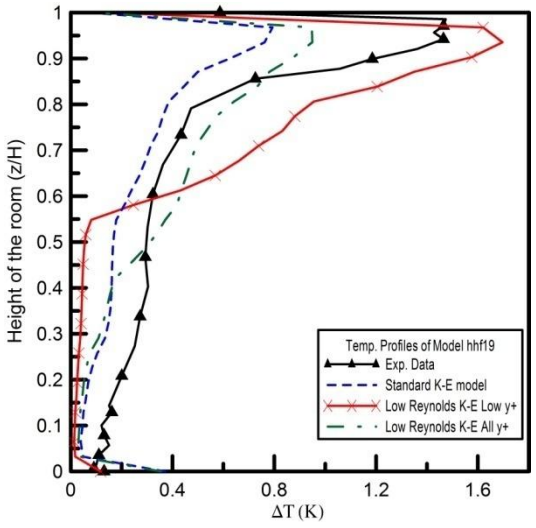

Figure 4-31: Temperature profiles predicted by high and low turbulence models.

4.7.2 Blended turbulence models

In order to deal with the complexity of the turbulent flows in the ventilated region, some standard turbulence models were modified and blended with additional equations so that these turbulence models can not only compute high Reynolds turbulent flows, they can also model the turbulent flows in the near-wall region. This section studies the performance of realisable two-layer k-ε model and $\overline{v^2}$-f low-Reynolds number k-ε model.

The realisable two-layer k-ε model consists of a k-ε turbulence model and a pair of turbulence length scale equations (see Section 3.2.3). By determining the switching criterion in the blending function, the two-layer turbulence model solve the differential transport equation for dissipation rate for the flow outside boundary layer; the dissipation rate is solved by algebraic equation for the flow in the near-wall region. There are many types of one-equation turbulence models developed for different types of turbulent flows. There are three types of two-layer turbulence models to be selected in Star CCM+: Wolfshtein shear-driven model (Wolfshtein, 1969), Norris shear-driven model (Norris, 1975) and Xu buoyancy-driven model (Xu et al., 1998).

As the turbulence length scales model developed by Norris are very similar to the model developed by Wolfshtein (see Section 3.2.3), the simulations results from the two models were also found to be closely alike. This is also observed early by Xu et al., (1998) and also in this study (see Figure 4-32). Thus, the two-layer turbulence model developed by Norris was not employed for modelling in this study.

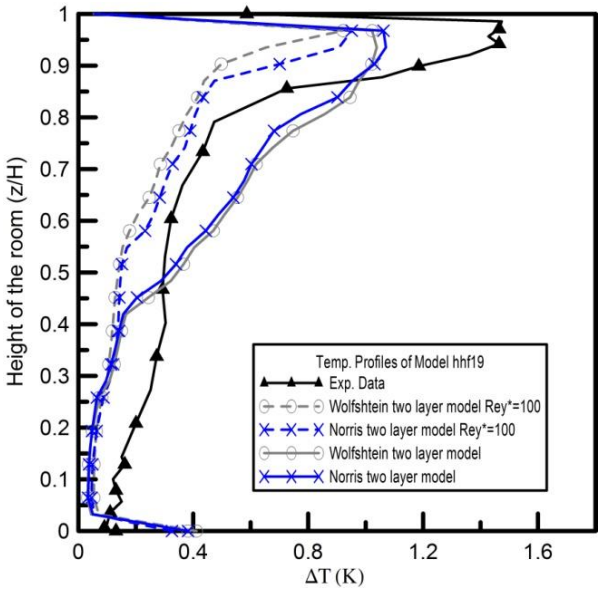

Figure 4-32: The predicted results using the turbulence models developed by Norris and Wolfshtein.

In this section, the shear-driven (Wolfshtein, 1969) and buoyancy-driven (Xu et al., 1998) types of two-layer turbulence models were selected for study. As the buoyancy-driven types of two-layer model was developed from experimental data of a turbulent natural convection flow, it can be seen from Figure 4-33 that buoyancy-driven two-layer model captures the temperature gradient near to the ceiling surface wall. $\overline{v^2}$-f low-Reynolds number k-ε model, also known for its capability of modelling the near-wall turbulent flows (see Section 3.2.5), also predicts a similar temperature profile. The simulation result of shear-driven two-layer model, on the other hand, does not have a good agreement with the experimental data in the near-wall region. The switching criterion for both buoyancy-driven and shear-driven two-layer turbulence models were at default value Re_y^* =60.

As $\overline{v^2}$-f low-Reynolds number k-ε model solves two extra differential equations, wall normal stress function $\overline{v^2}$ and elliptic function f, it requires more CPU time for simulation; hence, buoyancy-driven two-layer model is selected for simulation in this study.

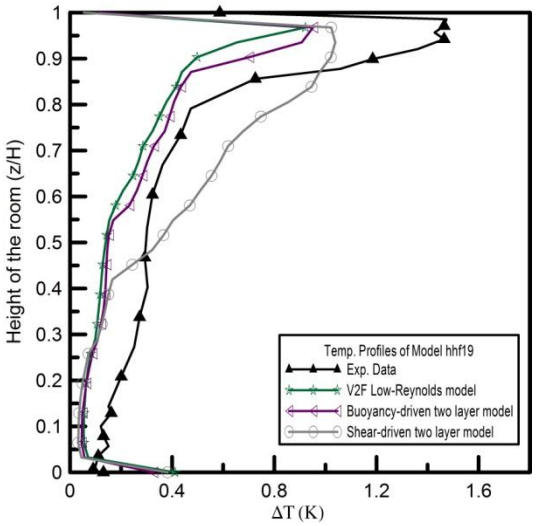

Figure 4-33: Temperature profiles predicted by blended turbulence models.

4.7.3 Switching criterions of two-layer model

The switching criterion Re_y^* in the blending function ϕ (Eq. (3-49)) determines when the transition from one model to another takes place. The values of switching criterion typically range from 50 to 200 which makes sure that the transition only occurs in the outer-wall region (Jongen, 1998). When the wall-distance based Reynolds number Re_y smaller than the switching criterion Re_y^*, ($Re_y << Re_y^*$), then the dissipation rate of the flow is solved by algebraic equation; otherwise, it is solved by differential dissipation transport equation.

The mechanism of transition is illustrated in Figure 4-34 and Figure 4-35 with switching criterion Re_y^*=100 and 200 respectively. The turbulence dissipation rate at the near-wall region of the ceiling surface was computed by the two-layer turbulence model. The y-axis on the left of the plot represents the magnitude of dissipation rate; the y-axis on the right represents the value of function ϕ. The y value on the x-axis represents the distant from the ceiling surface.

In the case of Re_y^*=100 (see Eq. (4-14)), the blending function $\phi \rightarrow 0$ (as the dash line shown in the figures) when Re_y << 100 switching the turbulence model to one-equation model for modelling (see Eq. (3-47)). When the wall-distance based Reynolds number increases, $Re_y >> Re_y^*$, the blending function $\phi \rightarrow 1$; then the model switches back to two-equation k-ε turbulence model for modelling.

$$\phi = \frac{1}{2} \cdot \left[1 + \tanh\left(\frac{Re_y - 100}{c_A}\right)\right]. \qquad (4\text{-}14)$$

A high criterion value, Re_y^*=8,000, was given to the model to produce the benchmark solution of one-equation model; and the solution from the realisable k-ε turbulence model (RKE) was taken as the benchmark solution represents the solution of two-equation k-ε turbulence model. As can be seen from both Figure 4-34 and Figure 4-35, the solutions were closely matched to the solutions from one-equation model in the region of $\phi \rightarrow 0$, and to the solutions from two-equation model in the region of $\phi \rightarrow 1$. It is also clear to see that the one-equation model employed region is widened when giving larger criterion values, and vice versa.

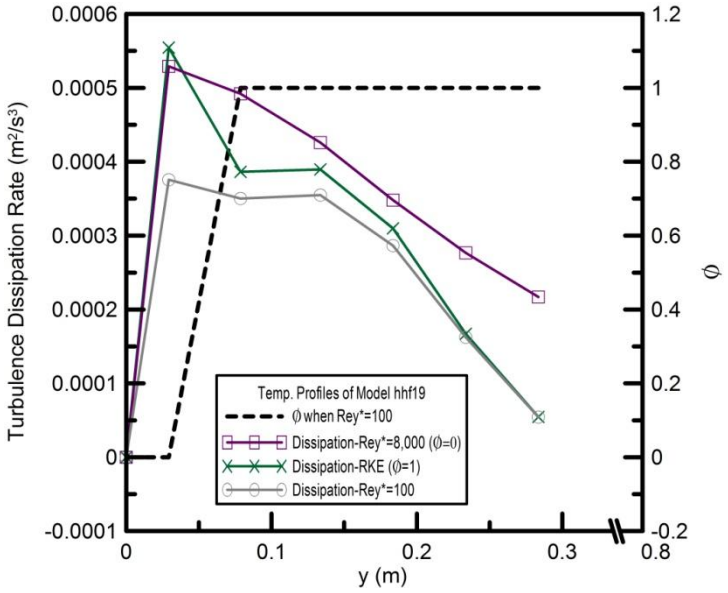

Figure 4-34: The dissipation rate at near-wall region of ceiling surface (Re_y*=100).

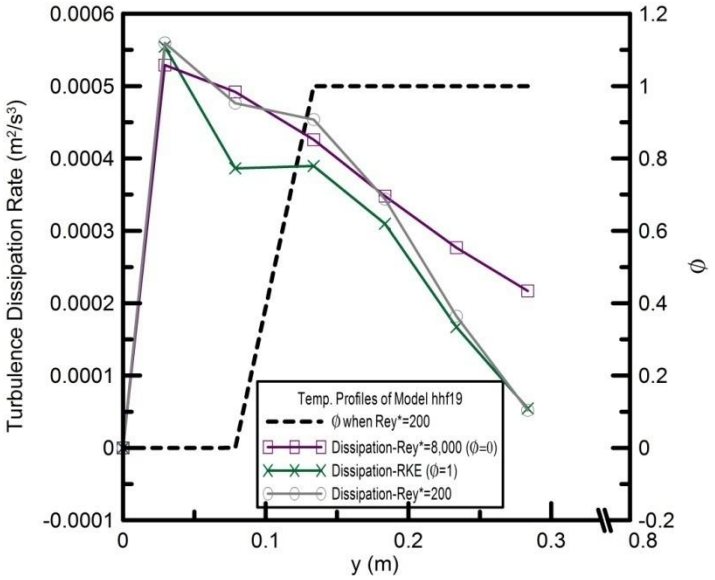

Figure 4-35: The dissipation rate at near-wall region of ceiling surface (Re_y*=200).

The predicted temperature profiles of the case model-hhf19 were also compared with the measurements for accuracy checking. The switching criterion selected for modelling the case were default value 60, 100, 160 and 200 (Jongen, 1998). The shear-driven turbulence length scales set developed by Wolfshtein (1969) was employed for solving the near-wall region flows. It can be seen from Figure 4-36 that the accuracy of the predicted result was closely related to the switching criterions. The results show that the value of switching criterions Re_y^* determines how far away from the ceiling wall the eddy viscosity was modelled by the turbulence length scale.

Another turbulence length scales set called buoyancy-driven mode developed by Xu (1998) in Star CCM+ was also selected for modelling. The predicted results were also varied with the switching criterion chosen (see Figure 4-37). In general, the predicted results of model hhf19 are not sensitive to switching criterion from Re_y^*=160 to 200. Since the simulation result at switching criterion Re_y^*=60 agrees well with the measurements, the default switching criterion was selected for modelling. For the shear-driven model, the predicted result at switching criterion Re_y^*=60 was not satisfactory; Re_y^*=100, on the other hand, provides a better predictive accuracy both on the temperature distribution and the position of thermal stratification (see Figure 4-36).

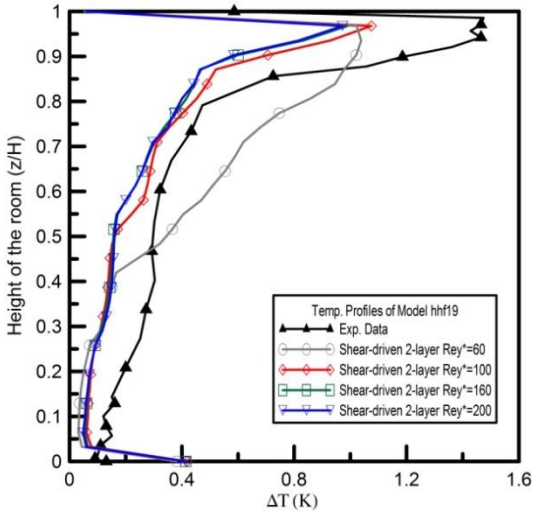

Figure 4-36: Temperature profiles predicted using turbulence length scale developed by Wolfshtein (1969) at different Re_y^* values.

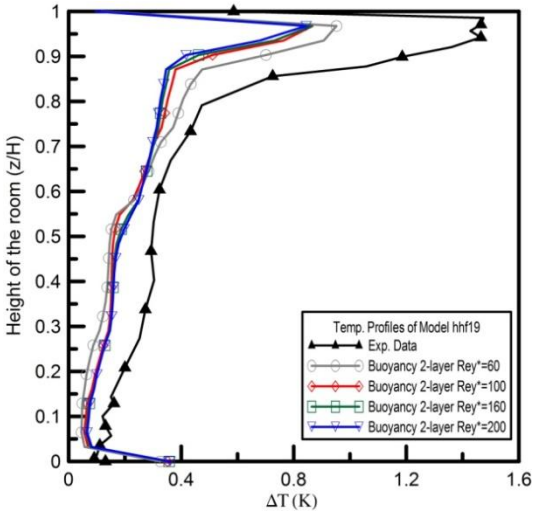

Figure 4-37: Temperature profiles predicted using turbulence length scale developed by Xu (1998) at different Re_y^* values.

4.7.4 Conclusions

From the analysis conducted above, the accuracy of the solutions can be mainly influenced by two factors: mesh cell size and the selection of turbulence models. It can be seen from Section 4.6 that an inadequate amount of cells generated in the computational domain could result in poor predictive accuracy of solutions. Hence, it is important to carry out grid-independent test before conducting any simulation works (Deevy, 2006)

The determination of turbulence model is also an important step towards getting accurate solutions. There are many different types of turbulence models developed to deal with different kinds of fluid dynamic problems; therefore, selecting the turbulence model accordingly will provide better simulation results. In the case of buoyancy-driven displacement ventilation flow, the ventilated space often contains a wide range of airflow elements with different levels of turbulence. There are high turbulent flows in the region above heat sources and near the openings; there are low turbulent flows in the near-wall regions and in the region adjacent to the stratification layer where flows relaminarized as the result of damping effects. Since every turbulence model has its own limitations, a turbulence model only performs well on certain type of turbulent flow problem. Hence, a comparison of the performances of turbulence models is essential for selecting turbulence model (Section 4.7).

Standard k-ε model is the most widely used turbulence model for all types of CFD modelling. It has also presented a fairly good prediction of temperature profile as shown in Figure 4-31. However, as it assumes the turbulence qualities are isotropic, it performs poorly on predicting the flows which are affected by damping effects. Low-Reynolds k-ε turbulence model, on the other hand, considers the damping effects by employing damping functions; therefore, it performs better in the near-wall region where damping effect takes place.

To model ventilated spaces where high and low turbulent airflows co-existed, $\overline{v^2}$-f low-Reynolds number k-ε model and two-layer turbulence models are suggested for modelling as these models also consider the damping effects (Zhang et al., 2007) (Mohammadi and Puigt, 2001). These two types of blending turbulence models did actually provide fairly good results as shown in Figure 4-33. Among the turbulence models tested, the two-layer turbulence model is the most cost-effective model for the cases studied. In comparison to all other turbulence models, the two-layer turbulence model has provided the most accurate results with less computation time (see Table 4-14). It was also pointed out in the earlier research that the two-layer turbulence model requires less mesh cells than low-Reynolds turbulence model in the near-wall region to provide acceptable results (Xu and Chen, 2001).

Table 4-14: The comparison of CPU time consumed by each turbulence model.

Items \ Turbulence models	Low-Re k-ε	Std k-ε	V2F	2-layer model
Cores used	8	8	8	8
CPU time per time step (s)	6017.9	6839	5909	4566.8
CPU time per core per time step (s)	752.3	854.9	738.6	570.9

The two-layer turbulence model developed by Wolfshtein (1969) and Xu (1998) named shear-driven model and buoyancy-driven model respectively in StarCCM+ were employed for modelling in this study. From the predicted results shown in Figure 4-36 and Figure 4-37, it can be seen that the predicted results have a discernible reliance on the switching criterions, Re_y^*, within the range of $50 < Re_y < 200$. Since the selection of the switching criterion is purely based on the experience (Xu et al., 1998), the determination of the criterion in this study was based on the knowledge built previously. The criterion values of 80 and 160 were suggested by Xu and Chen (2000) and Xu et al., (1998) for modelling natural convection indoor air flows. As the default value given in the programme is 60, the switching criterion 100 was selected instead of 80 for this study.

In general, it can be seen from the Figure 4-38 that both shear-driven model and buoyancy-driven model present satisfactory results with criterion value 100 and 60 respectively; however, it can be seen that the shear-driven model performs better in the cases with weaker buoyancy forces (lower heat source rate, Model hhf19) and smaller volume flow rate (smaller effective opening area, Model Hf19) as shown in Figure 4-38 and Figure 4-39. For the cases with stronger buoyancy forces and larger effective opening area, the buoyancy-driven model presents more accurate predictive results than shear-driven model as shown in Figure 4-40. Hence, this study employs shear-driven model for cases with lower volume flow rate (small opening area), and employs buoyancy-driven model otherwise.

The two-layer turbulence model selected for each modelling case is summarised in Table 4-15. It can be seen from the table that apart from model Hf19, the buoyancy-driven model was employed to simulate the cases with high heat source rate (2.4kW) and high volume flow rate cases. The shear-driven model was employed to simulate cases with low volume flow rate such as Model hhf30 (lower heat source rate), Model Hf19 and hhf19 (smaller effective openings).

Table 4-15: Summary of turbulence models selected for each case.

Model	**Turbulence Length Scale Model**	
	Buoyancy-driven	Shear-driven
Hf64	X	
hhf64	X	
Hf50	X	
hhf50	X	
Hf30	X	
hhf30		X
Hf19		X
hhf19		X

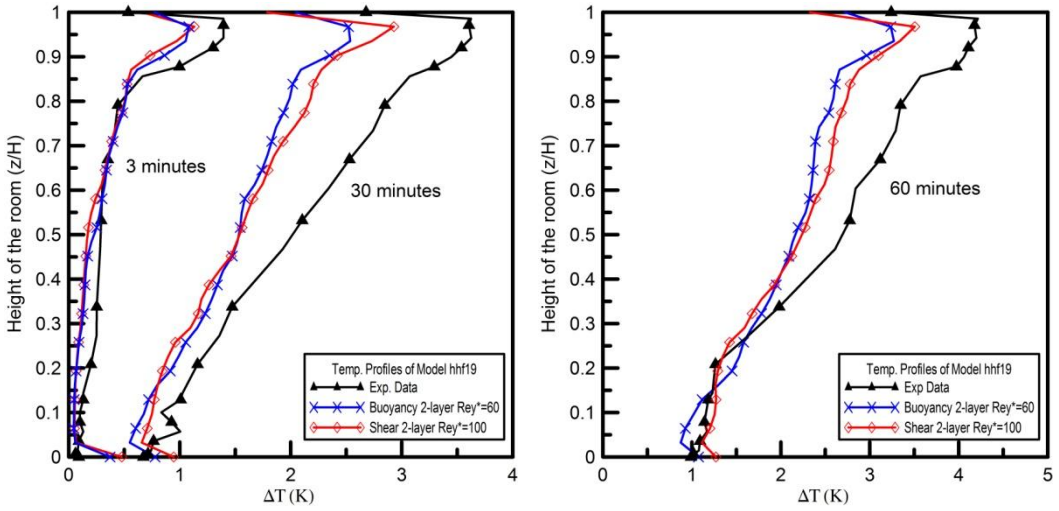

(a) (b)

Figure 4-38: Simulation results of Model hhf19 using buoyancy-driven and shear-driven turbulence length scale model at real-time (a) 3 and 30 minutes and (b) 60 minutes.

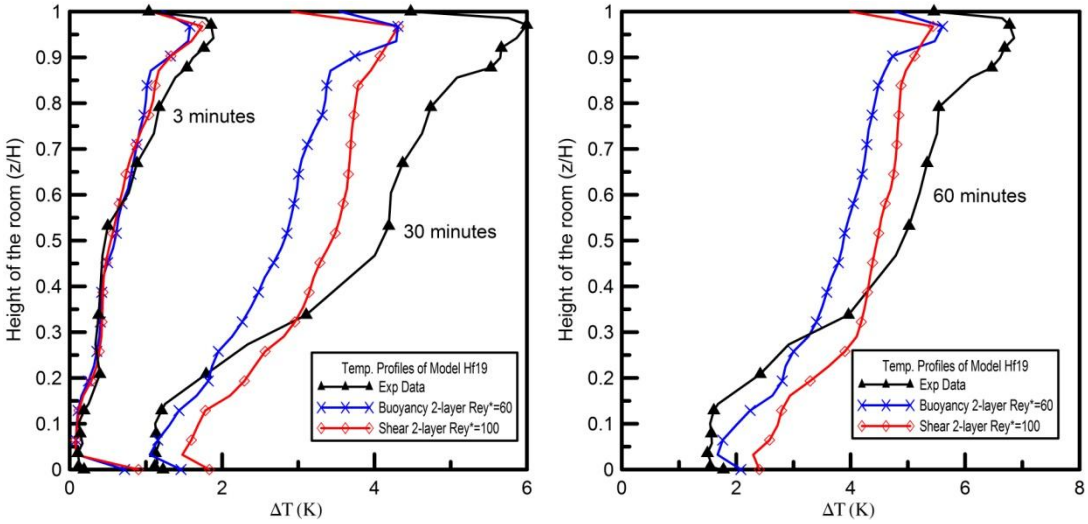

(a) (b)

Figure 4-39: Simulation results of Model Hf19 using buoyancy-driven and shear-driven turbulence length scale model at real-time (a) 3 and 30 minutes and (b) 60 minutes.

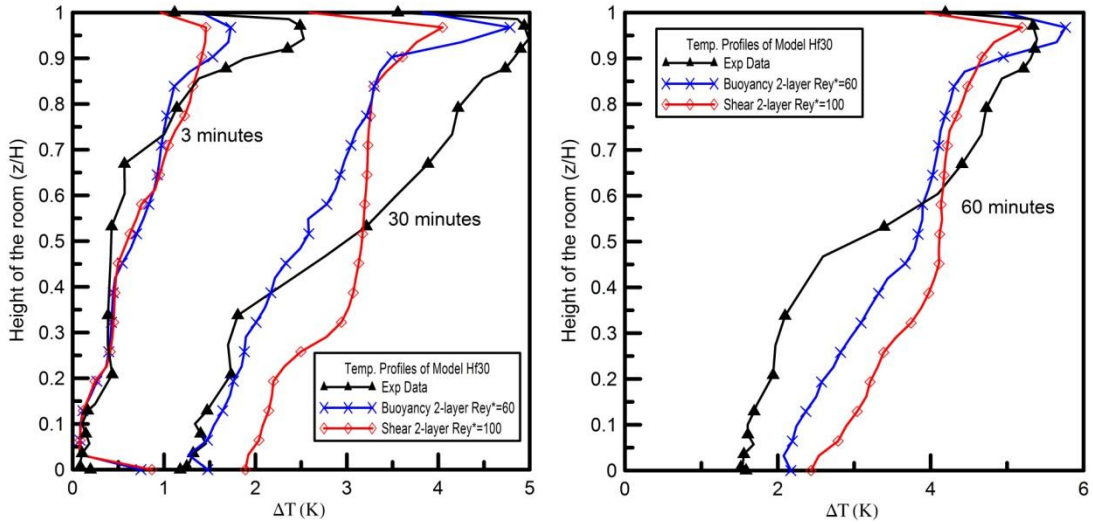

Figure 4-40: Simulation results of Model Hf30 using buoyancy-driven and shear-driven turbulence length scale model at real-time (a) 3 and 30 minutes and (b) 60 minutes.

4.8 Summary of ventilation flow modelling

The previous sections have detailed all the information needed for conducting simulations such as boundary conditions, heat transfer coefficients, absorption coefficients, and time-step. A flow chart is presented in this section to summarise the displacement ventilation flow modelling procedure (see Figure 4-41).

The first step in the procedure is to create the computation domain and each was created to replicate the dimension of experimental set-ups. There are four geometries in total and each was constructed with effective opening area a*=0.064, 0.05, 0.03, and 0.019 respectively. These four geometries were then used to simulate the buoyancy-driven ventilation flows with given conditions.

Once the computational domain was created, the second step is to specified the boundary conditions to the model. These include the heat rate at the centre of the floor, the heat conduction coefficient, heat convective coefficient and radiative properties at each boundary. The boundary conditions were all specified to match closely to the conditions of experiment cases.

The third step in the procedure is to determine the initial condition of the model. This includes the initial air temperature and the ambient air temperature (reference temperature). The air temperatures were obtained from the weather report on the dates when the experiments were conducted.

The weather conditions provided by the report were then used to compute the correspondent absorption coefficient on the date. The mean temperature and the averaged relative humidity were obtained from the weather report to determine the partial pressure of water vapour. Together with the partial pressure of carbon dioxide, the pathlength, and the heat source temperature, the absorption coefficient can be calculated (see Figure 4-21).

The fifth step is to create volume mesh for the domain. The polyhedral mesh was use to generate the mesh as it provide accurate solution when modelling turbulent flows as discussed in Section 4.3. The chamber is generated with coarsest meshes to minimise the amount of mesh created as the turbulent flows inside the test room is of interest. The fine mesh was created at the upper part and lower part of the test room where the turbulent flows are significant. Once the volume mesh is generated, the size of the time step can then be determined by applying Eq. (4-2).

From Table 4-15, buoyancy-driven two-layer turbulence model was selected for high heat load and volume flow rate cases; shear-driven two-layer turbulence model was employed for low heat load and volume flow rate cases. If solutions are stable and converged then a test for mesh independence should be conducted to examine accuracy. If the solution is sensitive to the volume mesh generated, then the process is return back to the mesh generation stage.

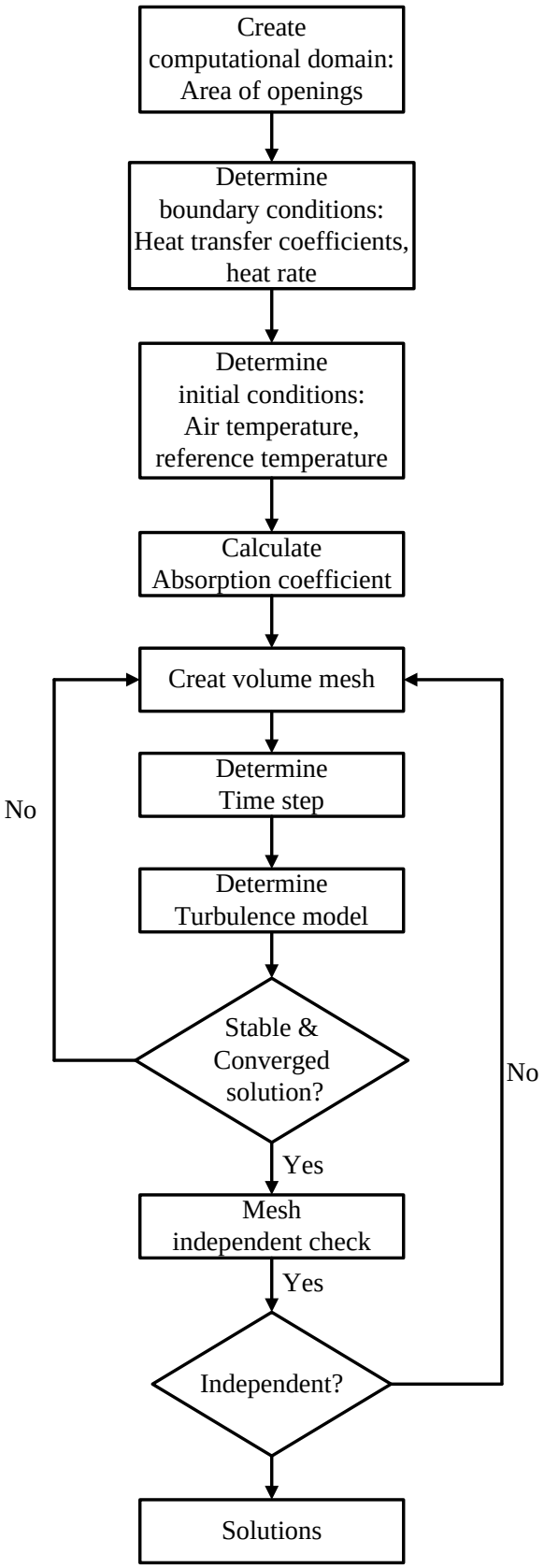

Figure 4-41: Flow chart of modelling procedure for buoyancy-driven displacement ventilation flow.

CHAPTER FIVE

5 Results: The Effects of Absorptivity of the Air to Radiation

5.1 Context

Following the modelling methodology established in the previous chapter, the simulation results of unventilated filling box model and displacement ventilation flow model are presented here. The results were compared with the numerical model and experimental measurements from the early studies for analysis.

5.2 Filling box model

The simulations of the filling box model conducted in this study was a room measuring 3 m high by 7 m wide by 5.6 m deep with a heat source rate 0.785kW located in the centre of the room. A line probe was placed in between the sidewall and the heat source for measuring temperature profile. The boundary walls of the test room were assumed to be adiabatic and the radiation heat transfer between the walls was neglected.

The simulation runs for a real time of 20, 80, 180, 300, 600 and 1800 seconds with time-steps of 1 second. It can be seen from the Figure 5-2 that the buoyancy force generated by the heat source induces the flow to rise up towards the ceiling surface; it then begins to spread out to form a layer of light fluid as the plume reaches the ceiling of the confined region (see Figure 5-2 (t=20s)). With the newly generated plume coming up to the ceiling surface and spreading out, it begins to push the existing fluid layer downward. A stratified layer is then formed with an interface separates the light fluid layer and the unmodified fluid region which is also known as first front (see Figure 5-2 (t=180s) (t=300s))

A time-dependent mathematical model for modelling the density field above the first front of a filling box model was employed in this section for verifying the simulation results.

The comparison of the results is shown in Figure 5-1. The normalised density profiles are plotted against the height of the room, and the magnitude of the density is in inverse relation to the height of the room. The density is at its lowest at the top of the room, and gradually increases towards the floor level of the room. It can also be seen from Figure 5-1 that the plume-affected region widens along with the time, which is the same as the temperature scalar scenes shown. The results from the simulation and the approximate expression have matched favourably well.

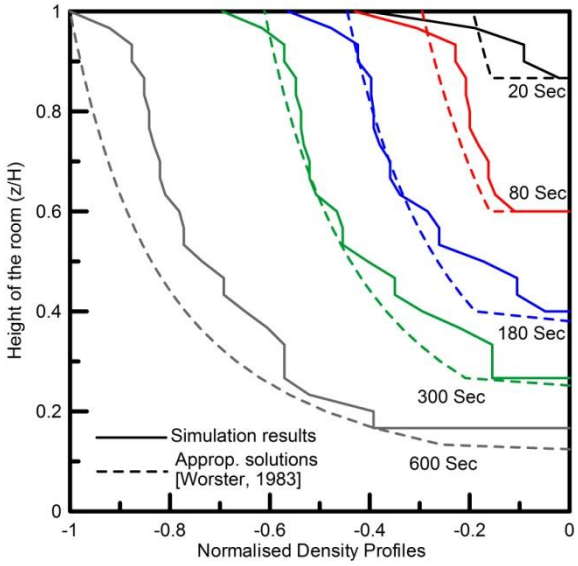

Figure 5-1: The comparison between simulated and approximate density profiles above interface.

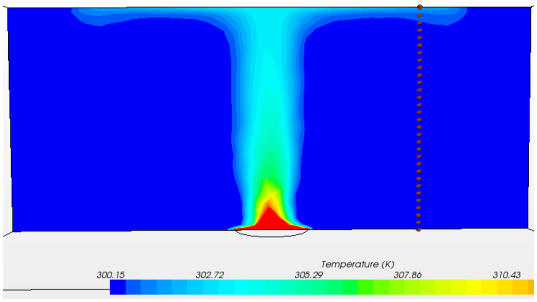

(a) t=20s

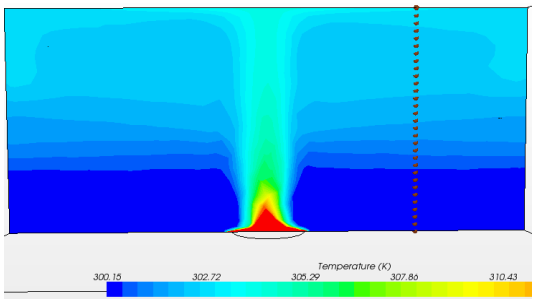

(d) t=300s

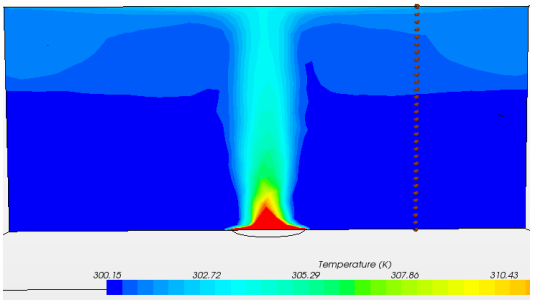

(b) t=80s

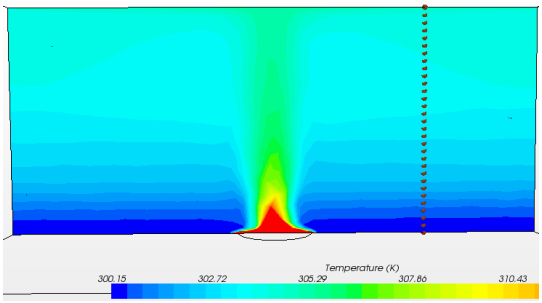

(e) t=600s

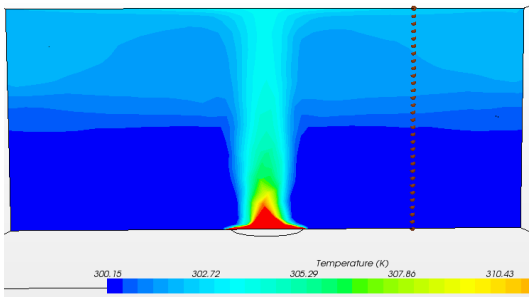

(c) t=180s

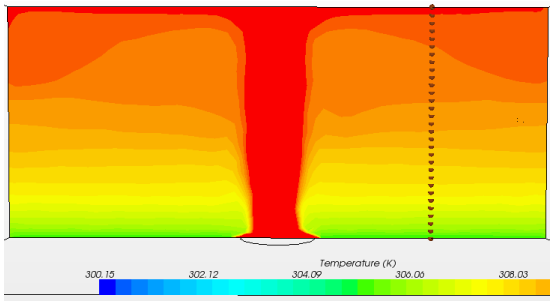

(f) t=1800s

Figure 5-2: The temperature scalar scenes of filling box models at real-time (a) t=20s, (b) t=80s, (c) t=180s, (d) t=300s, (e) t=600s, (f) 1800s.

It can be seen from the figures above that the plume is lazy. A lazy plume is considered a plume that arises from a real source at z=0 with lower momentum then the plume that rises from virtual point source (Taub et al., 2015). A dimensionless parameter, Γ, is used to classified the type of the plume. For a pure plume Γ=1, when Γ>1 the plume is classified as a lazy plume.

$$\Gamma(z=0) = \frac{5F_0 \cdot (Q_0)^2}{4c_0 \cdot (M_0)^{5/2}}, \tag{5-1}$$

where F_0, Q_0, and M_0 are buoyancy flux, volume flux and momentum flux at the source z=0, c_0 is the entrainment constant. This implies that the similarity solution can not be used for the case of lazy plume. However, Morton (1959) has shown that the lazy plume in the far-field away from the real source is approximately equivalent to the plume coming from point source located below (or above) the real source (see Figure 5-3).

Hence, as long as only the plume in the far-field region is of interest, it is possible to consider the lazy plume to be equivalent to a pure plume originating from a point source of buoyancy located at some virtual origin.

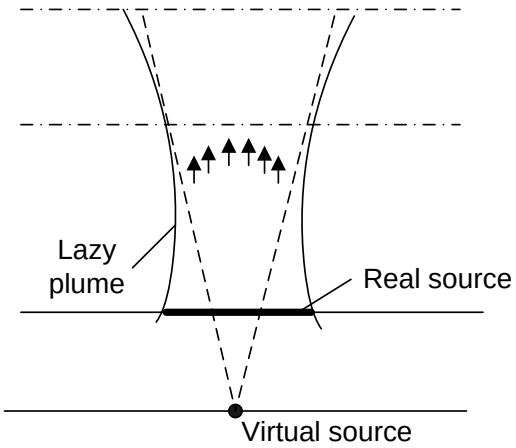

Figure 5-3: Schematic of the equivalent parts of lazy plume and pure plume.

5.3 Displacement ventilation model

The displacement ventilation models were created based on the conditions of experiment set-up built by Sandbach and Lane-Serff (2011b) by using commercial programme StarCCM+. Four models were created with four different effective opening areas respectively and each was given a heat source rate of 2.4kW and 1.25 kW respectively (see Table 4-2 and Table 4-3). The boundary conditions, initial conditions and modelling methods are detailed in Chapter 4. The absorption coefficient of each model was determined based on the conditions listed in Table 4-7. The turbulence model selected for modelling was realizable k-ε two-layer turbulence model as mentioned in Section 4.7. The predicted results were then verified with the experimental data and also compared with the numerical results from the mathematical model developed by Sandbach and Lane-Serff (2011b).

5.3.1 Temperature profiles

The simulation results of model Hf64/hhf64, Hf50/hhf50, Hf30/hhf30, Hf19/hhf19 at real-time 3 minutes, 30 minutes and 60 minutes respectively are presented in Figure 5-5 to Figure 5-11. The results were compared with the experimental data and the numerical solutions. It can be seen from the following figures that the simulation results are generally shown to match well with the experimental data. The results suggest that by taking the radiative absorptivity of the air into account, the error between the simulation results and the experimental data has significantly reduced in comparison to the error between the data and numerical solutions, especially in the lower half of the temperature profiles.

It can be seen from the Figure 5-4 and Figure 5-5 of model Hf64 and hhf64 that the simulation results are shown to agree reasonably well with the experimental results. The prediction of the temperature profiles along the room height and the position of the stratification layer interface were predicted satisfactory.

Although the simulation results at 30 minutes are less accurate in general then those results at 3 and 60 minutes, the error is generally less than 23%. The cause of this deficit is perhaps to do with the location of the measuring points. The measuring points could be affected by the heat diffusing from the plume or heat sources before the test room reaches thermal steady state (Davidson, 1989). In addition, the deficit can be largely to do with the temperature of the incoming air from the laboratory which increases over the duration of experiment. The ambient temperature recorded over the duration of the experiment is shown to have a relatively large gradient at the beginning of the experiment and hence a slightly large discrepancy at real-time 30 minutes (Sandbach, 2009).

By comparing the simulation results with the numerical data obtained by Sandbach (2009), it can be seen from the figures that there is a reasonably good fit at the upper half of the temperature profiles of all cases, but a relatively large deficit at the lower half. This is possibly to do with the fact that the temperature of the airflow coming through lower openings of the room gradually increases with time. In addition, the numerical result shows a sharp interface between the upper and lower layer, whereas the interfaces in the simulation results are mostly diffuse and not clear. This is perhaps to do with the thermal energy transfer from the descending warm air (cooled by the wall) in the upper part of the room towards interface. The heat transferred to the interface causing a diffuse interface.

Model of Hf64 and hhf64:

Effective opening a*=0.064; Heat source rate 2.4 and 1.25 kW respectively.

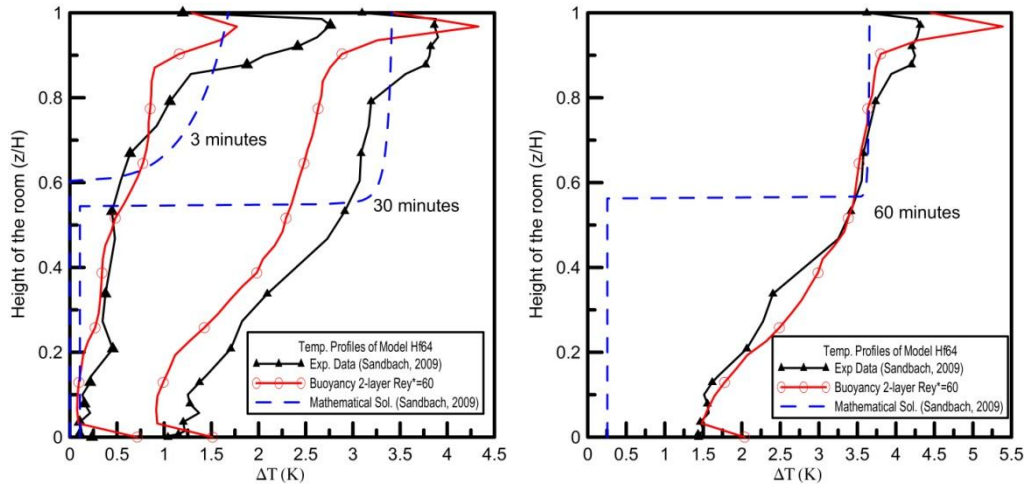

(a) (b)

Figure 5-4: The comparison of simulation results of Model Hf64 with experimental data (Sandbach, 2009) and mathematical modelling results (Sandbach, 2009) at real-time (a) 3 minutes, 30 minutes, and (b) 60 minutes.

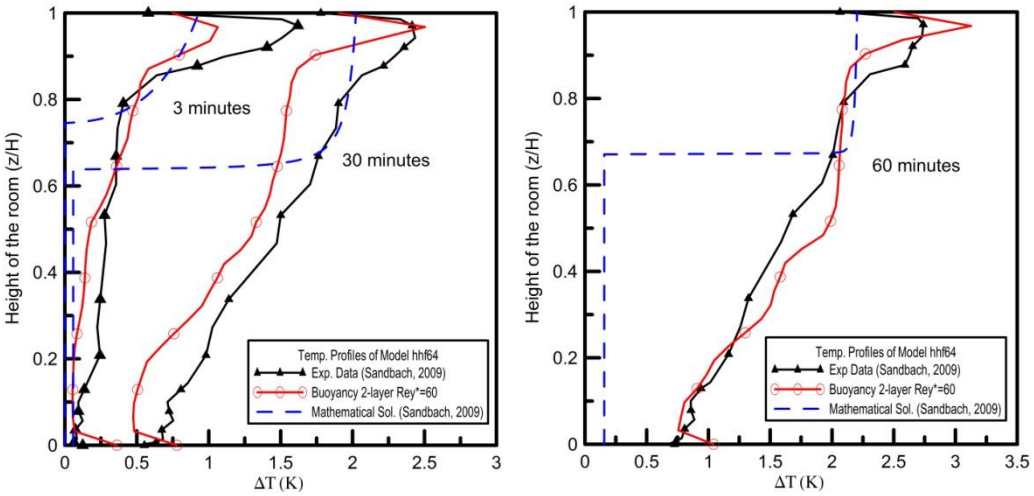

(a) (b)

Figure 5-5: The comparison of simulation results of Model hhf64 with experimental data (Sandbach, 2009) and mathematical modelling results (Sandbach, 2009) at real-time (a) 3 minutes, 30 minutes, and (b) 60 minutes.

Model of Hf50 and hhf50:

Effective opening a*=0.050; Heat source rate 2.4 and 1.25 kW respectively.

This model closes one opening on the ceiling, UO-2. The predicted results agree reasonably well with the measurements as can be seen from Figure 5-6 and Figure 5-7. It can also be noticed that the deficit at real-time 30 minutes of model hhf50 is smaller than the one with larger heat source in Figure 5-6. This is perhaps due to the measuring points were less affected by the heat diffusion as mentioned earlier.

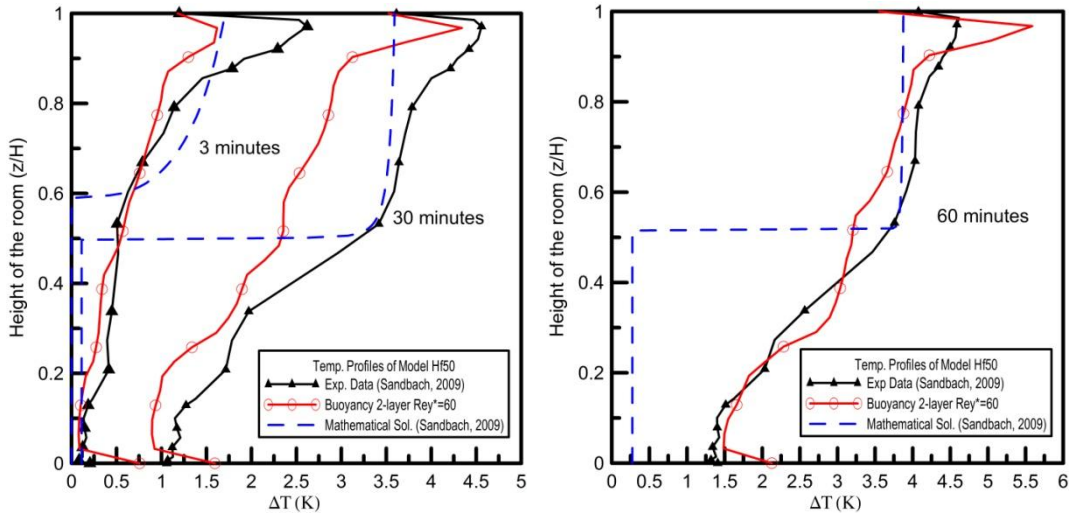

(a) (b)

Figure 5-6: The comparison of simulation results of Model Hf50 with experimental data (Sandbach, 2009) and mathematical modelling results (Sandbach, 2009) at real-time (a) 3 minutes, 30 minutes, and (b) 60 minutes.

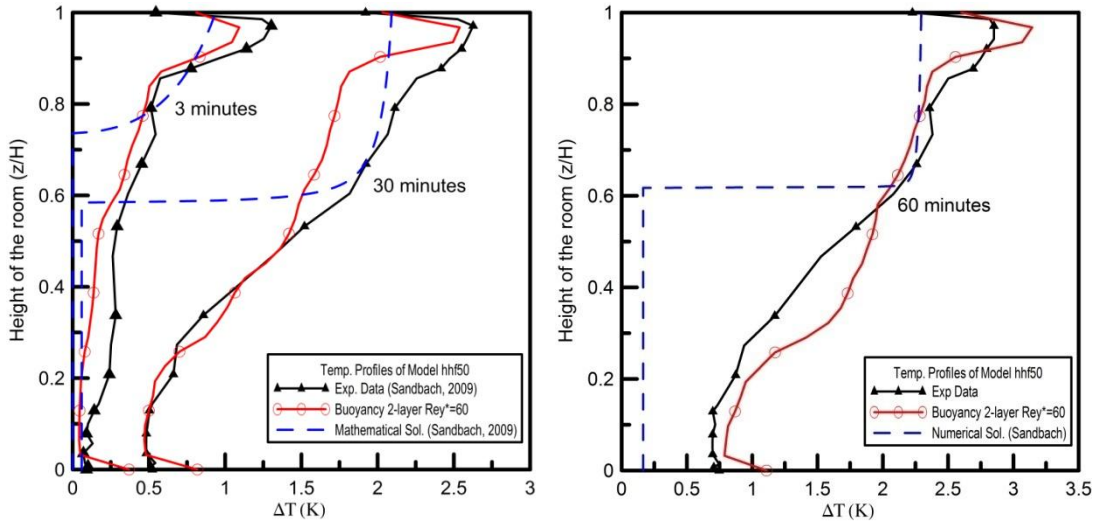

(a) (b)

Figure 5-7: The comparison of simulation results of Model hhf50 with experimental data (Sandbach, 2009) and mathematical modelling results (Sandbach, 2009) at real-time (a) 3 minutes, 30 minutes, and (b) 60 minutes.

Model of Hf30 and hhf30:

Effective opening a*=0.030; Heat source rate 2.4 and 1.25 kW respectively.

With the opening area reduced further by closing off opening LO-2 at lower level, the ventilation flow rate was further decreased. Hence, the model hhf30 with small heat source power was modelled by the Wolfshtein shear-driven turbulence model instead. The results are also shown to have a satisfactory agreement with the experimental data.

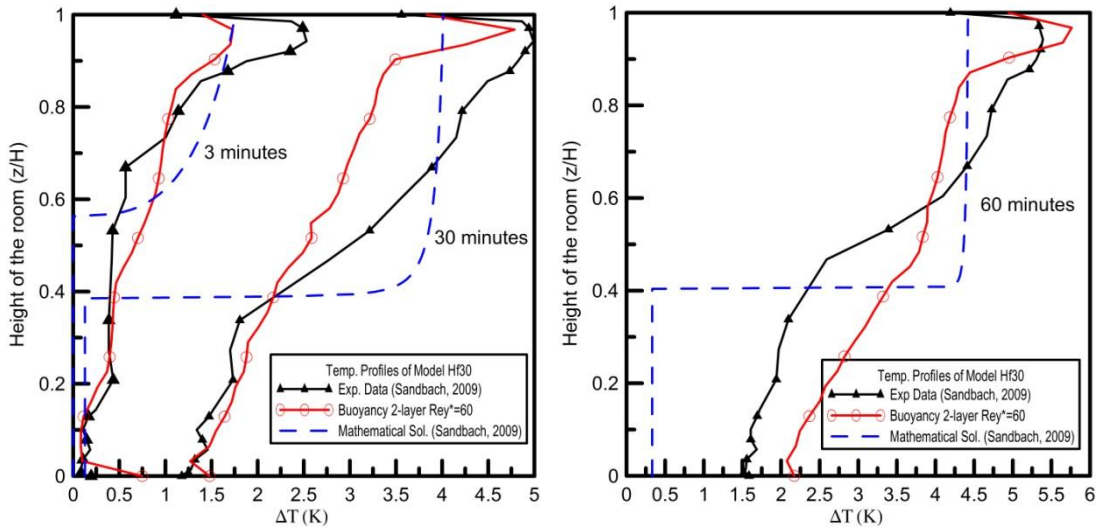

(a) (b)

Figure 5-8: The comparison of simulation results of Model Hf30 with experimental data (Sandbach, 2009) and mathematical modelling results (Sandbach, 2009) at real-time (a) 3 minutes, 30 minutes, and (b) 60 minutes.

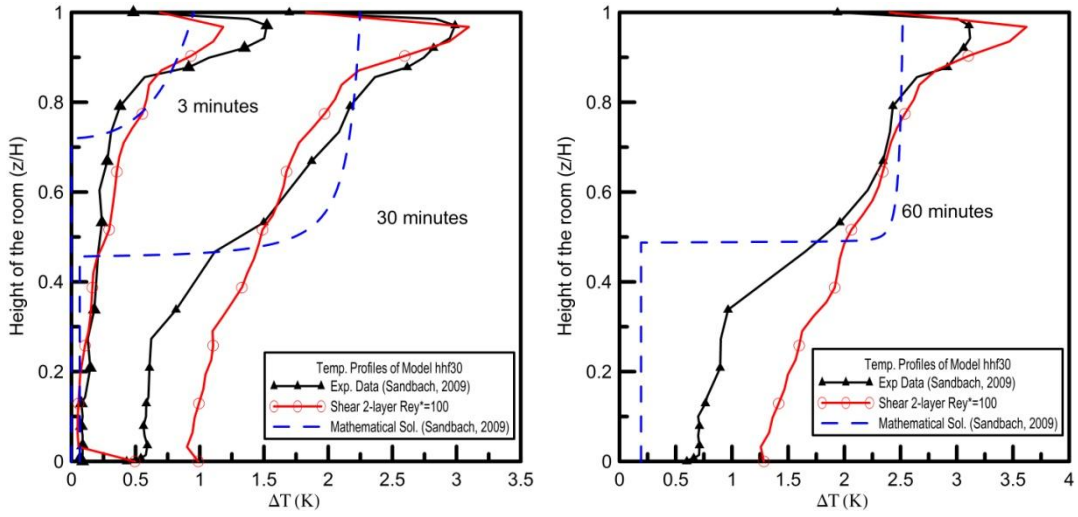

(a) (b)

Figure 5-9: The comparison of simulation results of Model hhf30 with experimental data (Sandbach, 2009) and mathematical modelling results (Sandbach, 2009) at real-time (a) 3 minutes, 30 minutes, and (b) 60 minutes.

Model of Hf19 and hhf19:

Effective opening a*=0.019; Heat source rate 2.4 and 1.25 kW respectively.

The shear-driven turbulence model performs generally well for the models with small ventilation flow rate. Although the discrepancy is relatively large than in previous models, the simulation results shown in the following figures agree reasonably well with the experimental data. The cause of the discrepancy is perhaps to do with the models with small ventilation flow rate are sensitive to radiative absorptivity.

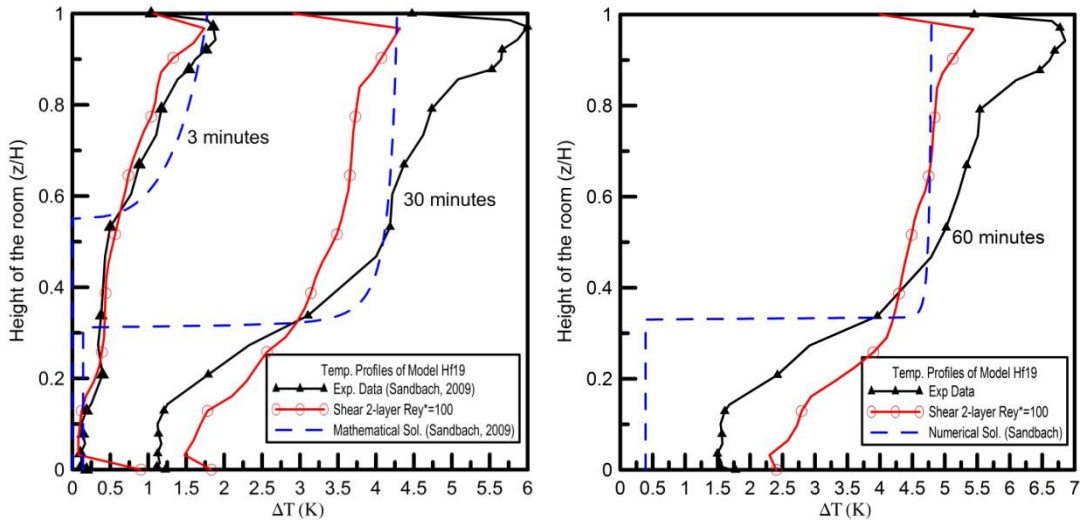

(a) (b)

Figure 5-10: The comparison of simulation results of Model Hf19 with experimental data (Sandbach, 2009) and mathematical modelling results (Sandbach, 2009) at real-time (a) 3 minutes, 30 minutes, and (b) 60 minutes.

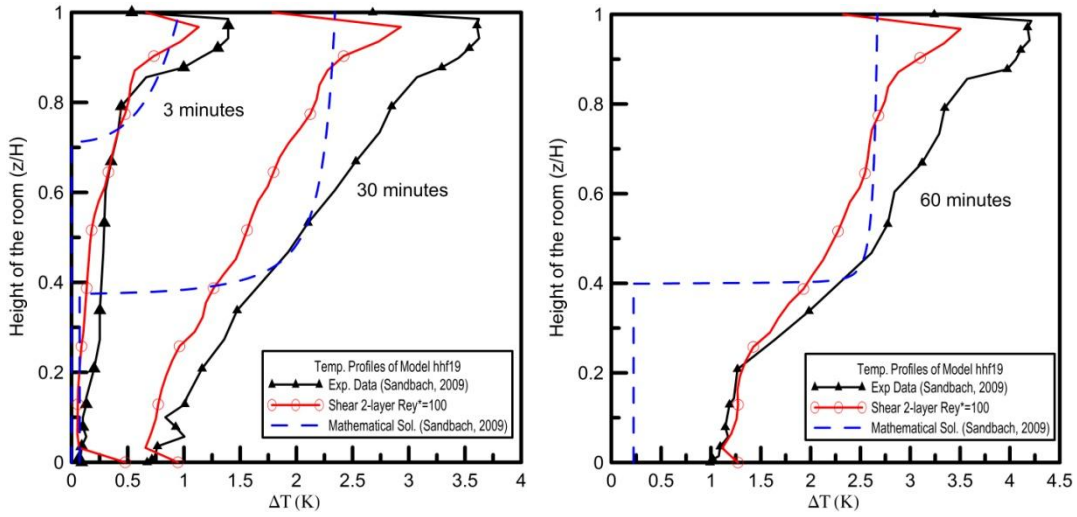

(a) (b)

Figure 5-11: The comparison of simulation results of Model hhf19 with experimental data (Sandbach, 2009) and mathematical modelling results (Sandbach, 2009) at real-time (a) 3 minutes, 30 minutes, and (b) 60 minutes.

5.3.2 Volume flow rate through openings

The predicted volume flow rate of each case through openings is also compared with the experimental measurements. It can be seen from the Figure 5-12 and Figure 5-13 that the predicted results in most cases have reasonably good match with the measurements. Although there is a discernible discrepancy in the case of Hf64 and hhf64 respectively, the error between the measurements and the predictive results is less then 23%.

The cause of the differences between the predicted results and the experimental data is perhaps to do with the predicted vertical temperature distributions. Temperature difference is the driving force of the airflow in the naturally ventilated space; a under-predicted vertical temperature distribution can result in a under-predicted air flow rate. As can be seen from the simulation results that the temperature profiles were mostly under-predicted, there are deficits between the measurements and the predicted volume flow rates.

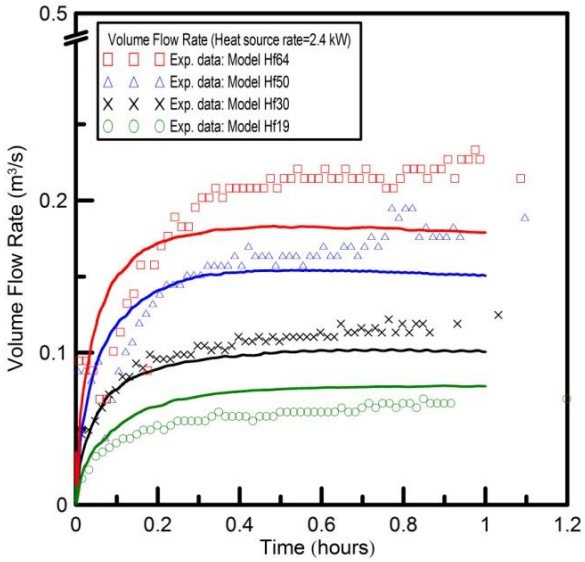

Figure 5-12: The comparison of volume flow rates at heat source rate 2.4 kW.

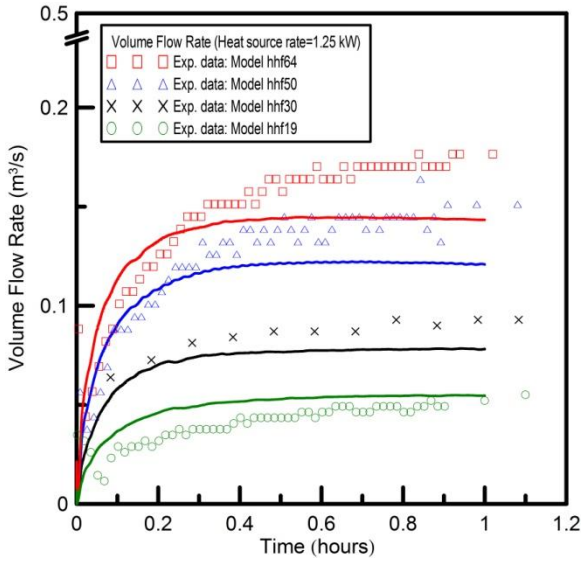

Figure 5-13: The comparison of volume flow rates at heat source rate 1.25 kW.

5.4 The effects of radiative absorptivity

For most of the ventilation flow studies, the radiative heat transfer inside the space was only considered from surface to surface, the working fluid in between the surfaces such as air was often considered as a medium that transparent to the thermal radiation. In fact, the medium which contains radiative participants can absorb and emit radiation. This section shows the influence of a non-transparent medium to the thermal distribution in the ventilated space.

5.4.1 Surface to surface radiation model (neglect absorptivity)

In order to compare the influences of the radiative absorptivity of the air on thermal distribution, two radiation models: surface to surface radiation model and participating media radiation model were used for simulations. Model Hf64 and hhf64 were both selected for study in this section.

For surface to surface model, the thermal distribution is mainly affected by growing thickness of the thermal stratification layer. There is a clear interface in between the modified and unmodified region at the early stage of the simulations as shown in Figure 5-14. Until the stratification layer start to descend, the lower half unmodified region stay un-affected.

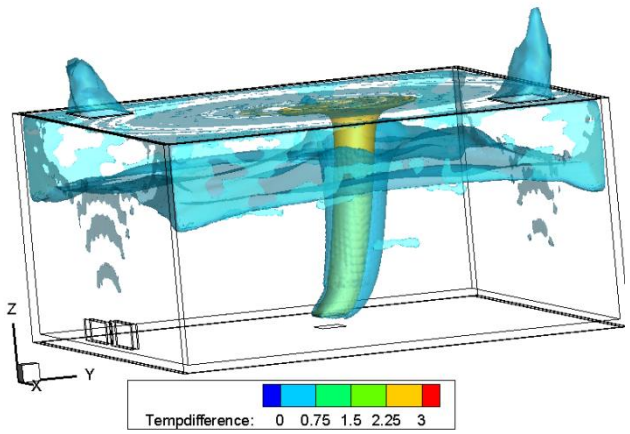

Figure 5-14: The iso-surfaces in temperature differences of S2S radiation model.

For participating radiation model, on the other hand, the stratification layer grows quicker and the thermal distribution in the lower half region is already affected due to the radiative absorptivity of the medium at the early stage of the simulations as can be seen in Figure 5-15 below.

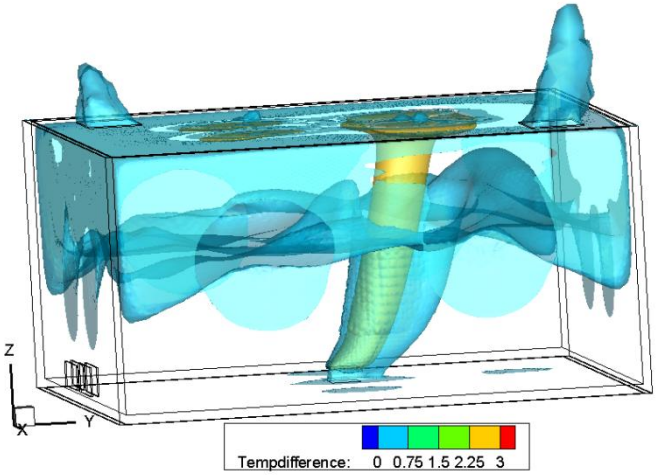

Figure 5-15: The iso-surfaces in temperature differences of participating radiation model.

Comparing simulation results with mathematical solutions from (Sandbach and Lane-Serff, 2011b). It can be seen from the Figure 5-16 and Figure 5-17 that there are clear deficits between the experimental data and the solutions from surface to surface radiation model. The temperature profiles were under-estimated when the radiative absorptivity was ignored. This phenomenon is especially clear in the lower half at real-time 3 and 30 minutes. And at real-time 3 minutes, the solutions are seen to have a good match with the mathematical solutions which also neglects the radiative absorptivity.

The agreement with the numerical solutions becomes poor when time increases as can be seen in Figure 5-18 at real-time 60 minutes. This is because the heat transfer at the side walls were neglected and the convective heat transfer from the descending warm air was not considered in the numerical model.

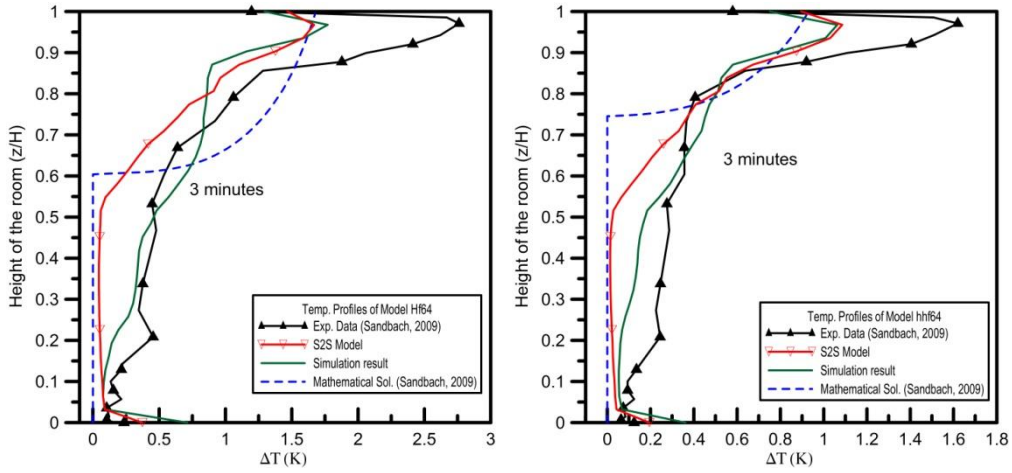

(a) (b)

Figure 5-16: Without considering the absorptivity, the surface to surface model agrees well with the mathematical solutions. The simulation considering absorptivity agrees well with the measurements in the cases of (a) Model Hf64 and (b) Model hhf64 at real-time 3 minutes.

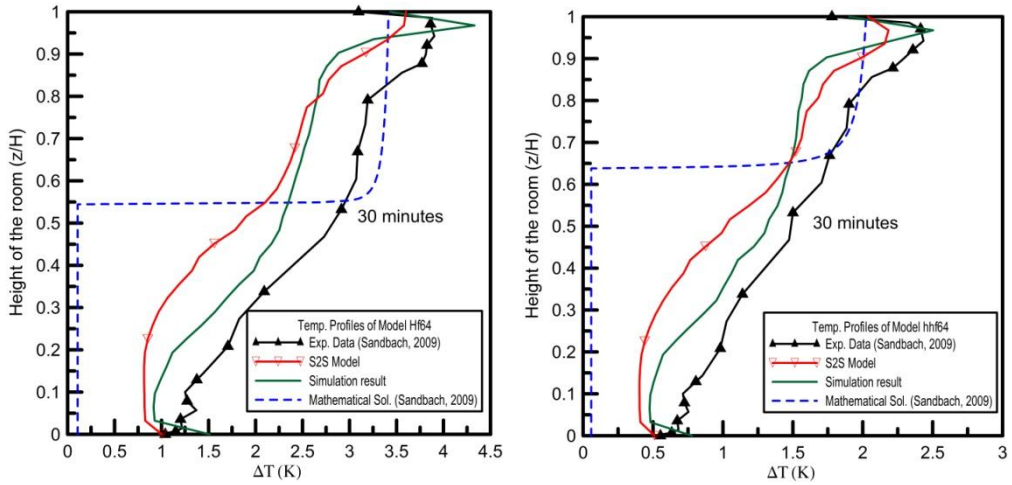

(a) (b)

Figure 5-17: The simulation results considering absorptivity and without are compared with the mathematical solutions in the cases of (a) Model Hf64 and (b) Model hhf64 at real-time 30 minutes.

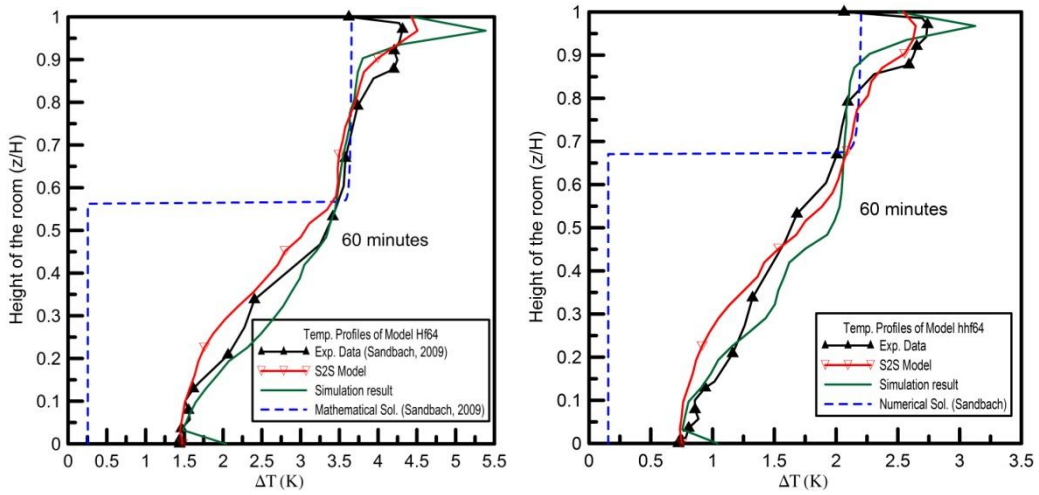

(a) (b)

Figure 5-18: The simulation results considering absorptivity and without are compared with the mathematical solutions in the cases of (a) Model Hf64 and (b) Model hhf64 at real-time 60 minutes.

5.4.2 The participating radiation model (consider absorptivity)

Based on the discussion above, it is certain that the absorptivity of the air can affect the thermal distribution inside the ventilated space. This section discusses further the effects of the intensity of radiative absorptivity on the thermal distribution by assigning different absorption coefficient to the models. The cases selected for modelling were model Hf64, Hf30 and Hf19 which the heat source rate were at 2.4 kW and the openings were fully, half opened, and closed to the smallest size respectively. All three cases were assigned three absorption coefficients: 0.01, 0.1, and 0.17 which were cited from the early studies mentioned in Section 2.7. The results from each absorption coefficients were compared with the simulation results from Section 5.3.1.

It can be seen from the results (model Hf64) that the absorption coefficient can affect the thermal distribution inside the ventilated space (as shown in Figure 5-19). The scale of the influence depends on the coefficients. It can be seen that the larger the absorption coefficient the greater the temperature differences it develops. The results in the figures also show that by employing the absorption coefficients cited from the early studies, the predictive temperature profiles were either under or over estimated in comparison to the simulation results presented in section 5.3.1.

Hence, it is clear to see that the absorption coefficient should be determined according to the conditions of each model instead of giving a one-and-for-all value; otherwise it could lead to inaccurate predictive results.

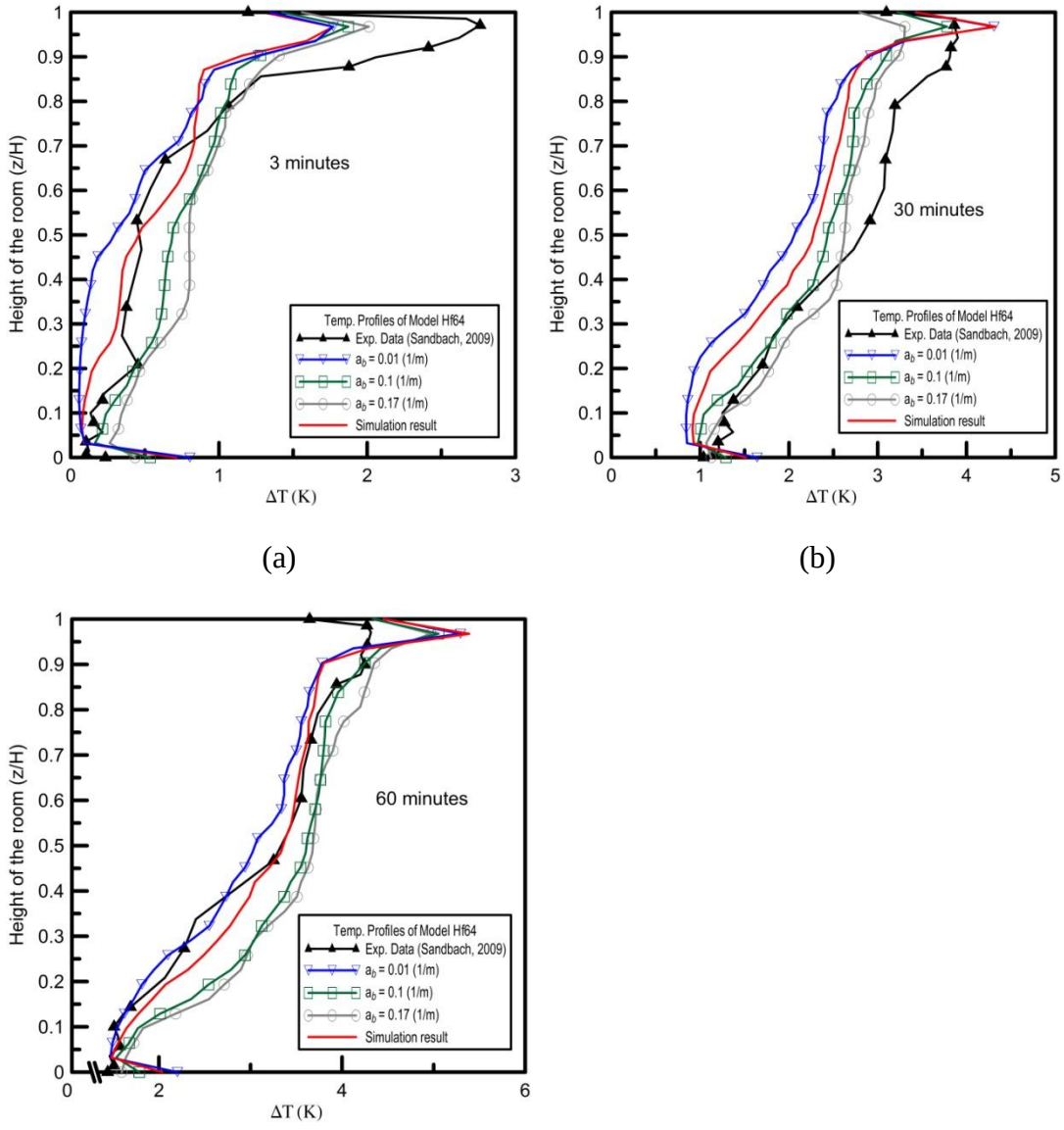

Figure 5-19: The magnitude of radiative absorptivity effects on thermal distribution in the cases of Model Hf64 at real-time (a) 3 minutes, (b) 30 minutes, and (c) 60 minutes.

In the cases of Model Hf30 and Hf19, the effects of absorptivity is observed to relatively significant in the case of Model Hf19 then Model Hf30 at early stage. This is perhaps to do with the airflow rate. The thermal energy of the airflow reacts quicker with less airflow rate (as shown in Figure 5-20). In real-time 30 and 60 minutes, the differences between vertical temperature profiles reduced as shown in Figure 5-21 and Figure 5-22.

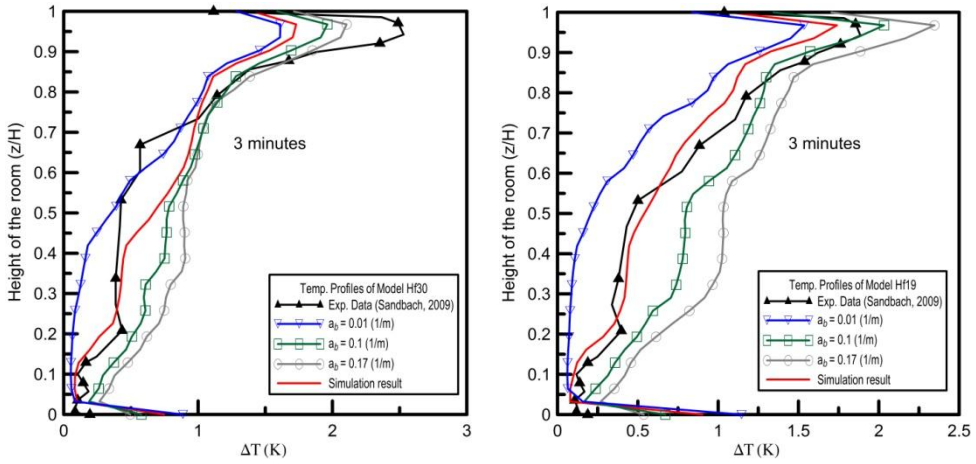

(a) (b)

Figure 5-20: The magnitude of radiative absorptivity effects on thermal distribution in the cases of (a) Hf30 and (b) Hf19 at real-time 3 minutes.

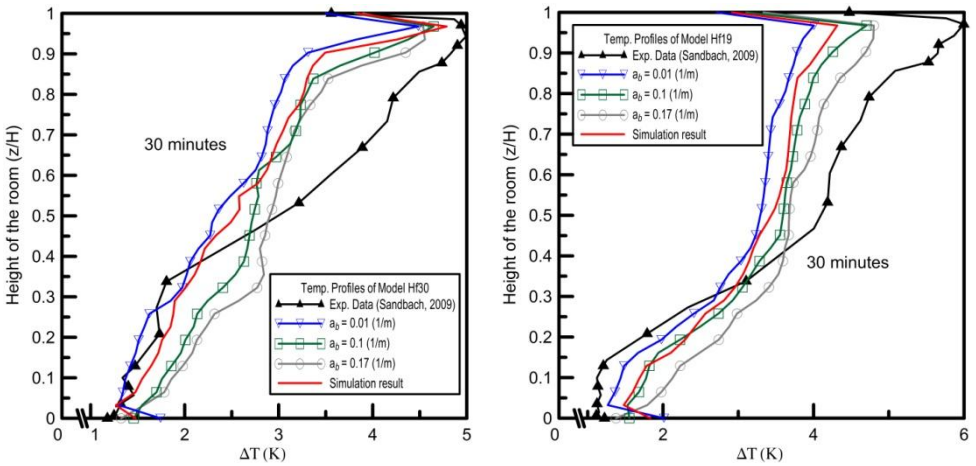

(a) (b)

Figure 5-21: The magnitude of radiative absorptivity effects on thermal distribution in the cases of (a) Hf30 and (b) Hf19 at real-time 30 minutes.

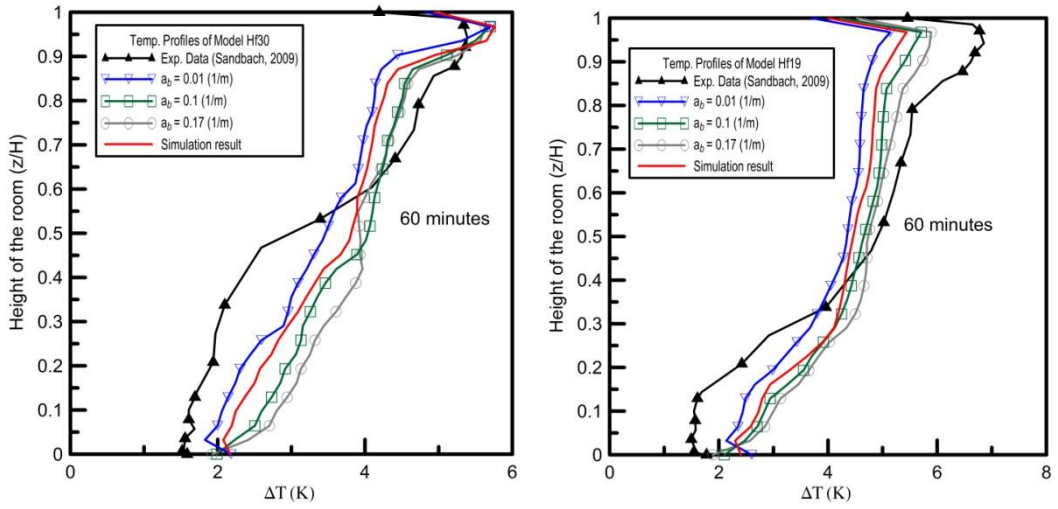

(a) (b)

Figure 5-22: The magnitude of radiative absorptivity effects on thermal distribution in the cases of (a) Hf30 and (b) Hf19 at real-time 60 minutes.

5.4.3 The influence of absorptivity on the strength of stratification

The absorption coefficient can not only have influence on the vertical temperature distribution, but also the formation of the stratification layer. It was found in an early study that a larger absorption coefficient tends to reduce the strength of the stratified layer (Chow and Holdo, 2010). This was also observed in this study from fully opened openings case, Model Hf64.

The strength of the stratification layer can also be expressed by Richardson number (R_i) which is the ratio of the buoyancy term to the flow gradient term. It is also sometime regarded as an indicator of the stability of stratification; which is defined as:

$$R_i = -\frac{g}{\rho}\frac{d\rho}{dy} \Big/ \left(\frac{\partial u}{\partial y}\right)^2, \qquad (5\text{-}2)$$

where ρ is density, u is velocity. It can be seen that the Richardson number and the temperature difference across the stratification layer decreases with high radiative absorptivity and weaken the interface next to the ceiling surface in the room (see Table 5-1).

Table 5-1: The influence of absorptivity on the strength of the stratification (Hf64)

Model Hf64			
Absorption coefficients (m^{-1})	ΔT	Density gradient across interface	R_i
a_b=0.01	1.21	0.011	6.33
a_b=0.035 (Sim.)	0.97	0.009	2.52
a_b=0.1	0.76	0.007	0.73
a_b=0.17	0.67	0.006	0.09

However, unlike the Model Hf64, this study found that the stability of the stratification layer is less affected by the strength of the radiative absorptivity in those models with smaller size of openings. This indicates that a steep temperature gradient remains at the upper half of the space despite an increasing absorption coefficient.

From the Table 5-2 and Table 5-3 below, it is evident that the temperature and density gradients are less affected and do not develop into linear vertical profiles along with larger absorption coefficients. The Richardson number of both model Hf30 and Hf19 are, however, still shown to have smaller values at large absorption coefficient; this is because the velocity of air flow increases with absorptivity.

Table 5-2: The influence of absorptivity on the strength of the stratification (Hf30)

Model Hf30			
Absorption coefficients (m^{-1})	ΔT	Density gradient across interface	R_i
a_b=0.01	1.46	0.014	14.02
a_b=0.044 (Sim.)	1.67	0.016	15.44
a_b=0.1	1.63	0.0158	1.63
a_b=0.17	1.63	0.0157	1.21

Table 5-3: The influence of absorptivity on the strength of the stratification (Hf19)

Model Hf19			
Absorption coefficients (m^{-1})	ΔT	Density gradient across interface	R_i
a_b=0.01	0.55	0.005	1.58
a_b=0.041 (Sim.)	0.71	0.007	0.97
a_b=0.1	0.84	0.008	0.78
a_b=0.17	1.11	0.01	0.65

For Model Hf64 and Hf30, the temperature differences are not sensitive to absorption-coefficient. This has to do with the magnitude of the mass flow rate. The mass flow rates of all three models in all three absorption coefficients are shown in the Figure 5-23 below. It can be seen from the figures that the magnitude of the mass flow rate is not only affected by the size of the opening area but also affected by the intensity of radiative absorptivity. In each model, the mass flow rate increases along with larger absorption coefficient.

In Model Hf64, it was found that the absorption coefficient has a significant impact on the strength of the stratification formed near to the ceiling. This is not surprising given that the stronger the absorptivity the larger the mass flow rate (see Figure 5-23(c)). The optically thick participating medium absorbs the radiative heat energy emitted from the boundary surfaces. If the gas absorbs the energy of passing radiation, this absorbed heat energy then increases the temperature of the gas. The net rate of radiative heat transfer between the boundary surface and gas can be expressed as:

$$\mathrm{Q_{net}} = A_s \cdot \sigma\left(\varepsilon_\mathrm{g} T_\mathrm{g}^4 - \alpha_\mathrm{g} T_\mathrm{s}^4\right)\frac{\varepsilon_\mathrm{s}+1}{2}, \qquad (5\text{-}3)$$

where A_s is the area of the boundary surface, σ is Stefan-Boltzmann constant, ε_g and ε_s are emissivity of gas and surface respectively, T_g, T_s are temperatures of gas and surface respectively. It can be seen from the equation that the larger the absorption coefficient the greater the gas temperature it becomes. As the gas temperature increases, this enlarges the density deficit of buoyant current and hence the volume

flux through the vents. This can also be seen from the numerical modelling results shown in Figure 5-23.

However, the impact cause by the absorption coefficient was found to be less significant in Model Hf30 and Hf19. This is because the mass flow rates of Model Hf30 and Hf19 are relatively small in comparison to Model Hf64 (see Figure 5-23 (a) and (b)). This causes less effective heat convection between the upper and lower half of the spaces and hence less significant influence of the absorption coefficients to the strength of stratification then the case of Model Hf64.

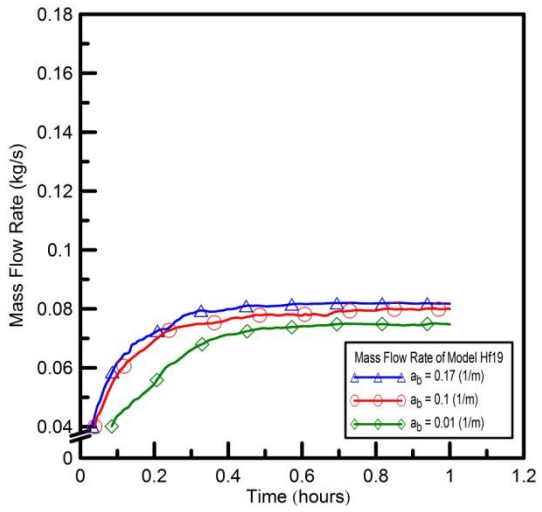

(a)

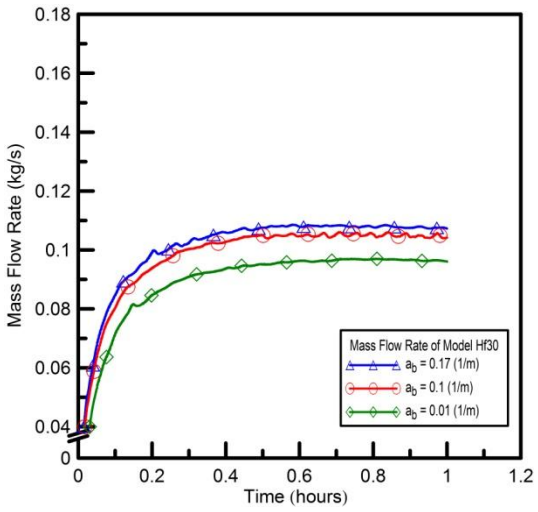

(b)

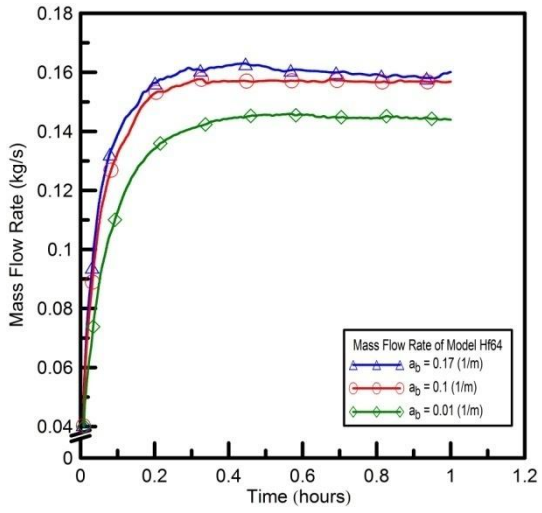

(c)

Figure 5-23: The effect of absorption coefficients to mass flow rates

CHAPTER SIX

6 The Effects of Surface Emissivity on Radiation

6.1 Context

Having studied the effects of radiative absorptivity of the air on the intensity of radiation in an enclosure, the established numerical modelling method is applied here to study the effects of the radiative properties of the boundary surfaces on vertical air temperature distribution in a displacement ventilation flows enclosure. The study is carried out by modelling the experiments conducted by Li et al. (1993b).

In the experiments, the interior wall surfaces of the test room were either painted black or covered with aluminium sheets to investigate the effects of the emissivity of the surfaces on radiation heat transfer. Changes of inlet volume flow rate and power of heat source were also incorporated in the experiments to examine their effects on the vertical temperature distribution in the test room. The numerical modelling results are then compared with the measurements.

6.2 The experiments

A full-scale experiment of displacement ventilation flows was conducted in a laboratory in Sweden as detailed in Li et al. (1993b). The experiment has a test room 4.2 m wide, 3.6 m deep, and 2.75 m high, as shown in Figure 6-1. Two openings were mounted on the front wall (wall 1) and on sidewall (wall 2) respectively. The supply opening on the front wall at floor level has dimensions of 0.5 m x 0.45 m, and 50% of it was made perforated reducing the total inlet area to 0.1125 m^2. The flow leaves the test room through the opening on wall 2 which has dimensions of 0.525 m x 0.22 m. The heat source was placed 2.7 m away from the supplying opening and 0.11 m above the floor and has dimensions of 0.4 m x 0.3 m x 0.3 m. The heat source is made of 24 light bulbs of 25 W which were placed in a uniform cube each

filled with aluminium chips to give uniform distribution of heat and reduce short-wave radiation to the wall surfaces.

The whole test room is placed in a larger enclosure so that the exterior surfaces of the sidewalls (wall 2, wall 3 and wall 4) were surrounded to control their temperatures. Only the exterior surfaces of the ceiling and front wall (wall 1) were not controlled and subjected to the thermal conditions in the laboratory in which the temperature varies by less than 1 ^{0}C during the experiments.

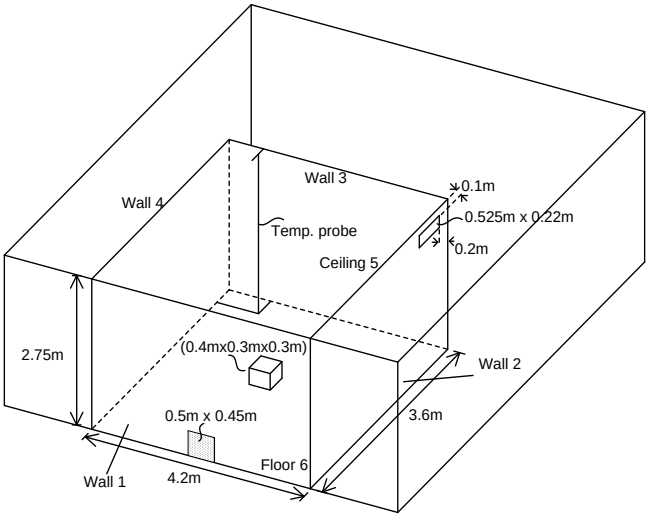

Figure 6-1: The layout of the space where experiment was conducted.

6.3 Computational modelling

The turbulence models and mesh method used for modelling this case are those set out in Chapter 4. The polyhedral mesh is applied to generate meshes for the computational domain; the turbulent flow in the domain is solved by realisable two-layer k-ε model. The computational domain is as shown in Figure 6-2. The thermal distribution and air flow in the larger enclosure is not considered and thus the outer domain can be removed. This is because the function of the large enclosure was to control the temperature of the exterior surfaces of the sidewalls. Therefore, the large enclosure domain can be replaced with constant temperature boundary condition. This can not only save considerable computational effort, but also free from considering the thermal distribution and air circulation in the outer region.

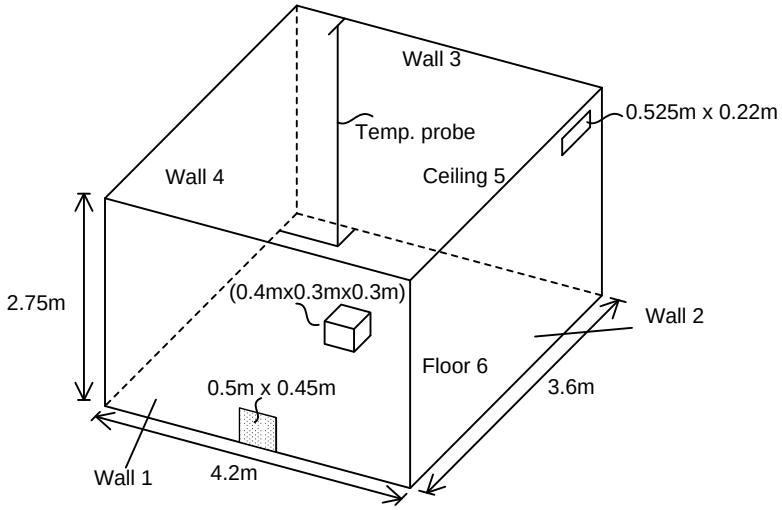

Figure 6-2: The computational domain of the test room.

6.3.1 Computational model

The two-layer k-ε turbulence model employed here consisted of kinetic and dissipation differential equations and an empirical turbulence length scales developed by Xu et al. (1998). They are used to model the flow dissipation rate in different flow regions. In the near-wall region, the dissipation rate was modelled by an algebraic equation and a turbulence length scale. When solving the flows in the outer near-wall region, the dissipation rate was solved by dissipation differential equation. The transition from differential equation to algebraic equation was

controlled by the switching criterion, Re_y^*, in the blending function, Eq. (3-49). In this case, the value was set as Re_y^*=60.

The whole geometry was meshed by the mesh size that is half size of the height of the smallest opening in the test room. The mesh were refined and improved at inlet opening, near ceiling and floor wall boundaries, region right above heat source and outlet opening. A 4 cm prism layer mesh was generated adjacent to the walls to resolve boundary layer flow. Simulations were conducted using meshes of 192,169, 642,587 and 1,243,670 cells for mesh independence check. The solutions of vertical temperature distribution from different meshes are shown in Figure 6-3. It can be seen from the figure that except for the solution from coarse mesh, the difference between the solutions of the other two meshes is small; hence, mesh of 642,587 was used to conduct simulations in this study.

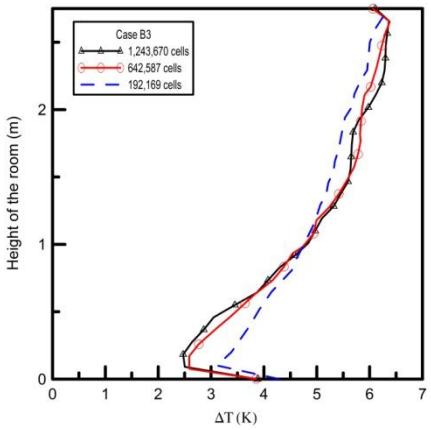

Figure 6-3: Mesh sensitivity test using meshes of 192,169, 642,587 and 1,243,670 cells in B3 case.

6.3.2 Boundary conditions

The boundary conditions of exterior surfaces of sidewalls: wall 2, wall 3, and wall 4 were set as constant temperature and the values were specified according to experimental condition provided in Li et al. (1993) as listed in Table 6-1. Since the exterior surfaces of the ceiling and front wall were not controlled and were affected by the thermal condition of the laboratory, the heat transfer model at those two surfaces account for both heat convection and radiation. The openings at the floor level and ceiling level are defined as inlet and outlet openings respectively. The inlet

opening is given a constant inlet volume flow rate and temperature for each case as shown in Table 6-1. The turbulent kinetic energy and dissipation rate at inlet boundary was determined by following equations:

$$k = \frac{3}{2}(\mathrm{I}v)^2\,, \tag{6-1}$$

$$\varepsilon = \frac{\rho C_\mu k^2}{\frac{\mu_t}{\mu}\mu}, \tag{6-2}$$

where I is turbulence intensity, v is mean velocity. The turbulence intensity is set as 0.01 and eddy viscosity ratio is 10 for determining k and ε values for inlet boundary. The C_μ=0.09 is specified in the turbulence model, the rest of the coefficients are: $C_{1\epsilon}$ =1.44, $C_{2\epsilon}$=1.9, σ_k=1.0, σ_ϵ=1.2, σ_T=1.0. The boundary condition of outlet opening is specified as flow outlet which is given a mass flow rate same as the value given at the inlet opening.

The effect of the radiative emissivity of the surfaces on thermal distribution inside the test room was also taken into account. The emissivities of the surfaces were set as 0.95 for surfaces painted black and 0.1 for surfaces covered with aluminium sheets in the simulation. The surfaces of cases B2, B3, B4 were painted black; the surfaces of case A2 were covered with aluminium sheet. The boundary conditions of each case are shown in Table 6-1.

Table 6-1: Temperatures maintained at exterior wall surfaces of the testroom (Li et al., 1993b)

Cases	volume flow rate (m^3/s)	Heat Load (W)	Supply Temp (^0C)	T_1 (^0C)	T_2 (^0C)	T_3 (^0C)	T_4 (^0C)	T_5 (^0C)
B2	0.023	300	19.2	20.3	23.1	23.3	23	21
B3	0.035	300	18	19.8	22.5	22.8	22.6	20
B4	0.035	450	18	19.8	23	22.4	22.5	19.8
A2	0.035	300	18	20.1	22.7	22.9	22.8	20.3

6.4 Results

This section presents the simulation results calculated by the modelling method set out in Chapter 4. The results are shown to have satisfactory agreement with the measurements taken by Li et al. (1993a). In addition, the effect of radiative absorptivity of the air on the thermal distribution in the enclosure was also investigated. The radiative absorptivity of the air was estimated based on the weather data of city Gavle in Sweden where the laboratory is based. Two averaged absorptivity values were obtained from the calculation using the data from winter time (month January, February, March and December) and summer time (month June, July, August and September). The absorptivity is larger in summer time than in winter time. By comparing the results, the extent of the influence of absorptivity on the thermal distribution in the enclosure was studied.

6.4.1 Simulation results without considering radiative absorptivity

Cases A2 and B3 are two experiments conducted under the same initial and boundary conditions with only surface emissivities differ from each other. The emissivity is 0.1 for case A2 and 0.95 for case B3. The turbulence model employed in this study for case A2 and B3 are shown to agree well with both the measurements and the numerical predictions made by Li et al. (1993) as shown in Figure 6-4.

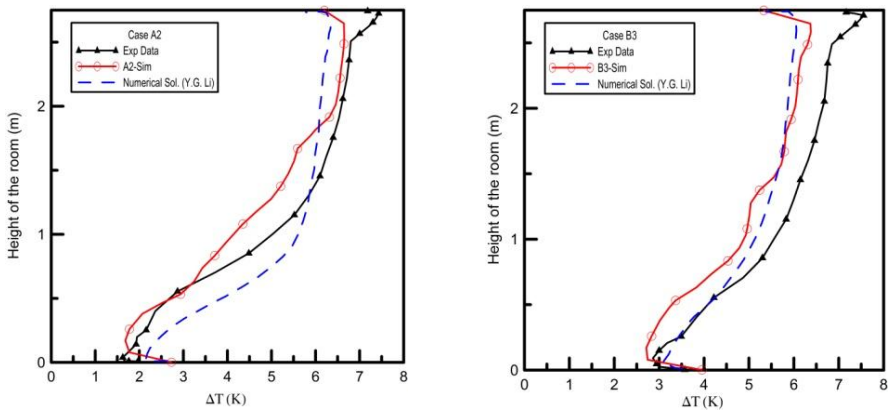

(a) (b)

Figure 6-4: The comparison of the simulation results with numerical solutions and measurements from the literature (Li et al., 1993) in (a) case A2 and (b) case B3.

Case B2 and B4 share most of the conditions of case B3, but case B2 was given a lower volume flow rate at the inlet while case B4 was given a higher heat load. The

simulation results have also shown to agree well with the measurements as can be seen from Figure 6-5.

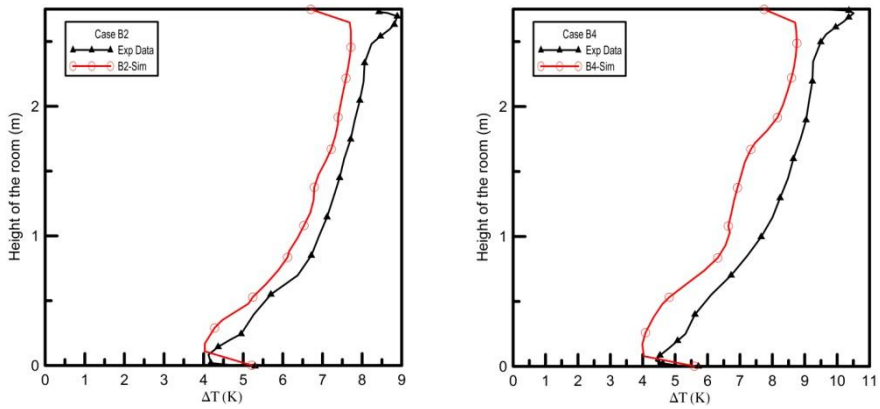

(a) (b)

Figure 6-5: The comparison between the simulation results and the measurements from the literature (Li et al., 1992) in the cases of (a) case B2 and (b) case B4.

The effect of surface emissivity on the thermal distribution can also be seen by comparing the vertical temperature profiles of case A2 and B3 as shown in Figure 6-6. It can be seen from the figures that the black floor surface absorbs the radiative heat from the ceiling heating the air near the floor level. Hence, the case with high surface emissivity (case B3) has higher temperature at the floor level than the case with low surface emissivity (case A2, aluminium surfaces).

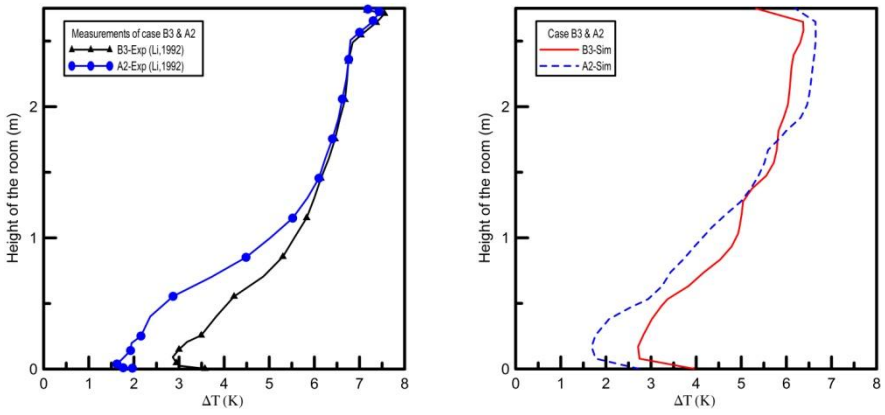

(a) (b)

Figure 6-6: The investigation of the influence of surface emissivity on thermal distribution in the enclosure through (a) experiments and (b) simulations. Both of the results show that less radiative heat was absorbed by the floor surface covered with aluminium sheets (case A2) then the floor painted black (case B3).

6.4.2 The effect of absorptivity of the air on thermal distribution

The absorptivity was estimated based on the weather data obtained from weather monitoring website called Meteoblue. Based on the daily weather data it provides, the averaged relative humidity and temperature of each month were obtained and shown in Figure 6-7. Two averaged absorption coefficients were calculated for summer and winter time respectively: 0.05 and 0.03 m^{-1}. Since the difference of the coefficients at two different weather conditions is not significant, the absorption coefficient of the air was taken as 0.05 m^{-1} for all cases studied.

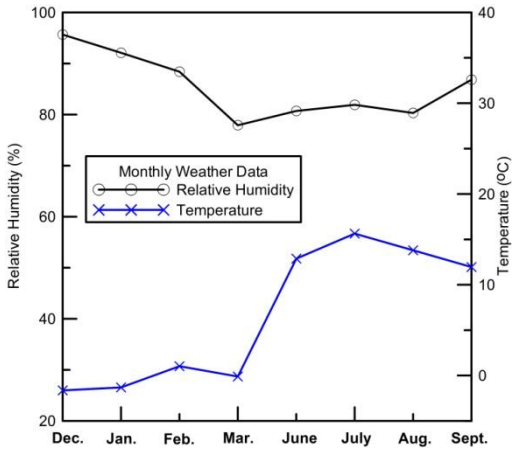

Figure 6-7: Monthly averaged relative humidity and temperatures of city Gavle.

The absorptivity of air is now considered in the simulation for four cases, A2, B2, B3, and B4, studied above. The simulation results were compared with the results obtained earlier. It can be seen that, despite the difference being small, the vertical temperature distribution in the enclosure was increased in general due to the absorptivity of the air as Figure 6-8 and Figure 6-9 (a) shown. However, a relatively significant difference can be found in case B4. As the heat load is higher in case B4, it increases the radiation heat transfer between surfaces; hence the amount of energy absorbed by the air is also increased. Therefore, there is a more discernable influence of absorptivity on the vertical temperature distribution. This can be seen by comparing case B3 and B4 in Figure 6-9.

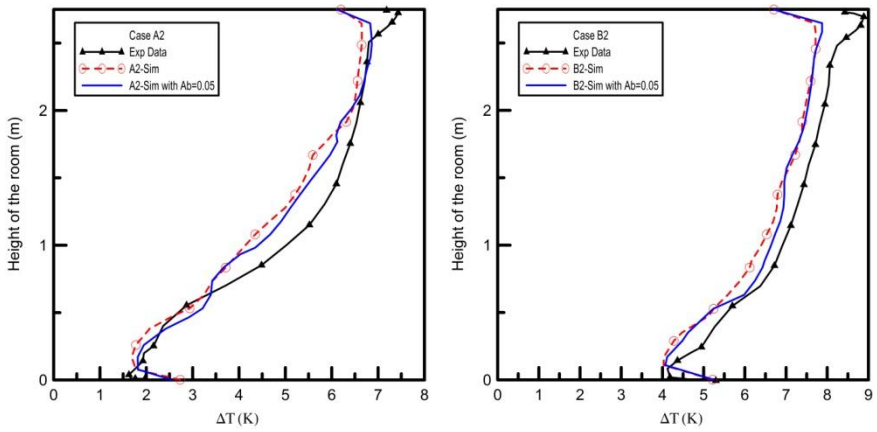

(a) (b)

Figure 6-8: The comparison between the simulation results considering radiative absorptivity of the air and those without in (a) case A2 with surfaces covered with aluminium sheet and (b) case B2 with surfaces painted black.

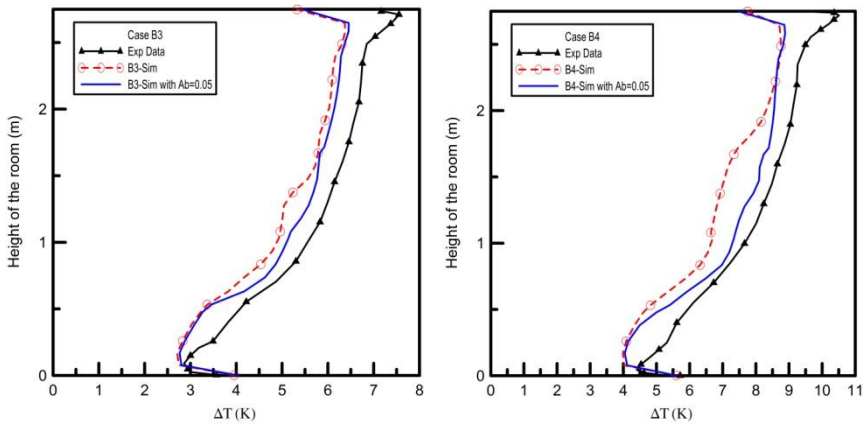

(a) (b)

Figure 6-9: The comparison between the simulation results considering radiative absorptivity of the air and those without in (a) case B3 with heat load at 300W and (b) case B4 with higher heat load at 450W.

Case B3 was also given different supply air flow temperatures: T_s= 14.5 ^oC, 18.9^oC, and 23.2 ^oC respectively to study the effect of supply air flow temperature on heat energy flow through sidewalls. The results show that the higher the inlet flow temperature, the greater the heat energy loss through the boundaries. The magnitude of inlet air temperature also has an effect on how significant the influence of radiative absorptivity is on thermal distribution.

In general, the differences between the results that considered absorptivity and those without are not significant in those cases with low supply air temperature (as can be seen from Figure 6-10). This is because the heat energy was mostly transfer to the incoming strong gravity current at the floor level. For the case with high supply air flow temperature, as shown in Figure 6-11 (T_s=23.2 ^oC), the radiation heat transfer from ceiling to floor surface is increased and hence a greater radiative energy absorbed by air. This phenomena was also found earlier in case B4.

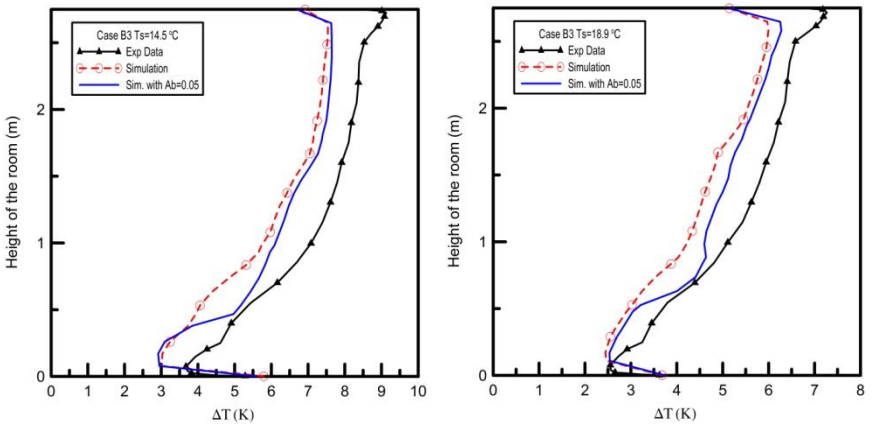

(a) (b)

Figure 6-10: The comparison between the simulation results considering radiative absorptivity of the air and those without in case B3 with supply air temperature at (a) T_s=14.5 ^oC and (b) T_s=18.9 ^oC

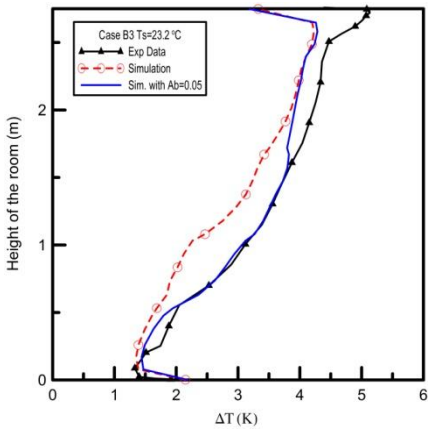

Figure 6-11: The comparison between the simulation results considering radiative absorptivity of the air and those without in case B3 with supply air temperature at T_s=23.2 ^oC.

6.4.3 Conclusions

This chapter models the buoyancy-driven ventilation flow with different radiative properties at boundaries. From the simulation results shown, the realisable two-layer k-ε turbulence model was shown to perform well on modelling thermal distribution in the enclosure both for the case with black surface and aluminium surface. The modelling method set out in Chapter 4 was also employed to take the radiative absorptivity of the air into account. The absorptivity of the air was estimated based on the weather condition obtained from the weather monitoring website. Although the difference was not significant in most cases, the influence of absorptivity to the thermal distribution can be discernible with high air flow temperature.

CHAPTER SEVEN

7 Conclusions and Future Work

7.1 Conclusions

This study simulates the buoyancy-driven flows both in the unventilated filling box model and in the displacement ventilation flow model by using commercial programme StarCCM. The simulation results were validated by the data from the early research works conducted by Worster and Huppert (1983), Sandbach and Lane-Serff (2011b) and Li et al. (1993b) respectively.

The study of the unventilated filling box model was first conducted to simulate the plume flow in the space without heat transfer at boundaries and radiation heat transfer from surface to surface. The conditions are given the same as the conditions of salt-bath experiment (Baines and Turner, 1969). For displacement ventilation flow model, the model considers the heat transfer at the boundary, the surface to surface radiation heat transfer, and the radiative absorptivity of the participating medium in between the surfaces. It is shown to have influence on the thermal distribution in the buoyancy-driven displacement ventilated space. In addition, this study also investigates the performance of the turbulence models in predicting the airflows in the displacement ventilated space in order to obtain accurate predictive results.

The simulation results are shown to have matched reasonably well with the mathematical solutions and experimental measurements obtained from the early studies. Based on these simulation results and the findings throughout the study, a number of conclusions can be drawn as follow:

a. The modelling approach established in this study was shown to perform well on modelling thermal distribution in buoyancy-driven displacement ventilation flow space. The model was first used to simulate the effects of radiative absorptivity of the air on thermal distribution in the space; then the modelling approach was used to simulate another set of experiments considering surface emissivity. The results were shown to have match well with the measurements from different experiments.

b. The air in the ventilated space was often regarded as a transparent medium to thermal radiation. However, the results of this study show that ignoring the absorptivity of the air can result in less accurate predictive results. It is in fact that the radiative absorptivity of the air has influence on the thermal distribution in the buoyancy-driven ventilated spaces.

c. It can be seen from Figure 5-16, by taking the radiative absorptivity of the air into account, the predictive accuracy of the thermal distribution in the space was improved especially at the lower half of the test room. By comparison to the results from mathematical model (Sandbach and Lane-Serff, 2011b) and the surface to surface radiation model, the participating radiation model provides accurate predictive results. In most cases, the averaged error can be less than 10% .

d. The modelling results using three absorption coefficients cited from early studies were compared in this study. The results show that the temperature profiles were either under or over predicted by those three coefficients. It is therefore clear to see that the absorption coefficient should be determined according to the conditions of each case, rather than be given the same value to all cases.

e. From the simulation results shown, it was found that the influence of the radiative absorptivity not only affected by the magnitude of absorption coefficient, but also affected by the size of the openings of the ventilated room. It can be seen that the discrepancy between the results are larger in Model Hf19 than the other two.

f. The mass flow rate in the ventilated test room is found to vary with two factors: the absorption coefficient and the size of the openings. It can be seen from Figure 5-23 that not only the mass flow rate increases with larger openings but also with large absorption coefficients.

g. The magnitude of the mass flow rate is influenced by the strength of the stratification layer. It can be seen from Figure 5-19 (b) and Table 5-1 that the strength of the stratification is weakened by large absorption coefficient (large mass flow rate); the stratification of Model Hf30 and Hf19, on the other hand, were less affected by the absorption coefficient due to relatively small mass flow rate as shown in Table 5-2 and Table 5-3.

h. In most early studies which considered the absorptivity of the air, the method used to determine the absorption coefficient of the air was not elucidated. This study details the process of the determination of absorption coefficient of the air. The two main participants, CO_2 and H_2O, were taken into account. The coefficient was found to vary with humidity and temperature which agrees with the findings from early experimental data (Rothman et al., 1998).

i. The magnitude of the absorption coefficient is generally varied with two variables: humidity and pathlength. From all the absorption coefficients calculated in this study, it can be seen that when the coefficient under a fixed temperature condition, the higher the humidity the larger the coefficient (Figure 4-23).

j. The airflows in the buoyancy-driven displacement ventilation flow region often consist of airflows at different turbulence level. Hence, a standard k-ε turbulence model may not provide satisfactory solutions. The selection of turbulence model should be made based on the nature of the airflows in the enclosure. In this study, the realisable two-layer k-ε turbulence model which takes the damping effects into account was shown to perform well among all other turbulence models.

k. Two types of turbulence length scale models, Wolfshtein shear-driven and Xu buoyancy-driven model, were implemented in the realisable two-layer k-ε turbulence model for modelling the temperature profiles of all cases listed in Table 4-2 and Table 4-3. The results show that the Wolfshtein shear-driven model performs well in the cases with low volume flow rate; Xu buoyancy-driven model performs better in the cases with higher volume flow rate.

l. The two-layer k-ε turbulence model together with the participating media radiation model also showed to perform well in modelling the experiment presented in Chapter 6. The results also suggest that the effect of absorptivity of the air becomes large with higher inlet airflow temperature.

In summary, buoyancy-driven two-layer turbulence model (Xu and Chen, 2001) is recommended for modelling buoyancy-driven displacement ventilation flows. It is also shown in this study that polyhedral mesh provides accurate solutions with less mesh cells required. A refined mesh is advised to generate around near-wall region for capturing the damping effects and high temperature gradients near heat source. The mathematical model for determining absorption coefficients provides the values according to the conditions of the air, and is shown to help improve the predicted results in the cases of high mass flow rate and high heat flow.

7.2 Future work

The modelling results presented in this study were shown to have a satisfactory agreement with the experimental results. However, by using the commercial CFD programme StarCCM, the modelling takes longer computational time than using approximate numerical model. In addition, the ventilation type studied in this work is only one kind of many other ventilation types; it would therefore be beneficial to have a look at other models with different conditions to have a complete view on ventilation systems. Hence, here in this section, some future works are proposed and outlined below:

a. In this study, the simulations considered the absorptivity of the air and its effects on thermal distribution. Since thermal comfort for human in the living space depends on how thermal is distributed, it would be helpful to investigate further on the issue of designing thermal comfort environment.

b. The CFD modelling can provide sufficient accurate predictive results; however, it requires large computational resource to complete a simulation work. Therefore, it would be worth developing an approximate mathematical model which also considers radiative absorptivity of the air for modelling buoyancy-driven displacement ventilation flows.

c. This study focus on modelling single buoyancy source displacement ventilation flow with ambient air temperature lower than in the enclosure. However, there can be other scenarios where the enclosure contains multiple heat sources and the ambient air temperature is relatively high. Since these conditions may have effects on buoyancy flows and hence thermal distribution, it may worth considering these conditions in further study.

d. Depending on the location of the openings, the ventilation flow models includes: doorway ventilation, opposing wind ventilation, mixing ventilation and etc,. The airflows in these models can be different, and therefore they would require different types of turbulence model for accurate simulation results. Hence, it is worth investigating different types of ventilation flows base on the knowledge of this study in order to have a complete view on modelling ventilation flows.

REFERENCES

Abdalla, I. E., Cook, M. J., Rees, S. J. & Yang, Z. Y. 2007. Large-Eddy Simulation of Buoyancy-Driven Natural Ventilation in an Enclosure with a Point Heat Source. *International Journal of Computational Fluid Dynamics,* 21**,** 231-245.

Alberti, M., Weber, R. & Mancini, M. 2015. Re-creating Hottel's emissivity charts for carbon dioxide and extending them to pressure using HITEMP-2010 data base. *Combustion and Flame,* 162**,** 597-612.

Alberti, M., Weber, R. & Mancini, M. 2016. Re-creating Hottel's emissivity charts for water vapor and extending them to 40 bar pressure using HITEMP-2010 data base. *Combustion and Flame,* 169**,** 141-153.

Angell, J. K. 1964. Measurements of Lagrangian and Eulerian Properties of Turbulence at a Height of 2,500 ft. *Quarterly Journal of the Royal Meteorological Society,* 90**,** 57-71.

Angell, J. K., Pack, D. H., Hoecker, W. H. & Delver, N. 1971. Lagrangian-Eulerian Time-Scale Ratios Estimated from Constant Volume Balloon Flights Past a Tall Tower. *Quarterly Journal of the Royal Meteorological Society,* 97**,** 87-92.

Baines, W. D. & Turner, J. S. 1969. Turbulent Buoyant Convection from a Source in a Confined Region. *Journal of Fluid Mechanics,* 37**,** 51-80.

Batchelor, G. K. 1954. Heat Convection and Buoyancy Effects in Fluids. *Quarterly Journal of the Royal Meteorological Society,* 80**,** 339-358.

Berour, N., Lacroix, D., Boulet, P. & Jeandel, G. 2004. Radiative and Conductive Heat Transfer in a Nongrey Semitransparent Medium. Application to Fire Protection Curtains. *Journal of Quantitative Spectroscopy & Radiative Transfer,* 86**,** 9-30.

Bjorn, E. & Nielsen, P. V. 2002. Dispersal of Exhaled Air and Personal Exposure in Displacement Ventilated Rooms. *Indoor Air,* 12**,** 147-164.

Blazek, J. 2005. *Computational fluid dynamics principles and applications / J. Blazek,* Amsterdam, San Diego, Elsevier.

Brewster, M. Q. 1992. *Thermal radiative transfer and properties / M. Quinn Brewster,* New York - Chichester : J. Wiley & Sons.

Brown, W., Wilson, A. & Solvason, K. 1963. Heat and Moisture Flow through Openings. *American Society of Heating, Refrigerating and Air-Conditioning Engineers,* 5**,** 49-54.

Burch, D. E., Gryvnak, D. A. & Williams, D. 1962. Total Absorptance of Carbon Dioxide in the Infrared. *Applied Optics,* 1**,** 759-765.

CD-adapco 2012. User Guide Star CCM+ Version 7.06.012. *In:* CD-ADAPCO (ed.). CD-adapco.

CD-adapco. 2013. STARCCM FoundationTrainingV2.0. Available: http://www.scribd.com/doc/148337137/Lec-STARCCM-FoundationTrainingV2-0.

Çengel, Y. A. 2011. *Thermodynamics : an engineering approach,* London, Singapore : McGraw-Hill.

Chen, G. Y. & Xu, W. R. 1998. A Zero-Equation Turbulence Model for Indoor Airflow Simulation. *Energy and Buildings,* 28**,** 137-144.

Chen, Q. 1995. Comparison of Different K-Epsilon Models for Indoor Air-Flow Computations. *Numerical Heat Transfer Part B-Fundamentals,* 28**,** 353-369.

Chien, K. Y. 1982. Predictions of Channel and Boundary-Layer Flows with a Low-Reynolds-Number Turbulence Model. *Aiaa Journal,* 20**,** 33-38.

Chow, K. & Holdo, A. E. 2010. On the Influence of Boundary Conditions and Thermal Radiation on Predictive Accuracy in Numerical Simulations of Indoor Ventilation. *Building and Environment,* 45**,** 437-444.

Crawford, T. M. & Duchon, C. E. 1999. An Improved Parameterization for Estimating Effective Atmospheric Emissivity for Use in Calculating Daytime Downwelling Longwave Radiation. *Journal of Applied Meteorology,* 38**,** 474-480.

Dalziel, S. B. & Laneserff, G. F. 1991. The Hydraulics of Doorway Exchange Flows. *Building and Environment,* 26**,** 121-135.

Davidson, L. 1989. Ventilation by Displacement in a 3-Dimensional Room - a Numerical Study. *Building and Environment,* 24**,** 363-372.

Davidson, L. & Nielsen, P. V. 2003 Comparing a K-E Model and the V2-F Model in a 3D Isothermal Wall Jet. Report R0301. Building Technology and Structural Engineering. Aalborg, Denmark

Davidson, L., Nielsen, P. V. & Sveningsson, A. 2003. Modifications of the V2-F Model for Computing the Flow in a 3D Wall Jet. International Symposium on Turbulence, Heat and Mass Transfer, 12-17, October 2003 Antalya, Turkey. International Symposium on Turbulence, Heat and Mass Transfer, pp. 577-584.

Dean, J. A. 2005. *Lange's handbook of chemistry*, Maidenhead : McGraw-Hill.

Deevy, M. 2006 CFD Modelling of the Benchmark Displacement Ventilation Test Case. Health & Safety Laboratory. Buxton

Deevy, M. & Gobeau, N. 2006 CFD Modelling of Benchmark Test Cases for Flow Around a Computer Simulated Person. Health & Safety Laboratory. Buxton

Etheridge, D. & Sandberg, M. 1996. *Building Ventilation: Theory and Measurement*, Wiley.

Feichter, J., Schultz, M. & Diehl, T. 2002. Modelling Chemical Constituents of the Atmosphere. *Computing in Science & Engineering,* 4**,** 56-63.

Fitzgerald, S. D. & Woods, A. W. 2010. Transient Natural Ventilation of a Space with Localised Heating. *Building and Environment,* 45**,** 2778-2789.

Gao, J., Zhao, J. N. & Gao, F. S. 2006. Displacement of Natural Ventilation in an Enclosure with a Convective/Radiative Heat Source and Nonadiabatic Envelopes. *Journal of Solar Energy Engineering-Transactions of the Asme,* 128**,** 83-89.

Germeles, A. E. 1975. Forced Plumes and Mixing of Liquids in Tanks. *Journal of Fluid Mechanics,* 71**,** 601-623.

Hanna, S. R. 1981. Lagrangian and Eulerian Time-Scale Relations in the Daytime Boundary Layer. *Journal of Applied Meteorology,* 20**,** 242-249.

Henkes, R. A. W. M. & Hoogendoorn, C. J. 1989. Comparison of Turbulence Models for the Natural Convection Boundary Layer Along a Heated Vertical Plate. *International Journal of Heat and Mass Transfer,* 32**,** 157-169.

Henkes, R. A. W. M., Van Der Vlugt, F. F. & Hoogendoorn, C. J. 1991. Natural-Convection Flow in a Square Cavity Calculated with Low-Reynolds-Number Turbulence Models. *International Journal of Heat and Mass Transfer,* 34**,** 377-388.

Hottel, H. C. 1967. *Radiative transfer / (by) Hoyt C. Hottel and Adel F. Sarofim,* New York, New York : McGraw-Hill.

Howell, S. A. & Potts, I. 2002. On the Natural Displacement Flow through a Full-Scale Enclosure, and the Importance of the Radiative Participation of the Water Vapour Content of the Ambient Air. *Building and Environment,* 37**,** 817-823.

Iaccarino, G. 2001. Predictions of a Turbulent Separated Flow Using Commercial CFD Codes. *Journal of Fluids Engineering,* 123**,** 819-828.

Jaluria, Y., Lee, S. H. K., Mercier, G. P. & Tan, Q. Visualization of Transport Across a Horizontal Vent Due to Density and Pressure Differences. National Heat Transfer Conference. 1993. pp.1-17

Ji, Y., Cook, M. J. & Hanby, V. 2007. CFD Modelling of Natural Displacement Ventilation in an Enclosure Connected to an Atrium. *Building and Environment,* 42**,** 1158-1172.

Jones, W. P. & Launder, B. E. 1972. The Prediction of Laminarization with a Two-Equation Model of Turbulence. *International Journal of Heat and Mass Transfer,* 15**,** 301-314.

Jongen, T. 1998. *Simulation and Modeling of Turbulent Incompressible Flows.* Ph.D. Thesis, Lausanne EPFL.

Kaye, N. B. & Hunt, G. R. 2007. Smoke Filling Time for a Room Due to a Small Fire: The Effect of Ceiling Height to Floor Width Aspect Ratio. *Fire Safety Journal,* 42**,** 329-339.

Kim, S. W. & Chen, C. P. 1988. A Multiple-Time-Scale Turbulence Model Based on Variable Partitioning of Turbulent Kinetic Energy Spectrum. *26th Aerospace Sciences Meeting.* American Institute of Aeronautics and Astronautics.

Lallemant, N., Sayre, A. & Weber, R. 1996. Evaluation of Emissivity Correlations for H2O-CO2-N-2/Air Mixtures and Coupling with Solution Methods of The Radiative Transfer Equation. *Progress in Energy and Combustion Science,* 22**,** 543-574.

Lam, C. K. G. & Bremhorst, K. 1981. A Modified Form of the K-Epsilon Model for Predicting Wall Turbulence. *Journal of Fluids Engineering-Transactions of the Asme,* 103**,** 456-460.

Leckner, B. 1972. Spectral and Total Emissivity of Water Vapor and Carbon Dioxide. *Combustion and Flame,* 19**,** 33-48.

Li, Y., Fuchs, L. & Sandberg, M. 1993a. Numerical Prediction of Airflow and Heat-Radiation Interaction in a Room with Displacement Ventilation. *Energy and Buildings,* 20**,** 27-43.

Li, Y., Sandberg, M. & Fuchs, L. 1992. Vertical Temperature Profiles in Rooms Ventilated by Displacement: Full-Scale Measurement and Nodal Modelling. *Indoor Air-International Journal of Indoor Air Environment and Health,* 2**,** 225-243.

Li, Y. G., Sandberg, M. & Fuchs, L. 1993b. Effects of Thermal-Radiation on Air-Flow with Displacement Ventilation - an Experimental Investigation. *Energy and Buildings,* 19**,** 263-274.

Linden, P. F. 1999. The Fluid Mechanics of Natural Ventilation. *Annual Review of Fluid Mechanics,* 31**,** 201-238.

Linden, P. F., Laneserff, G. F. & Smeed, D. A. 1990. Emptying Filling Boxes - the Fluid-Mechanics of Natural Ventilation. *Journal of Fluid Mechanics,* 212**,** 309-335.

Linden, P. F. & Simpson, J. E. 1985. Bouyancy Driven Flows through an Open Door. *Air Information Review,* 6**,** 4-5.

McCoy, J. H., Rensch, D. B. & Long, R. K. 1969. Water Vapor Continuum Absorption of Carbon Dioxide Laser Radiation near 10 mu. *Applied Optics,* 8**,** 1471-1478.

Modak, A. T. 1979. Radiation from Products of Combustion. *Fire Safety Journal,* 1**,** 339-361.

Modest, M. 1993. *Radiative heat transfer,* New York, McGraw-Hill.

Modest, M. F. 2003. *Radiative heat transfer*, New York ; London : McGraw-Hill.

Mohammadi, B. & Puigt, G. 2001. Mathematical and Numerical Analysis of an Alternative Well-Posed Two-Layer Turbulence Model. *Esaim-Mathematical Modelling and Numerical Analysis-Modelisation Mathematique Et Analyse Numerique,* 35**,** 1111-1136.

Morton, B. R., Taylor, G. & Turner, J. S. 1956. Turbulent Gravitational Convection from Maintained and Instantaneous Sources. *Proceedings of the Royal Society of London Series a-Mathematical and Physical Sciences,* 234**,** 1-23.

Mossi, A., Galarça, M. M., Brittes, R., Vielmo, H. A. & França, F. H. R. 2012. Comparison of Spectral Models in the Computation of Radiative Heat Transfer in Participating Media Composed of Gases And Soot. *Journal of the Brazilian Society of Mechanical Sciences and Engineering,* 34**,** 112-119.

Murakami, S., Ohira, N. & Kato, S. 2000. CFD Analysis of a Thermal Plume and the Indoor Air Flow Using K-Epsilon Models with Buoyancy Effects. *Flow Turbulence and Combustion,* 63**,** 113-134.

Narasimha, R. & Sreenivasan, K. R. 1979. Relaminarization of Fluid Flows. *Advances in applied mechanics,* 19**,** pp. 221-309.

Nielsen, P. V. 1998. The Selection of Turbulence Models for Prediction of Room Airflow. *ASHRAE Transactions,* Vol. 104**,** pp. 1119-1127.

Nielsen, P. V. 2004. Computational Fluid Dynamics and Room Air Movement. *Indoor Air,* 14**,** 134-143.

Norris, H. L. 1975. *Turbulent channel flow with a moving wavy boundary.* PhD Thesis, Stanford University.

Noto, K. & Nakai, K. 2008. Direct Numerical Simulation of Turbulent Thermal Plume in Stably Stratified Ambient: Formulation, Numerical Methodology, Reverse Transition, Relaminarization, and Turbulent Enhancement. *Numerical Heat Transfer Part B-Fundamentals,* 53**,** 313-357.

Novoselac, A., Burley, B. J. & Srebric, J. 2006. Development of New and Validation of Existing Convection Correlations for Rooms with Displacement Ventilation Systems. *Energy and Buildings,* 38**,** 163-173.

Orloff, L., Modak, A. T. & Markstein, G. H. Radiation from Smoke Layers. 17th Int. Symp. Combustion. 1979.

Patel, V. C., Rodi, W. & Scheuerer, G. 1985. Turbulence Models for Near-Wall and Low Reynolds-Number Flows - A Review. *Aiaa Journal,* 23**,** 1308-1319.

Peric, M. & Ferguson, S. 2004. The Advantage of Polyhedral Meshes. www.cd-adapco.com

Poling, B. E. 2001. *The properties of gases and liquids,* New York & London, London : McGraw-Hill.

Prandtl, L. 1952. *Essentials of fluid dynamics,* London & Glasgow, Blackie & son Limited.

Reynolds, O. 1895. On the Dynamical Theory of Incompressible Viscous Fluids and the Determination of the Criterion. *Philosophical Transactions of the Royal Society of London. A,* 186**,** 123-164.

Rodi, W. 1993. *Turbulence models and their application in hydraulics : a state-of-the-art review / Wolfgang Rodi,* Rotterdam, Rotterdam : A.A.Balkema.

Rooney, G. G. 2005. Modelling of Downwelling Long-Wave Radiation Using Cloud Fraction Obtained from Laser Cloud-Base Measurements. *Atmospheric Science Letters,* 6**,** 160-163.

Rooney, G. G. & Linden, P. F. 1996. Similarity Considerations for Non-Boussinesq Plumes in an Unstratified Environment. *Journal of Fluid Mechanics,* 318**,** 237-250.

Rooney, G. G. & Linden, P. F. 1997. Strongly Buoyant Plume Similarity and 'Small-Fire' Ventilation. *Fire Safety Journal,* 29**,** 235-258.

Rothman, L. S., Rinsland, C. P., Goldman, A., Massie, S. T., Edwards, D. P., Flaud, J. M., Perrin, A., Camy-Peyret, C., Dana, V., Mandin, J. Y., Schroeder, J., McCann, A., Gamache, R. R., Wattson, R. B., Yoshino, K., Chance, K. V., Jucks, K. W., Brown, L. R., Nemtchinov, V. & Varanasi, P. 1998. The hitran molecular spectroscopic database and hawks (hitran atmospheric workstation): 1996 edition. *Journal of Quantitative Spectroscopy and Radiative Transfer,* 60**,** 665-710.

Rouse, H., Yih, C. S. & Humphreys, H. W. 1952. Gravitational Convection from a Boundary Source. *Tellus,* 4**,** 201-210.

Sandbach, S. 2009. *Mathematical and laboratory modelling of ventilation.* PhD Thesis, University of Manchester.

Sandbach, S. D. & Lane-Serff, G. F. 2011a. Transient Buoyancy-Driven Ventilation: Part 1. Modelling Advection. *Building and Environment,* 46**,** 1578-1588.

Sandbach, S. D. & Lane-Serff, G. F. 2011b. Transient Buoyancy-Driven Ventilation: Part 2. Modelling Heat Transfer. *Building and Environment,* 46**,** 1589-1599.

Schlichting, H. 1962. *Boundary layer theory / by Hermann Schlichting-translated by J. Kestin,* New York, London, New York, London : McGraw-Hill.

Scrase, I. 2000 White Collar Co2 : Energy Consumption in the Service Sector. London

Shih, T.-H., Liou, W. W., Shabbir, A., Yang, Z. & Zhu, J. 1995a. A New K-E Eddy Viscosity Model for High Reynolds Number Turbulent Flows. *Computers & Fluids,* 24**,** 227-238.

Shih, T.-H., Zhu, J. & Lumley, J. L. 1995b. A New Reynolds Stress Algebraic Equation Model. *Computer Methods in Applied Mechanics and Engineering,* 125**,** 287-302.

Siegel, R. 1992. *Thermal radiation heat transfer / Robert Siegel and John R. Howell,* Washington, Washington : Hemisphere Publishing Corporation.

Snegirev, A. Y. & Frolov, A. S. 2011. The Large Eddy Simulation of a Turbulent Diffusion Flame. *High Temperature,* 49**,** 690-703.

Sørensen, D. N. & Nielsen, P. V. 2003. Quality Control of Computational Fluid Dynamics in Indoor Environments. *Indoor Air-International Journal of Indoor Air Quality and Climate,* 13**,** 2-17.

Steiner, A. 1971. On the Reverse Transition of a Turbulent Flow Under Action of Buoyancy Forces. *Journal of Fluid Mechanics,* 47**,** 503-512.

Taub, G. N., Lee, H., Balachandar, S. & Sherif, S. A. 2015. An Examination of the High-Order Statistics of Developing Jets, Lazy and Forced Plumes at Various Axial Distances from Their Source. *Journal of Turbulence,* 16**,** 950-978.

Taylor, G. I. & U.S. Atomic Energy Commission 1946. *Dynamics of a mass of hot gas rising in air,* Oak Ridge, Tenn., Technical Information Division, Oak Ridge Operations.

Teodosiu, C., Kuznik, F. & Teodosiu, R. 2014. CFD Modeling of Buoyancy Driven Cavities with Internal Heat Source—Application to Heated Rooms. *Energy and Buildings,* 68, Part A**,** 403-411.

The British Standards Institution 1999. Ventilation for Buildings. Design Criteria for The Indoor Environment. British Standards Institution

Tien, C. L. 1968. Thermal Radiation Properties of Gases. *Advances in Heat Transfer,* Vol. 5**,** pp. 253-324.

Tien, C. L. & Lee, S. C. 1982. Flame Radiation. *Progress in Energy and Combustion Science,* 8**,** 41-59.

Townsend, A. A. 1970. Entrainment and the Structure of Turbulent Flow. *Journal of Fluid Mechanics,* 41**,** 13-46.

Turner, J. S. 1969. Buoyant Plumes and Thermals. *Annual Review of Fluid Mechanics,* 1**,** 29-44.

Van Driest, E. R. 1956. On Turbulent Flow near a Wall. *Journal of the Aeronautical Sciences,* 23**,** 1007-1011.

Versteegh, T. & Nieuwstadt, F. 1996. Scaling of Free Convection Between Two Differentially Heated Infinite Vertical Plates.

White, F. M. 2006. *Viscous fluid flow / Frank M. White,* Boston, London, Boston, Mass. London : McGraw-Hill.

Wolfshtein, M. 1969. The Velocity and Temperature Distribution in One-Dimensional Flow with Turbulence Augmentation and Pressure Gradient. *International Journal of Heat and Mass Transfer,* 12**,** 301-318.

Worster, M. G. & Huppert, H. E. 1983. Time-Dependent Density Profiles in a Filling Box. *Journal of Fluid Mechanics,* 132**,** 457-466.

Xu, M., Yamanaka, T. & Kotani, H. 2001. Vertical Profiles of Temperature and Contaminant Concentration in Rooms Ventilated by Displacement with Heat Loss through Room Envelopes. *Indoor Air-International Journal of Indoor Air Quality and Climate,* 11**,** 111-119.

Xu, W., Chen, Q. & Nieuwstadt, F. T. M. 1998. A New Turbulence Model for Near-Wall Natural Convection. *International Journal of Heat and Mass Transfer,* 41**,** 3161-3176.

Xu, W. R. & Chen, Q. Y. 2000. Simulation of Mixed Convection Flow in a Room with a Two-Layer Turbulence Model. *Indoor Air-International Journal of Indoor Air Quality and Climate,* 10**,** 306-314.

Xu, W. R. & Chen, Q. Y. 2001. A Two-Layer Turbulence Model for Simulating Indoor Airflow Part II. Applications. *Energy and Buildings,* 33**,** 627-639.

Yakhot, V. & Orszag, S. A. 1986. Renormalization-Group Analysis of Turbulence. *Physical Review Letters,* 57**,** 1722-1724.

Yamanouchi, T. & Tanaka, M. 1985. Absorption Properties of the Near-Infrared Water Vapor Bands. *Journal of Quantitative Spectroscopy and Radiative Transfer,* 34**,** 463-472.

Yih, C. S. 1951. Free Convection due to a Point Source of Heat. *Journal of Applied Mechanics-Transactions of the Asme,* 18**,** 323-323.

Zhang, H. & Modest, M. F. 2002. Evaluation of the Planck-Mean Absorption Coefficients from HITRAN and HITEMP Databases. *Journal of Quantitative Spectroscopy and Radiative Transfer,* 73**,** 649-653.

Zhang, Z., Zhai, Z. Q., Zhang, W. & Chen, Q. Y. 2007. Evaluation of Various Turbulence Models in Predicting Airflow and Turbulence in Enclosed Environments by CFD: Part 2-Comparison with Experimental Data from Literature. *Hvac&R Research,* 13**,** 871-886.

Zukowska, D., Melikov, A. & Popiolek, Z. 2012. Impact of Personal Factors and Furniture Arrangement on the Thermal Plume above a Sitting Occupant. *Building and Environment,* 49**,** 104-116.